Development and Characterization of High Curie-Temperature (T_C) and High-Performance Piezo-/ferroelectric Materials of Complex Perovskite Structure

by

Neda Afzali

M.Sc., Sharif University of Technology, 2015
B.Sc., Sharif University of Technology, 2013

Thesis Submitted in Partial Fulfillment of the
Requirements for the Degree of
Master of Science

in the
Department of Chemistry
Faculty of Science

SIMON FRASER UNIVERSITY
Fall 2023

Declaration of Committee

Name: **Neda Afzali**

Degree: **Master of Science (Chemistry)**

Title: **Development and Characterization of High Curie-Temperature (T_C) and High-Performance Piezo-/ferroelectric Materials of Complex Perovskite Structure**

Committee: **Chair:** **Paul Li**
Professor, Chemistry

Zuo-Guang Ye
Supervisor
Professor, Chemistry

Hua-Zhong Yu
Committee Member
Professor, Chemistry

Steven Holdcroft
Committee Member
Professor, Chemistry

Gary Leach
Examiner
Associate Professor, Chemistry

Abstract

Novel piezo-/ferroelectric materials are being developed to use in a variety of applications including energy harvesting devices, electromechanical sensors and actuators, ultra-sound detectors, etc. One of the main challenges in this area is developing piezo-/ferroelectric materials with high Curie temperatures (T_C) enabling them to maintain their performance in elevated temperatures. Bismuth-containing systems, particularly $BiScO_3$-$PbTiO_3$ (BS-PT), show promise but face limitations like high conductivity at elevated temperatures and narrow morphotropic phase boundary (MPB) region. Also, it is difficult to grow Bi-based complex perovskite single crystals. This study focuses on developing high-temperature and high-performance piezo- /ferroelectric perovskite materials and establishing structure-property relationships in the developed perovskite material systems for potential energy storage and transduction applications. Under this objective, a new bismuth-based $(1-x)Pb(Sc_{1/2}Nb_{1/2})O_3$-$xBiScO_3$ solid solution is developed with moderate piezoelectric performance suitable for energy storage applications. Also, a novel ternary solid solution combining $Pb(Sc_{1/2}Nb_{1/2})O_3$ and $BiScO_3$-$PbTiO_3$ has been successfully synthesized which exhibits extended morphotropic phase boundary (MPB) region and higher T_C comparing to well-known $Pb(Zr,Ti)O_3$. Finally, single crystals of the 0.1PSN-0.315BS-0.585PT were successfully grown with a high T_C of 410 °C and a promising piezo-/ferroelectric performance (E_C = 67 kV/cm and d_{33} = 478 pC/N). This work demonstrates the feasibility of developing high-temperature piezo-/ferroelectric materials, with improved performance and enhanced relaxor behavior, making them ideal for a range of applications, in particular at high temperatures.

Keywords: Piezo-/ferroelectric; High Curie temperature; Bismuth-based solid solutions; Ceramic; Single crystal

Acknowledgements

I would like to thank my senior supervisor, Dr. Zuo-Guang Ye, for the invaluable research opportunity he provided and for his support and guidance during my graduate studies.

I would also like to thank my supervisory committee members, Dr. Hua-Zhong Yu, and Dr. Steven Holdcroft, for their valuable feedback and guidance on my research. Additionally, I express my gratitude to Dr. Gary Leach for his role as my internal examiner of this thesis.

I would like to express my appreciation towards the past and present members of Dr. Ye's research group. I am grateful to Dr. Alexei Bokov for his valuable research advice and thoughtful questions on my research. Also, I would like to thank Dr. Yi Yuan for imparting invaluable knowledge about experimental procedures and structural refinements. Also, I would like to thank Dr. Bixia wang and Dr. Zenghui Liu for their assistance with structural refinements.

I would like to thank my friends in 4dlabs, Dr. Neha Clair, Dr. Vidhi Chauhan, Sveta Chen, Amber Lin, Qi Deng and Nastaran Taghvaei for their support in the laboratory and friendship. I would like to specially thank Tara Nazari for introducing me to the single crystal growth technique and Polarized Light Microscopy as well as her friendship.

I would like to thank Brendan VanSpall, an undergraduate student who contributed to the synthesis and characterizations in the $Pb(Sc_{1/2}Nb_{1/2})O_3$-$BiScO_3$-$PbTiO_3$ project during his CHEM 481 course. Additionally, my gratitude extends to Michael Wong for his assistance with characterizations at 4D Labs.

I appreciate the financial and facility support from the 4D LABS, Department of Chemistry, Simon Fraser University, the Natural Sciences and Engineering Research Council of Canada, and the United States of Office of Naval Research.

A special mention of heartfelt thanks goes to my beloved husband, Ehsan Taghvaie, for his unwavering support, unconditional love, and encouragement during my graduate studies at Simon Fraser University. It was impossible without you “my love”.

Lastly, I would like to thank my parents for their love and support on my journey of life.

Table of Contents

Declaration of Committee ii
Abstract iii
Acknowledgements iv
Table of Contents vi
List of Tables viii
List of Figures x
List of Acronyms xv

Chapter 1. Introduction 1
1.1. Piezoelectric Properties 1
1.2. Ferroelectric Properties 2
1.3. Applications of Piezo-/ferroelectric Materials 4
1.4. Perovskite Structure 5
1.5. PZT Solid Solution and Morphotropic Phase Boundary (MPB) 7
1.6. Relaxor Ferroelectrics 9
1.7. Development of Piezo-/ferroelectric Materials 11
1.8. Limitations of Leading Piezo/ferroelectric Materials and Challenges 13
1.9. Objectives and Organization of the Thesis 17

Chapter 2. Materials Characterizations: Principles and Techniques 19
2.1. Introduction 19
2.2. Powder X-ray Diffraction (XRD) 19
  2.2.1. Principles Employed in Crystal Symmetry Determination 20
  2.2.2. Rietveld Refinement 22
2.3. Dielectric Spectroscopy 23
2.4. Ferroelectric Hysteresis Measurements 26
2.5. Piezoelectric Measurements 27
2.6. Helium Ion Microscopy (HIM) 28
2.7. Polarized Light Microscopy (PLM) 30

Chapter 3. Synthesis, Structure and Characterization of a New Bismuth-based Relaxor Ferroelectric Perovskite Solid Solution System of (1-x)Pb($Sc_{1/2}Nb_{1/2}$)O_3-xBiScO_3 33
3.1. Abstract 33
3.2. Introduction 34
3.3. Solid State Synthesis and Ceramics Sintering 35
3.4. Formation of Solid Solution and Determination of its Solubility Limit 36
3.5. Crystal Structure Analysis 37
3.6. Ceramic Microstructure Analysis 40
3.7. Dielectric Properties and Relaxation 43
3.8. Relaxor Ferroelectric Properties 47
3.9. Ferroelectric and Piezoelectric Properties 50
3.10. Conclusions 52

Chapter 4. Synthesis, Structure and Properties of a Novel Ternary Solid Solution with High T_C and High Piezo-/Ferroelectric Performances 54
4.1. Abstract 54
4.2. Introduction...55
4.3. Solid State Synthesis and Ceramics Sintering 57
4.4. Crystal Structure Analysis...58
4.5. Ceramic Microstructure Analysis 65
4.6. Dielectric Properties and Phase Transition 68
4.7. Dielectric Relaxation 76
4.8. Poling Effect on Piezoelectric Performance 77
4.9. Ferroelectric and Piezoelectric Properties.....................................79
4.10. Conclusions 85

Chapter 5. Growth and Characterization of Relaxor Ferroelectric (1-x)($0.35BiScO_3$-$0.65PbTiO_3$)-x$Pb(Sc_{1/2}Nb_{1/2})O_3$ Crystals 87
5.1. Abstract 87
5.2. Introduction...87
5.3. Single Crystal Growth 89
5.4. Growth Result, Crystal Morphology, and Structural Analysis 92
5.5. Optical Domain Structure, Phase Symmetry and Phase Transition 96
5.6. Ferroelectric and Piezoelectric Properties.....................................98
5.7. Conclusions 100

Chapter 6. Conclusions 102

References...105

List of Tables

Table 2.1: Symmetry names, unit cell parameters, and angles for the seven crystal systems. 21

Table 3.1: Phase and variations of the 'a_R' and 'α_R' lattice parameters, and volume of the unit cell (V_R) as a function of $BiScO_3$ content for the (1-x)$Pb(Sc_{1/2}Nb_{1/2})O_3$-x$BiScO_3$ solid solutions. 39

Table 3.2: Comparison of the apparent density, theoretical density, and relative density of the (1-x)$Pb(Sc_{1/2}Nb_{1/2})O_3$-x$BiScO_3$ solid solution ceramics. 42

Table 3.3: FWHMs of the dielectric peaks calculated for f = 100 kHz; T_C/T_{max} obtained from dielectric measurements upon heating and cooling; ΔT_{max} values obtained from dielectric measurements upon cooling. Errors were determined by the step size of the dielectric temperature measurements. 46

Table 3.4: Ferroelectric and piezoelectric properties of the (1-x)$Pb(Sc_{1/2}Nb_{1/2})O_3$-x$BiScO_3$ solid solutions measured at room temperature: E_C = Coercive Field, P_S = Saturation Polarization, P_r = Remanent Polarization, d_{33} = Piezoelectric Coefficient. 52

Table 4.1: Variations of the a, c, α lattice parameters, and volume of the unit cell as a function of $Pb(Sc_{1/2}Nb_{1/2})O_3$ content for the (1-x)(0.35$BiScO_3$-0.65$PbTiO_3$)-x$Pb(Sc_{1/2}Nb_{1/2})O_3$. 64

Table 4.2: Apparent density, theoretical density, and relative density of (1-x)(0.35$BiScO_3$-0.65$PbTiO_3$)-x$Pb(Sc_{1/2}Nb_{1/2})O_3$ solid solution ceramics. 65

Table 4.3: FWHMs calculated for f = 100 kHz for the (1-x)(0.35$BiScO_3$-0.65$PbTiO_3$)-x$Pb(Sc_{1/2}Nb_{1/2})O_3$ solid solutions; $T_{C/max}$ obtained from dielectric measurement upon heating and cooling. Errors were determined by the step size of the dielectric temperature measurements. 71

Table 4.4: $T_{C/max}$ obtained from dielectric measurement upon heating and cooling. Errors were determined by the step size of the dielectric temperature measurements. ΔT_{max} represents the temperature difference between the maximum values observed at frequencies of 1 kHz and 100 kHz. Errors were determined by the step size of the dielectric temperature measurements. 74

Table 4.5: Variation in piezoelectric coefficient (d_{33}) for (1-x)(0.35$BiScO_3$-0.65$PbTiO_3$)-x$Pb(Sc_{1/2}Nb_{1/2})O_3$ ceramics with x = 0.10 and x = 0.20 and different poling temperatures and poling duration time. 78

Table 4.6: Coercive field (E_C), remanent polarization (P_r) and piezoelectric coefficient (d_{33}) of the (1-x)(0.35$BiScO_3$-0.65$PbTiO_3$)- x$Pb(Sc_{1/2}Nb_{1/2})O_3$ solid solution. E_C and P_r are obtained from the ferroelectric P-E loop measured at room temperature. 81

Table 4.7: Coercive Coercive field (E_C), remanent polarization (P_r) and piezoelectric coefficient (d_{33}) of the (1-x)(0.34$BiScO_3$-0.66$PbTiO_3$)- x$Pb(Sc_{1/2}Nb_{1/2})O_3$ solid solution. E_C and P_r are obtained from the ferroelectric P-E loop measured at room temperature. 83

Table 4.8: Coercive field (E_C), remanent polarization (P_r) and piezoelectric coefficient (d_{33}) of the (1-x)(0.36$BiScO_3$-0.64$PbTiO_3$)- x$Pb(Sc_{1/2}Nb_{1/2})O_3$ solid

solution. E_C and P_r are obtained from the ferroelectric P-E loop measured at room temperature. 84

List of Figures

Figure 1.1: Illustration of the (a) direct, and (b) converse longitudinal piezoelectric effects. 2

Figure 1.2: (a) A common polarization (P) - electric (E) hysteresis loop, illustrating the transition of spontaneous polarizations, (b) A two-dimensional representation of the Gibbs free energy G plotted against polarization.....3

Figure 1.3: The temperature-dependent dielectric constant (ε') of a ferroelectric material displaying a prominent anomaly peak at T_C, marking the transition of the ferroelectric polar phase to the paralelectric non-polar phase within a perovskite unit cell. 4

Figure 1.4: The perovskite ABO_3 crystal structure in its cubic paraelectric phase (a = b = c), (b) The same perovskite in its tetragonal ferroelectric phase (a = b ≠C). 6

Figure 1.5: Phase diagram of the solid solution $PbZr_{1-x}TixO_3$ around the morphotropic phase boundary (MPB). 9

Figure 1.6: Temperature-dependent variation in the dielectric constant (ε') of a representative relaxor ferroelectric material. T_{m1} signifies the dielectric peak observed at 1 Hz, while T_{m2} represents the peak at 100 kHz. 11

Figure 1.7: Development of perovskite-based piezoelectric materials with respect to their piezoelectric constants d_{33}. 13

Figure 1.8: Variation in the piezoelectric coefficient d_{33} in relation to Curie temperature for relaxor-PT single crystals, PZT ceramics, and single crystal piezo-/ferroelectric perovskite materials. 15

Figure 2.1: Schematic illustration of Bragg's laws derivation from a set of lattice planes with interplanar spacing (d) and the diffraction of X-rays by a crystal. 20

Figure 2.2: Defining lattice parameters and angles within a crystal unit cell. 21

Figure 2.3: Frequency response analyzer circuit for dielectric spectroscopy. 24

Figure 2.4: Illustration of the loss angle δ in relation to the real and imaginary components of the dielectric permittivity. 25

Figure 2.5: Schematic representation of a customized Sawyer-Tower circuit adapted for the precise measurement of ferroelectric hysteresis loops. The symbols C_s, R_s, C_r, R, V, and V_r denote the sample's capacitance, sample resistance, reference capacitance, resistor, step voltage, and voltage across the reference capacitor, respectively. 26

Figure 2.6: Schematic for measuring d_{33} using quasi-static method. 28

Figure 2.7: Schematic of Helium Ion Microscopy (HIM) imaging system. 29

Figure 2.8: Principle and configuration of polarized light microscopy (PLM). 30

Figure 3.1: Powder X-Ray diffraction (XRD) patterns of $(1-x)Pb(Sc_{1/2}Nb_{1/2})O_3-xBiScO_3$ after calcination measured at room temperature, with the reference pattern of pure $Pb(Sc_{1/2}Nb_{1/2})O_3$ (PDF # 80922) displayed. 37

Figure 3.2: Room temperature X-ray diffraction (XRD) patterns of the $(1-x)Pb(Sc_{1/2}Nb_{1/2})O_3-xBiScO_3$ solid solution ceramics after sintering, with

the reference pattern for pure $Pb(Sc_{1/2}Nb_{1/2})O_3$ (PDF # 80922) shown for comparison. 38

Figure 3.3: Results of Rietveld refinement fitting of the high-resolution X-ray diffraction data of the $(1-x)Pb(Sc_{1/2}Nb_{1/2})O_3-xBiScO_3$ solid solution: (a) x = 0, (b) x = 0.10. 39

Figure 3.4: Variations of the room-temperature 'a_R' and 'α_R' lattice parameters, as a function of $BiScO_3$ content for the $(1-x)Pb(Sc_{1/2}Nb_{1/2})O_3-xBiScO_3$ solid solution. 40

Figure 3.5: Helium ion microscopy (HIM) images of the sintered $(1-x)Pb(Sc_{1/2}Nb_{1/2})O_3-xBiScO_3$ solid solution ceramics with various compositions: (a) x = 0 with 500 nm scale, (b) x = 0.10 with 5 μm scale, and (c) x = 0.20 with 5 μm scale, (d) x = 0.10 with 2μm scale, and (e) x = 0.20 with 20μm scale. Grain size distribution and average grain sizes of the ceramics calculated using Image J software: (f) x = 0.00, (g) x = 0.10, (h) x = 0.20. Variation of the average grain size with $BiScO_3$ mole content. 42

Figure 3.6: Variation of dielectric constant ε' and loss tangent tan δ as a function of temperature for the $(1-x)Pb(Sc_{1/2}Nb_{1/2})O_3-xBiScO_3$ solid solutions: (a) x = 0.00, (b) x = 0.05, (c) x = 0.10, (d) x = 0.15 and (e) x = 0.20, measured at the frequencies of 1 kHz, 10 kHz, and 100 kHz upon cooling. Variations of the dielectric constant ε' as a function of temperature of all the compositions measured at f = 100 kHz (f). 45

Figure 3.7: Variations of the Curie/maximum temperatures (T_C/T_{max}) as a function of $BiScO_3$ mole content in the $(1-x)Pb(Sc_{1/2}Nb_{1/2})O_3-xBiScO_3$ solid solution measured upon heating and cooling, and variations of the ΔT_{max} as a function of $BiScO_3$ mole content upon cooling. 46

Figure 3.8: (a) Temperature dependences of the dielectric constant (ε') and loss tangent (tanδ) for $(1-x)Pb(Sc_{1/2}Nb_{1/2})O_3-xBiScO_3$ with x = 0.15 measured at various frequencies upon cooling; (b) Temperature dependences of the imaginary part of the dielectric permittivity (ε'') in the temperature range of 20-70ºC; (c) Frequency dependence of the real part (ε') of the dielectric permittivity for $(1-x)Pb(Sc_{1/2}Nb_{1/2})O_3-xBiScO_3$ with x = 0.15 measured at various temperatures. 47

Figure 3.9: Fitting of the dielectric constant as a function of temperature measured at 1 MHz to the quadratic law described in Equation 3.1 for the $(1-x)Pb(Sc_{1/2}Nb_{1/2})O_3-xBiScO_3$ ceramics: (a) x = 0.10, and (b) x = 0.15.......49

Figure 3.10: Fitting of the dielecric relaxation of the $(1-x)Pb(Sc_{1/2}Nb_{1/2})O_3-xBiScO_3$ ceramics to the Vogel-Fulcher law: (a) x = 0.10, and (b) x = 0.15. 50

Figure 3.11: Polarization-Electric field (P-E) hysteresis loops of $(1-x)Pb(Sc_{1/2}Nb_{1/2})O_3-xBiScO_3$ ceramics at 10 Hz, recorded at room temperature: (a) x = 0.0, (b) x = 0.05, (c)x = 0.10, (d) x = 0.15, and (e) x = 0.20; and (f) variation of the coercive field (E_C), remanent polarization (P_r) and piezoelectric coefficient (d_{33}) as a function of $BiScO_3$ mole content. 51

Figure 4.1: The schematic ternary phase diagram features lead scandium niobate ($Pb(Sc_{1/2}Nb_{1/2})$, PSN), bismuth scandium ($BiScO_3$, BS), and lead titante ($PbTiO_3$, PT) as end members and their respective structural symmetries. Blue dots represent the compositions studied in this research. 57

Figure 4.2: Powder X-ray diffraction patterns obtained at room temperature of the (1-x)(0.35$BiScO_3$-0.65$PbTiO_3$)-x$Pb(Sc_{1/2}Nb_{1/2})O_3$ solid solution: (a) compositions of x = 0 - 0.30, and (b) their zoomed-in XRD patterns between 36° to 48°. 59

Figure 4.3: Powder X-ray diffraction patterns obtained at room temperature of the ceramics of (1-x)(0.34$BiScO_3$-0.66$PbTiO_3$)-x$Pb(Sc_{1/2}Nb_{1/2})O_3$: (a) Compositions of x = 0 - 0.20, (b) Their zoomed-in XRD patterns between 36° to 48°; and (1-x)(0.36$BiScO_3$-0.64$PbTiO_3$)- $Pb(Sc_{1/2}Nb_{1/2})O_3$ solid solutions: (c) Compositions of x = 0 - 0.20; and (d) Their zoomed-in XRD patterns between 36° to 46°. 61

Figure 4.4: Rietveld refinement fitting the high-resolution X-ray diffraction data of the (1-x)(0.35$BiScO_3$-0.65$PbTiO_3$)-x$Pb(Sc_{1/2}Nb_{1/2})O_3$ solid solution: (a) x = 0; (b) x = 0.20. 63

Figure 4.5: Variations of the room-temperature 'a' and 'c' lattice parameters, 'α_R' Rhombohedral angle, 'c/a', and 'V' as a function of $Pb(Sc_{1/2}Nb_{1/2})O_3$ content for the (1-x)(0.35$BiScO_3$-0.65$PbTiO_3$)-x$Pb(Sc_{1/2}Nb_{1/2})O_3$ solid solution. 65

Figure 4.6: Helium ion microscopy (HIM) images of sintered (1-x)(0.35$BiScO_3$-0.65$PbTiO_3$)-x$Pb(Sc_{1/2}Nb_{1/2})O_3$ solid solution ceramics for various compositions: (a) x = 0; (b) x = 0.10; (c) x = 0.20; and (d) x = 0.30 with 10μm scale; (e) x = 0.10, (f) x = 0.30 with 20 μm as scale. 67

Figure 4.7: Average grain size values for (1-x)(0.35$BiScO_3$-0.65$PbTiO_3$)-x$Pb(Sc_{1/2}Nb_{1/2})O_3$ solid solution ceramics, determined using Image J software based on HIM images, are displayed for various compositions: (a) x = 0; (b) x = 0.10; (c) x = 0.20; (d) x = 0.30. The graph (e) illustrates the relationship between average grain size and $Pb(Sc_{1/2}Nb_{1/2})O_3$ mole content. 68

Figure 4.8: Variation of dielectric constant ε' and tan δ as a function of temperature for the (1-x)(0.35$BiScO_3$-0.65$PbTiO_3$)-x$Pb(Sc_{1/2}Nb_{1/2})O_3$ solid solutions: (a) x = 0; (b) x = 0.05; (c) x = 0.10; (d) x = 0.20; (e) x = 0.30 measured at 1 kHz, 10 kHz, and 100 kHz upon cooling; (f) variations of the dielectric constant ε' as a function of temperature on all the compositions at f = 100 kHz. 71

Figure 4.9: Variation of dielectric constant ε' and tan δ as a function of temperature for the (1-x)(0.34$BiScO_3$-0.66$PbTiO_3$)-x$Pb(Sc_{1/2}Nb_{1/2})O_3$ solid solution: (a) x = 0; (b) x = 0.10; (c) x = 0.20; and for the (1-x)(0.36$BiScO_3$-0.64$PbTiO_3$)-x$Pb(Sc_{1/2}Nb_{1/2})O_3$ solid solution: (d) x = 0; (e) x = 0.10, (f) x = 0.20 measured at 1 kHz, 10 kHz, and 100 kHz upon cooling. 74

Figure 4.10: Variations of the (a) Curie temperatures and (b) ΔT_{max} as a function of $Pb(Sc_{1/2}Nb_{1/2})O_3$ mole content for the (1-x)($BiScO_3$-$PbTiO_3$)-x$Pb(Sc_{1/2}Nb_{1/2})O_3$ solid solution, obtained from dielectric measurements upon cooling. 75

Figure 4.11: Partial structural phase diagram illustrating the behavior of (1-x)(0.35$BiScO_3$-0.65$PbTiO_3$)-x$Pb(Sc_{1/2}Nb_{1/2})O_3$ solid solution. Red dots mark Curie and maximum temperatures (T_C and T_{max}) 76

Figure 4.12: Fitting of the dielectric relaxation of the (1-x)(0.35$BiScO_3$-0.65$PbTiO_3$)-x$Pb(Sc_{1/2}Nb_{1/2})O_3$ ceramics to the Vogel-Fulcher law: (a) x = 0.10, and (b) x = 0.20. 77

Figure 4.13: Ferroelectric P-E loop of the (1-x)($0.35BiScO_3$-$0.65PbTiO_3$)-x$Pb(Sc_{1/2}Nb_{1/2})O_3$ solid solution at 10 Hz, recorded at room temperature for the compositions: a) x = 0, b) x = 0.05, c) x = 0.10, d) x = 0.20 and e) x = 0.30; and variation of the coercive field (E_C), remanent polarization (P_r) and piezoelectric coefficient (d_{33}) as a function of $Pb(Sc_{1/2}Nb_{1/2})$ mole content. 81

Figure 4.14: Ferroelectric P-E loop of the (1-x)($0.34BiScO_3$-$0.66PbTiO_3$)-x$Pb(Sc_{1/2}Nb_{1/2})O_3$ solid solution at 10 Hz, recorded at room temperature for the compositions: a) x = 0, b) x = 0.10, c) x = 0.20; and d) variation of the coercive field (E_C), remanent polarization (P_r) and piezoelectric coefficient (d_{33}) as a function of x$Pb(Sc_{1/2}Nb_{1/2})O_3$ mole content. 83

Figure 4.15: Ferroelectric P-E loop of the (1-x)($0.36BiScO_3$-$0.64PbTiO_3$)-x$Pb(Sc_{1/2}Nb_{1/2})O_3$ solid solution at 10 Hz, recorded at room temperature for the compositions: a) x=0, b) x = 0.10, c) x = 0.20; and d) variation of the coercive field (E_C), remanent polarization (P_r) and piezoelectric coefficient (d_{33}) as a function of $Pb(Sc_{1/2}Nb_{1/2})O_3$ mole content. 84

Figure 5.1: (a) Schematic illustrating the furnace and crucible assembly utilized in the high-temperature solution growth (HTSG) process for the growth of $0.1Pb(Sc_{1/2}Nb_{1/2})O_3$-$0.315BiScO_3$-$0.585PbTiO_3$ crystals; (b) Real picture of the furnace set up and ventilation system. 91

Figure 5.2: Thermal profile consisting of heating, dwelling, and cooling at variable rates used for the growth of crystals with the nominal composition of $0.1Pb(Sc_{1/2}Nb_{1/2})O_3$-$0.315BiScO_3$-$0.585PbTiO_3$ crystals by high-temperature solution growth (HTSG) method. 91

Figure 5.3: Optical images of as-grown single crystals with a nominal composition of $0.1Pb(Sc_{1/2}Nb_{1/2})O_3$-$0.315BiScO_3$-$0.585PbTiO_3$: (a) Crystals formed on the surface of solidified flux in the crucible after cooling; (b) Enlarged view of selected single crystals formed inside the flux that display growth striation; (c) Crystals grown in the middle of the flux that are revealed after leaching in 20% nitric acid for 60 minutes; (d) Selected crystals after leaching with pseudo-cubic morphology. 93

Figure 5.4: X-ray diffraction (XRD) patterns obtained from: (a) Ground powder; (b) One of the naturally grown pseudo-cubic facets, of the $0.1Pb(Sc_{1/2}Nb_{1/2})O_3$-$0.315BiScO_3$-$0.585PbTiO_3$ single crystals. 95

Figure 5.5: Domain structure of a $(001)_{cub}$ platelet of the PSN-BS-PTR single crystal observed by polarized light microscopy (PLM) at room temperature: a) Diagonal extinctions in Region 1, corresponding to the rhombohedral phase; b) Intermediate extinctions at 90° ± 21°, indicating the monoclinic symmetry in Regions 2; c) Parallel extinctions in Regions 3, suggesting the tetragonal symmetry. 97

Figure 5.6: Variations of domain structure of the $(001)_{cub}$ platelet showing phase transitions of the birefringent rhombohedral, monoclinic and tetragonal symmetries to the high temperature isotropic cubic phase. 98

Figure 5.7: Polarization-electric field (P-E) loops of the single crystals with nominal composition of $0.1Pb(Sc_{1/2}Nb_{1/2})O_3$-$0.315BiScO_3$-$0.585PbTiO_3$ measured at the frequency of 100 Hz at room temperature, under various field strengths from 20 kV/cm up to 170 kV/cm, demonstrating good ferroelectricity. 100

Figure 6.1: Variations in the piezoelectric coefficient (d_{33}) concerning the Curie temperature (T_C) across different perovskite materials. 104

List of Acronyms

BS	$BiScO_3$
d_{33}	Piezoelectric coefficient
HIM	Helium ion microscopy
MPB	Morphotropic phase boundary
PIN	$Pb(In_{1/2}Nb_{1/2})O_3$
PLM	Polarized light microscopy
PMN	$Pb(Mg_{1/3}Nb_{2/3})O_3$
PNR	Polar nanoregion
P_r	Remanent polarization
P_s	Spontaneous polarization
PSN	$Pb(Sc_{1/2}Nb_{1/2})O_3$
PT	$PbTiO_3$
PZN	$Pb(Zn_{1/3}Nb_{2/3})O_3$
PZT	$PbZr_{1-x}Ti_xO_3$
R_{exp}	Expected profile residual
R_p	Profile residual factor
R_{wp}	Weighted profile residual
tan δ	Dielectric loss
T_C	Curie temperature
T_m	Melting point temperature
T_{max}	Maximum permittivity temperature
XRD	X-ray diffraction
ε’	Dielectric constant
ε’’	Imaginary part of dielectric permittimity

Chapter 1.

Introduction

This thesis encompasses the research involving the design, synthesis, and characterization of high-temperature, high-performance perovskite materials in ceramic and single crystal forms, intended for applications in electromechanical transduction, energy storage, and memory devices. In this chapter, essential concepts such as the perovskite structure, dielectric properties, piezoelectricity, ferroelectricity, antiferroelectricity, solid solutions, and the morphotropic phase boundary (MPB) are introduced and explained. Additionally, we provide an overview of perovskite piezo-/ferroelectric materials' applications, their development, ongoing research challenges, and interests, which collectively lead to the motivation and objectives of this study.

1.1. Piezoelectric Properties

The phenomenon of piezoelectricity was first discovered by Pierre and Jacques Curie in 1880, originating from their observations on α-quartz.[1] The term "piezo" in piezoelectricity is derived from the Greek word meaning "to press," and it denotes the property of materials with specific crystal symmetry classes, enabling the conversion of mechanical energy into electrical energy and vice versa. These materials are referred to as piezoelectrics.[2] As presented in Figure 1.1, when a mechanical stress is applied to a piezoelectric material, it undergoes a change in polarization (P), resulting in the generation of electric charges, a phenomenon known as the direct piezoelectric effect, commonly used in generators and sensors. Conversely, if an electric field is applied to piezoelectrics, it induces strain (S), leading to crystal deformation, known as the converse piezoelectric effect, often utilized in motors. The magnitude of the resulting electric charges (polarization) or strain is directly proportional to the applied mechanical stress or electric field, as indicated by the piezoelectric coefficient 'd' in Equations 1.1 and 1.2:

$$P_i = d_{ij}T_j \text{ (Direct effect)} \qquad (1.1)$$

$$S_i = d_{ij}E_j \text{ (Converse effect),} \quad (1.2)$$

where electric polarization induced is P_i, the stress applied is T_i, the strain induced is S_i, the electric field applied is E_i, and d_{ij} is the piezoelectric coefficient. For d_{ij}, 'i' and 'j' are used in a special notation for crystal properties. Longitudinal coefficients (ij = 11, 22, 33) are associated with measurements in the direction of the applied electric field, while transverse coefficients (ij = 12, 23, 31) pertain to measurements perpendicular to the field. The remaining coefficients are called shear coefficients (ij = 14, 15, 16, …,35, 36).[3]

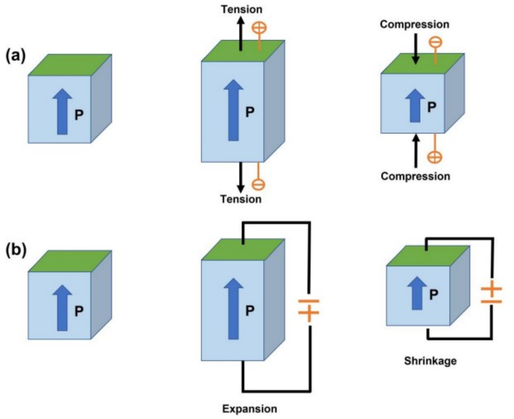

Figure 1.1: Illustration of the (a) direct, and (b) converse longitudinal piezoelectric effects.

1.2. Ferroelectric Properties

Ferroelectrics are a class of piezoelectric materials that exhibit a spontaneous polarization which is reorientable under an external electric field. Ferroelectricity is a remarkable property found in certain materials, where spontaneous polarization can be reversed by the application of electric fields. This behavior is often characterized by the polarization-electric field hysteresis loop, as depicted in Figure 1.2 (a), in an unpoled ferroelectric material, the spontaneous polarizations are randomly oriented, leading to a near-zero total spontaneous polarization. However, when an electric field is applied, these polarizations align with the field, resulting in a saturation polarization known as P_S or P_{max}. These aligned polarizations persist in the same direction even as the electric field is reduced to zero, a state referred to as the "poled" status. The remaining spontaneous polarization is termed remnant polarization (P_r). Removing P_r necessitates applying an electric field with the opposite direction, known as the coercive field (E_C). Both E_C and P_r are crucial parameters for describing and measuring a material's ferroelectricity. Larger values of these parameters indicate stronger ferroelectric properties. The coercive field, saturation polarization, remnant polarization, and hysteresis loop shape can be influenced by various factors, including sample thickness, microstructures, grain sizes, defects, mechanical stress, and preparation conditions.[4–6]

From an energy perspective, as depicted in Figure 1.2 (b), when the spontaneous polarization aligns with the electric field direction, the system attains its lowest free energy state, making it the preferred configuration. This preference results in the formation of a double well curve in the Gibbs free energy versus spontaneous polarization when subjected to an electric field. Conversely, when an electric field of the opposite direction is applied, the double well potential becomes more favorable in minimizing energy, prompting the polarization to switch in the opposite direction. This phenomenon gives rise to the characteristic P-E hysteresis loop.[7]

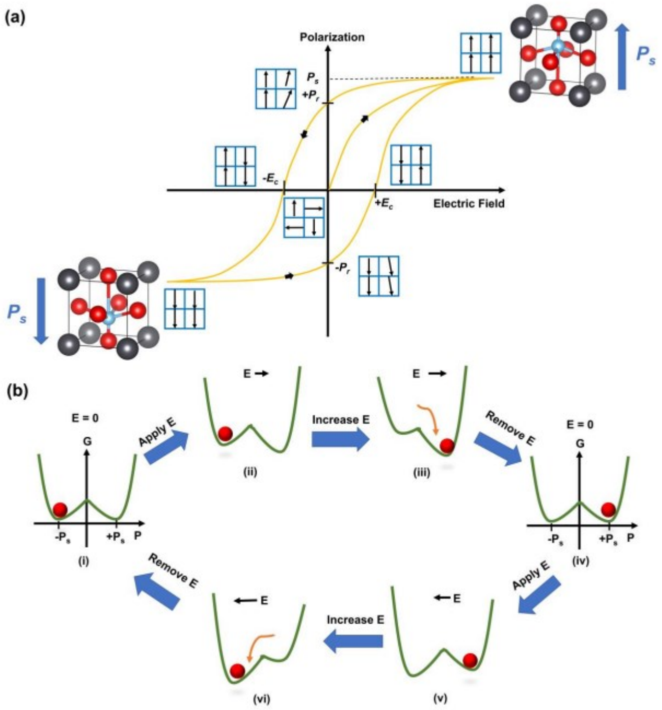

Figure 1.2: **(a) A common polarization (P) - electric (E) hysteresis loop, illustrating the transition of spontaneous polarizations, (b) A two-dimensional representation of the Gibbs free energy G plotted against polarization.**

Ferroelectric materials experience a phase transition from their ferroelectric polar phase to a paraelectric non-polar cubic phase as they are heated, resulting in changes to the crystal unit cell dimensions and anomalies in various material properties such as dielectric, elastic, thermal, and optical characteristics. This critical temperature of transition is referred to as the Curie temperature (T_C) as presented in Figure 1.3. Higher T_C values are desirable for wider temperature range applications. The phase transition behavior at T_C can be categorized as first or second order. In a second-order transition, there is a continuous change in spontaneous polarization as the material passes through T_C, which is evident in the Gibbs free energy plot versus polarization. In contrast, a first-order transition involves a discontinuous change in spontaneous polarization at T_C, leading to distinct free energy characteristics. These transitions are linked to anomalies observed in material properties as temperature varies around T_C.[4]

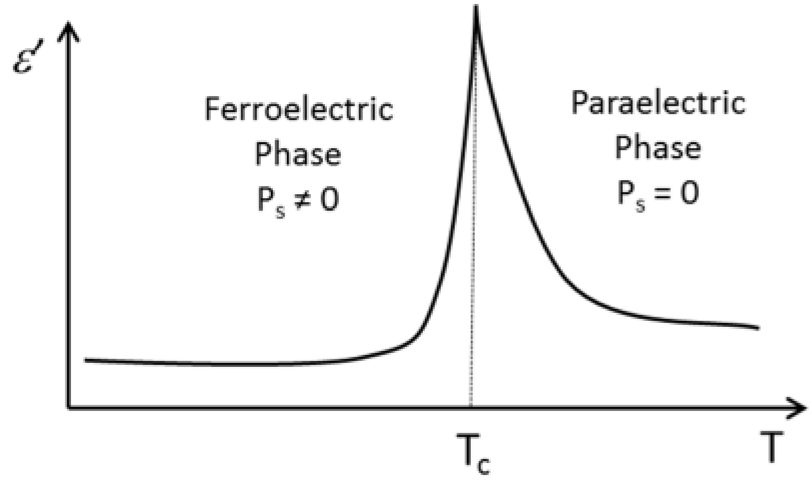

Figure 1.3: The temperature-dependent dielectric constant (ε') of a ferroelectric material displaying a prominent anomaly peak at T_C, marking the transition of the ferroelectric polar phase to the paralelectric non-polar phase within a perovskite unit cell.

1.3. Applications of Piezo-/ferroelectric Materials

Piezo-/ferroelectric materials, renowned for their exceptional properties, find applications spanning a multitude of industries and everyday life. Among their notable applications is in capacitors, where their high relative permittivity, typically within the range of 10^2 to 10^4, makes them a preferred choice. Additionally, these materials play a pivotal role in memory devices, especially in ferroelectric random-access memory (FeRAM). FeRAM capitalizes on the reversible polarization in ferroelectrics, with negative and positive remanent polarizations representing binary states "0" and "1," respectively. This technology boasts several advantages, including low power consumption and rapid write and read cycle times, typically under 100 nanoseconds.

Moreover, the direct and converse piezoelectric effects are widely applied in sensors and actuators. These phenomena find utility in various applications such as atomic force microscopy cantilevers, acoustic sensors, ultrasonic transducers for medical imaging, and sonar systems.[7–9] Additionally, the burgeoning field of energy harvesting leverages the direct piezoelectric effect, converting mechanical vibrations into electrical energy. This technology is utilized in innovations like piezoelectric shoe inserts, enabling energy harvesting from walking, and devices that harness energy from ocean waves.[10,11] In our daily lives, piezo-/ferroelectric materials can be found in everyday devices, from inkjet printers, camera shutters, and loudspeakers to automotive components like mirror adjusters, piezoelectric fuel injectors, tire pressure sensors, and engine knock detectors.

Perovskite materials, celebrated for their exceptional piezo-/ferroelectric performance, play a pivotal role in numerous applications. They are harnessed in electromechanical devices, capacitors, and non-volatile memory devices across various forms, including ceramics, thin films, single crystals, textured ceramics, polymers, and composites. Among these materials, relaxor-$PbTiO_3$-based ferroelectric single crystals like PMN-PT and PZN-PT are particularly noteworthy due to their exceptional piezoelectric properties.

Furthermore, perovskites with robust ferroelectric characteristics, such as $BaTiO_3$, are highly desirable for capacitors, especially multilayer capacitors (MLC) in electronic devices, given their high dielectric constants. Moreover, ferroelectric perovskites like PZT are crucial in non-volatile memory applications, serving as random-access memory films with switchable polarizations, vital for computer random-access memories, smart cards, and radio-frequency identification tags. The pyroelectric properties of ferroelectric perovskites also make them well-suited for infrared sensing devices.

1.4. Perovskite Structure

Perovskite materials are fundamental in the realm of functional materials, playing a significant role in the study of various piezo-/ferroelectric substances. A majority of these important materials crystallize in the perovskite structure, which forms the foundation of our research in this thesis. This perovskite structure is characteristic of compounds with the general chemical formula ABX_3, where 'A' denotes a larger 12-coordinated cation, 'B' represents a smaller 6-coordinated cation, and 'X' is typically oxygen anions, though other anions like F^-, Cl^-, and S^{2-} can also be present. The most extensively studied piezo-/ferroelectric materials are perovskite oxides, a category exemplified by the structure of the mineral calcium titanate ($CaTiO_3$). In a cubic ABO_3 perovskite unit cell, large 'A' cations are typically positioned at the cube's corners (A site), small 'B' cations occupy the cube's center (B site), and oxygen atoms are located at the face centers of the cube. Perovskites that can exhibit ferroelectric behaviour exist in the cubic paraelectric phase above the Curie temperature (T_C) but transition to lower symmetry structures like the ferroelectric tetragonal phase below T_C (Figure 1.4).

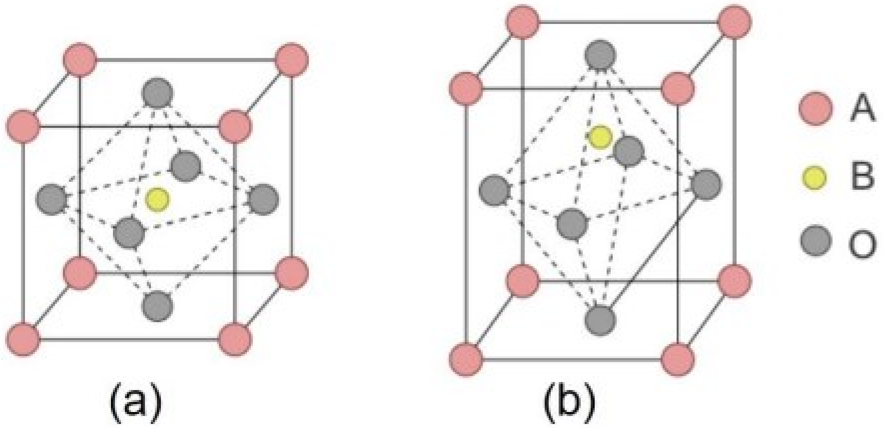

Figure 1.4: The perovskite ABO_3 crystal structure in its cubic paraelectric phase (a = b = c), (b) The same perovskite in its tetragonal ferroelectric phase (a = b ≠C).

The stability and distortion of perovskite structures are significantly influenced by the sizes of ions comprising the structure. While the idealized cubic perovskite structure, is depicted in Figure 1.4 (a), real-world perovskites often exhibit more pronounced distortions.

To gauge the degree of distortion, the empirical Goldschmidt's tolerance factor (t) is a valuable metric. It is calculated using the following equation:

$$t = \frac{R_A + R_O}{\sqrt{2}(R_B + R_O)} \quad (1.3)$$

where R_A, R_B, and R_O represent the ionic radii of the A, B, and O^{2-} ions, respectively. In practice, perovskite structures tend to remain stable within the tolerance factor range of 0.8 to 1.1. If t exceeds 1.1, the perovskite structure is inclined to distort into a hexagonal 2H-$BaNiO_3$ structure, while values of t less than 0.8 often lead to distortions toward structures like corundum (α-Al_2O_3) and its derivatives. When t equals 1, the perovskite structure becomes cubic.

The tolerance factor, apart from ionic size, can also be influenced by various other factors like the presence of vacancies, local ionic environment, the Jahn-Teller effect, pressure, and temperature, all contributing to the distortion of the perovskite structure.

1.5. PZT Solid Solution and Morphotropic Phase Boundary (MPB)

A solid solution is a crystalline phase with variable composition achieved by either substituting new atoms or ions into equivalent positions or introducing atoms or ions into typically vacant sites. The solid solutions discussed in this thesis primarily involve substituting different cations for the A and B crystallographic sites in the perovskite structure, enabling the creation of new solid solutions with tailored structures and properties. This substitution process is represented by the equation:

$$(1-x)ABO_3 + xA'B'O_3 \rightarrow A_{(1-X)}A'_xB_{(1-x)}B'_xO_3$$

A solid solution represents a continuous sequence of substances with compositions falling between two distinct end members. In solid-solution series, the components can be thought of as mutually substituting within the crystal structure, resulting in intermediate members with properties that smoothly transition from one end member to the other. A practical illustration of this concept is the formation of a solid solution by reacting the two end members PbZrO3 and PbTiO3:

$$(1-x)PbZrO_3 + xPbTiO_3 \rightarrow Pb(Zr_{1-x}Ti_x)O_3$$

PZT ($PbTi_xZr_{(1-x)}O_3$) is a renowned perovskite solid solution known for its exceptional piezo-/ferroelectric performance. This material bridges the characteristics of two perovskite end members, $PbTiO_3$ and $PbZrO_3$. While $PbTiO_3$ boasts a ferroelectric tetragonal phase with a high Curie temperature (T_C = 490 °C), it suffers from limited piezoelectric capabilities due to its pronounced tetragonality. On the other hand, $PbZrO_3$, as discussed earlier, exhibits an antiferroelectric orthorhombic phase characterized by zero net polarization.

By substituting $PbZrO_3$ with $PbTiO_3$, a compositional phase transition occurs, progressing from the orthorhombic antiferroelectric phase to a rhombohedral ferroelectric phase and then to an intermediate phase, ultimately leading to the tetragonal ferroelectric phase with increasing $PbTiO_3$ content. This intermediate phase, often referred to as the morphotropic phase boundary (MPB), harbors coexisting rhombohedral, tetragonal, and monoclinic structures, as depicted in Figure 1.5.[12] The temperature at which this phase transition unfolds within the MPB composition is termed T_{MPB}, with higher T_{MPB} values favored in practical applications to ensure stable dielectric and piezo-/ferroelectric performance. Remarkably, the MPB compositions of PZT solid solution exhibit significantly enhanced dielectric and piezoelectric responses. This enhancement is attributed to the presence of the monoclinic phase, which serves as a bridge connecting rhombohedral and tetragonal polarization rotational directions. This unique configuration allows for a broader range of polarization states by reducing and flattening the energy profile, thereby boosting electromechanical performance.

Furthermore, the discovery of multiple symmetries within the MPB region are not limited to PZT but also extend to other lead-based solid solutions, such as $Pb(Mg_{1/3}Nb_{2/3})O_3$-$PbTiO_3$ (PMN-PT) and $Pb(Zn_{1/3}Nb_{2/3})O_3$-$PbTiO_3$ (PZN-PT).

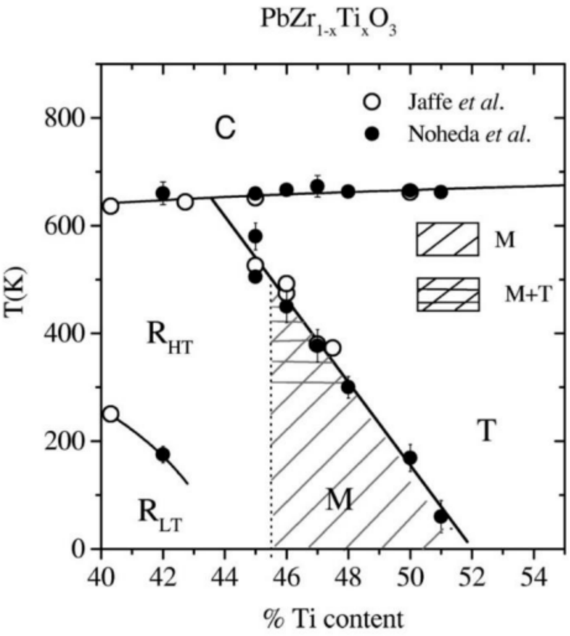

Figure 1.5: Phase diagram of the solid solution $PbZr_{1-x}TixO_3$ around the morphotropic phase boundary (MPB).

Note: reproduced from Ref[12] with the permission from the American Physical Society and the Scientific Publishing.

1.6. Relaxor Ferroelectrics

First reported in 1961, relaxor materials have found applications beyond conventional ferroelectrics. Their outstanding dielectric constants make them ideal candidates for use in multilayer capacitors, among other applications. Relaxor ferroelectric materials such as $Pb(Mg_{1/3}Nb_{2/3})O_3$ (PMN), have become a subject of increased interest in recent times, thanks to their unique nanostructures and remarkable properties. Unlike conventional ferroelectrics with long-range dipole ordering, relaxors exhibit a diffuse phase transition. They are characterized by a broad peak in dielectric permittivity with pronounced frequency dispersion below the temperature of maximum permittivity (T_{max}) as illustrated in Figure 1.6. This unique behavior arises from the arrangement of dipoles in polar nanoregions (PNRs) on a nanometer scale due to local structural heterogeneity. As a result, relaxor ferroelectrics demonstrate superior dielectric and piezoelectric responses compared to normal ferroelectrics, making them highly valuable in electromechanical transduction applications. The presence of these polar nanoregions (PNRs) has been verified through detailed high-resolution diffraction investigations and the analysis of diffuse scattering patterns in the vicinity of Bragg peaks. Various models[8,13–15] have been created to elucidate the origins and processes responsible for PNR formation and the relaxor behavior. However, it's essential to note that these mechanisms remain incompletely comprehended and are frequently a subject of controversy.[16,17]

Cross introduced a superparaelectric model for relaxor ferroelectrics, drawing an analogy to the superparamagnetic state[8]. In this model, he proposed that at elevated temperatures, micro polar regions undergo dynamic disorder due to thermal activation between different polarization states. The activation energy barrier's height is directly linked to the polar region's volume. As the temperature decreases, those regions with activation energy lower than kT (where k represents the Boltzmann constant) freeze into a preferred orientation associated with the ferroelastic state, resulting in the formation of polar microdomains.

Furthermore, Vielhand and Cross extended the superparaelectric model to explain the variation in T_{max} concerning the AC measurement frequency (f), employing the Vogel-Fulcher (VF) relationship[14]:

$$f = f_0 \exp\left[{-E_a}/{T_{max} - T_f}\right], \quad (1.4)$$

where f is the measurement frequency, and f_0, E_a (activation energy) and T_f (freezing temperature) are the fitting parameters.[8] Bokov et al. introduced an alternative empirical description of relaxor ferroelectrics in 2012. According to this definition, relaxor ferroelectrics are characterized by the observance of the Vogel-Fulcher law for T_{max} (as described in Equation 1.4) and the quadratic law for permittivity (as indicated in Equation 1.5, provided below).

$$\frac{\varepsilon_A}{\varepsilon'} = 1 + \frac{(T-T_A)^2}{2d^2}\,. \qquad (1.5)$$

In this equation, T_A (< T_{max}) represents the temperature where the fitting curve is located, and ε_A (> ε_{max}) indicates the extrapolated value of ε' at T = T_A. Additionally, d is a measure of the peak's diffuseness.[8,14,18] Notably, the steep slope in permittivity at high temperatures is generally frequency independent. Consequently, the parameters T_A, ε_A, and d derived from fitting this segment are also not influenced by frequency variations.[19]

The permittivity of relaxors is primarily influenced by two key contributions: conventional relaxor polarization and universal relaxor polarization. Conventional relaxor polarization involves the reorientation of dipole moments within PNRs and contributes significantly, typically accounting for 80-90% of the total dielectric constant. The remaining portion is mainly attributed to universal relaxor polarization, the nature of which remains a subject of debate but is thought to involve the relaxation of mobile charge carriers. Notably, at high frequencies, the contribution from universal relaxation becomes negligible.

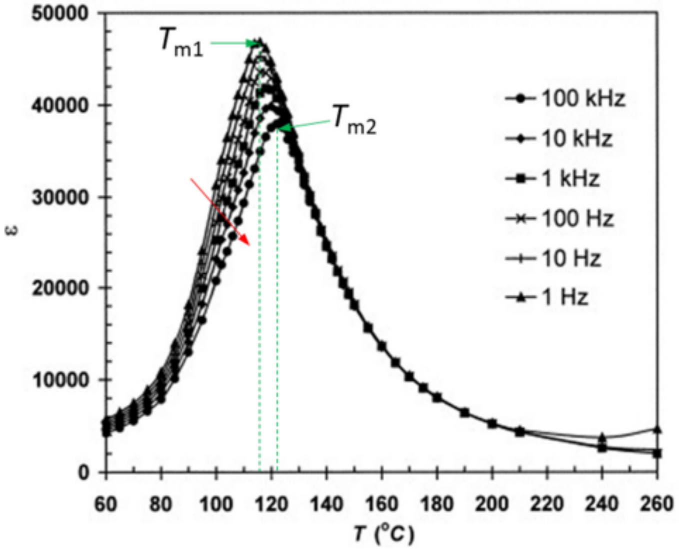

Figure 1.6: **Temperature-dependent variation in the dielectric constant (ε') of a representative relaxor ferroelectric material. T_{m1} signifies the dielectric peak observed at 1 Hz, while T_{m2} represents the peak at 100 kHz.**

1.7. Development of Piezo-/ferroelectric Materials

The journey of piezo-/ferroelectric materials through history has been a story of remarkable discovery and continuous development (Figure 1.7). It all began in 1880 when Pierre and Jacques Curie unearthed the piezoelectric effect in α-quartz (α-SiO_2) crystals[1]. Although these crystals, commonly used in telecommunications for their precise vibration frequencies, exhibited piezoelectricity, their piezoelectric coefficient is quite low at d_{11} ~ 2.3 pC/N. A significant breakthrough came with the synthesis of Rochelle salt ($KNaC_4H_4O_6 \cdot 4H_2O$) in 1921. Valasek's discovery revealed its ferroelectric and greatly enhanced piezoelectric properties with d_{14} = 345 pC/N. Despite this, Rochelle salt’s hygroscopic and thermally unstable nature hindered its practical applications.[20,21]

In the early 1940s, the landscape of piezo-/ferroelectric materials underwent a transformative shift with the discovery of barium titanate ($BaTiO_3$) by Von Hippel and Goldman. $BaTiO_3$ marked the entry into the perovskite era, and its single crystal, grown in 1947, exhibited a piezoelectric coefficient of d_{33} = 86 pC/N[22]. Although it was a significant milestone, $BaTiO_3$ presented challenges due to multiple phase transitions before its Curie temperature (T_C) and a small coercive field (E_C), making it less suitable for electromechanical transduction applications. In the 1950s, a groundbreaking achievement came with the development of the $PbTi_xZr_{(1-x)}O_3$ (PZT) perovskite solid solution[23,24]. This marked the first discovery of the morphotropic phase boundary (MPB) and introduced PZT as an industrially valued piezo-/ferroelectric material. With strong piezoelectric and dielectric responses in the MPB compositions, along with high Curie temperatures, PZT became a cornerstone in this field.

In the 1970s, Newnham introduced the concept of "engineered biphasic connectivity," paving the way for the creation of piezoelectric composites. These innovative materials brought together single crystals and ceramics, combining them with inert polymers. The result was materials that provided increased flexibility and adaptability in terms of acoustic impedance, making them highly practical for a wide range of transduction applications[25,26]. The late 20th century to the early 21st century witnessed another pivotal development with the emergence of relaxor-based perovskite ferroelectrics, particularly $Pb(Mg_{1/3}Nb_{1/3})O_3$-$PbTiO_3$ (PMN-PT) and $Pb(Zn_{1/3}Nb_{1/3})O_3$-$PbTiO_3$ (PZN-PT) solid solution single crystals. These materials displayed ultrahigh piezoelectric coefficients (d_{33}) in the range of 1500 to 2500 pC/N, high strain levels, and outstanding electromechanical coupling factors exceeding 90%, surpassing PZT ceramics.[27–30]

The journey of development in this field continued with extensive research into various high-performance relaxor-PT single crystal systems, including binary and ternary systems like $Pb(Sc_{1/2}Nb_{1/2})O_3$-$PbTiO_3$ (PSN-PT), $Pb(In_{1/2}Nb_{1/2})O_3$-$PbTiO_3$ (PIN-PT), and $Pb(Yb_{1/2}Nb_{1/2})O_3$-$PbTiO_3$ (PYN-PT).[28,31] Researchers also explored the doping of rare earth ions which led to significant advancements in piezoelectric coefficients. In 2019, the doping of Samarium into PMN-PT single crystals set yet another milestone, achieving even higher piezoelectric coefficients ranging from 3400 to 4100 pC/N.[32] These developments underscore the incredible progress and potential of piezo- and ferroelectric materials in modern technology and industry.

In more recent years, the exploration of relaxor ferroelectrics has added another dimension to the field. As previously mentioned, these materials, characterized by a diffused phase transition and unique nanostructures, have exhibited extraordinary properties. The concept of the superparaelectric model and the Vogel-Fulcher relationship has contributed to a deeper understanding of relaxor behavior. Ongoing research seeks to unlock the full potential of these materials for applications such as electromechanical transduction.

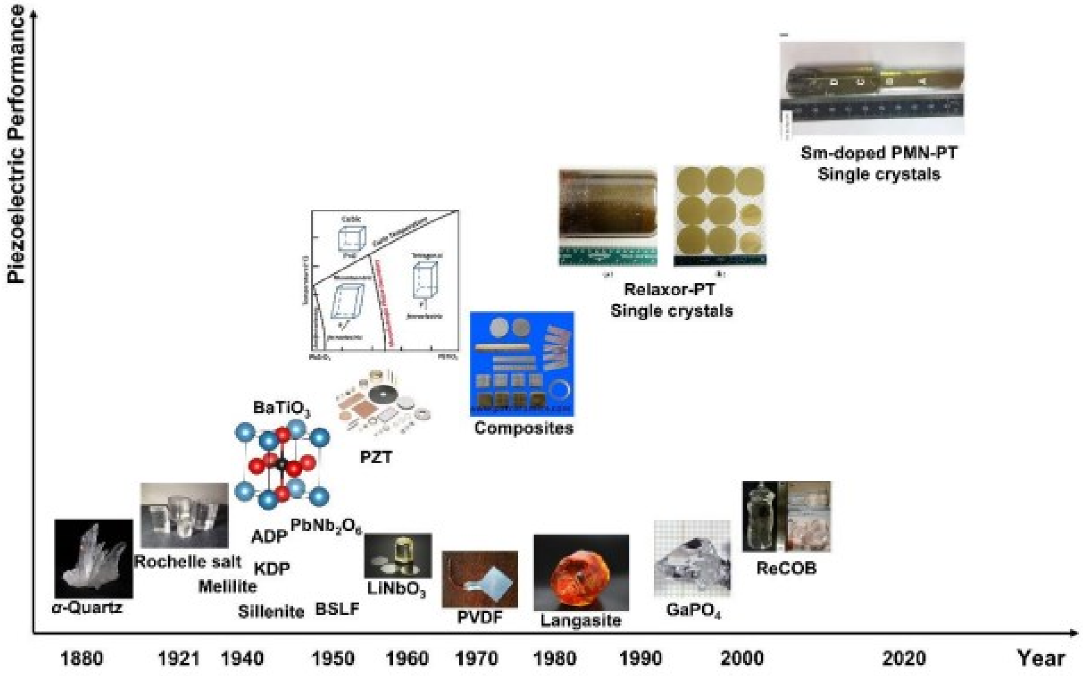

Figure 1.7: Development of perovskite-based piezoelectric materials with respect to their piezoelectric constants d_{33}.

Note: diagram sources are from Ref [46, 72-75] [79, 97, 98] with reuse permission for the purpose of research.

1.8. Limitations of Leading Piezo/ferroelectric Materials and Challenges

While piezo-/ferroelectric materials have been developed significantly over the years, they still face limitations which restrict their use, especially in today's rapidly evolving industries such as automotive, aerospace, and energy. The demand for high-temperature electromechanical piezo-/ferroelectric materials has grown with these developments, presenting new challenges for current piezo-/ferroelectric materials. Both industry and the scientific community recognize the need for piezo-/ferroelectric materials that can operate effectively over a wider temperature range. Specifically, there is a demand for piezo-/ferroelectric materials with high Curie temperatures (exceeding 400°C) to meet the requirements of non-destructive structural health monitoring, sensing, and transduction in critical applications like aircraft and automobile turbine/engine components, oil drilling, and nuclear/electrical power plants.

The Figure 1.8 depicts the relationship between the piezoelectric coefficient d_{33} and the Curie temperature (T_C) for prominent piezo-/ferroelectric perovskite materials, including relaxor-PT single crystals, PZT-related ceramics, and single crystals. Notably, a general trend emerges where higher d_{33} values are associated with lower T_C, presenting a challenge in developing piezo-/ferroelectric materials with high-temperature and high-performance.

Relaxor-PT single crystals like PMN-PT and PZN-PT exhibit exceptional piezoelectric properties, featuring d_{33} values surpassing 1500 pC/N and electromechanical coupling factors (k_{33}) exceeding 90%. However, their T_Cs fall below 200°C, with even lower phase transition temperatures (T_{MPB}) below 100°C, which constrains their use in high-temperature electromechanical applications. PZT-related materials, renowned for their piezo-/ferroelectric qualities, are also constrained by their T_C range of 150 - 360 °C, and PZT ceramics are susceptible to depoling and aging concerns within 200°C.

Another concern arises when considering high-power applications of piezo-/ferroelectric materials. These materials are extensively employed in various applications such as ultrasonic motors, transformers, underwater acoustic transducers, and medical ultrasonic uses like acoustic radiation force impulse imaging and ultrasound-guided high-intensity focused ultrasonic therapy. In these applications, piezo-/ferroelectric materials must withstand high electric fields, which necessitates low dielectric and mechanical losses and the ability to endure substantial coercive fields. However, the piezoelectric materials currently in use, like PMN-PT and PZN-PT single crystals, exhibit relatively low coercive fields, typically around 2 - 3 kV/cm. This limitation significantly restricts their application in high electric field applications.

Moreover, many high-performance piezo-/ferroelectric perovskite materials contain lead, which raises concerns due to its toxicity. High lead exposure can harm health and cause pollution when such materials are disposed of. Regulations such as the restriction of hazardous substances (RoHS) launched by the European Union, restrict hazardous substance use, highlighting the need for lead-free or lead-reduced alternatives.

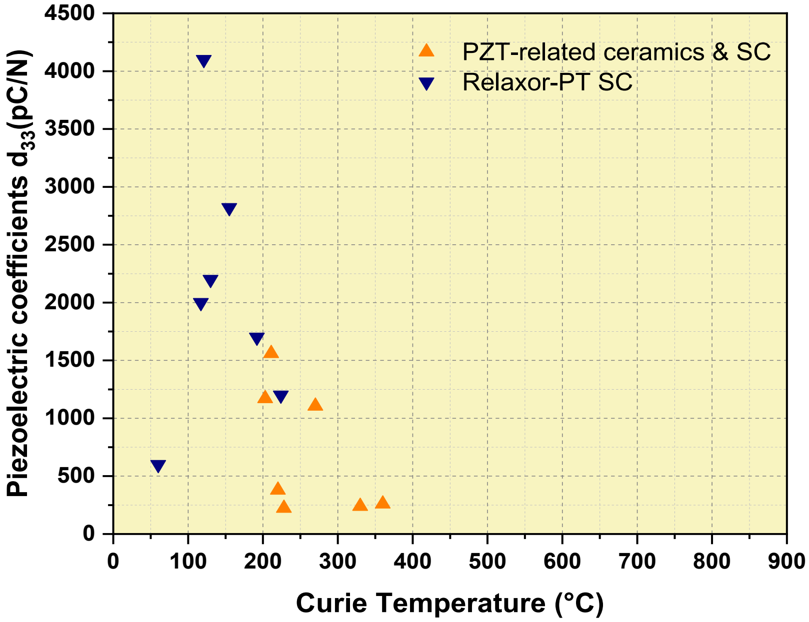

Figure 1.8: Variation in the piezoelectric coefficient d_{33} in relation to Curie temperature for relaxor-PT single crystals, PZT ceramics, and single crystal piezo-/ferroelectric perovskite materials.

Note: the data source of relaxor-PT single crystals are extracted from Ref [22-26], [41, 45-48]; the data source of PZT-related ceramics and single crystals are extracted from Ref [83], [87-89].

To address the challenges of low Curie temperature (T_C), low morphotropic phase boundary temperature (T_{MPB}), low coercive field, and lead toxicity, considerable research has focused on developing lead-free alternatives for perovskite materials without compromising piezoelectric performance. Bismuth-based perovskite solid solutions have shown promise, with T_C exceeding 400°C and strong piezoelectric properties. These materials have a general formula of $BiMeO_3$ or $BiMe'Me''O_3$, where Me or Me'Me'' represents metallic elements with an average valence of +3. In the structure of a bismuth-based perovskite unit cell, Bi^{3+} has emerged as a viable substitute for Pb^{2+} on the A-site of the perovskite structure due to its environmental friendliness and its possession of sterochemically active $6S^2$ lone pair electrons. These lone pair electrons play a crucial role in enhancing polarization within the perovskite structure and elevating Curie temperatures. Additionally, the smaller ionic radius of Bi^{3+} compared to Pb^{2+} allows for more significant cationic displacement at the A-site, resulting in a more pronounced polarization enhancement effect.[33,34] However, pure bismuth-based perovskites are challenging to synthesize under standard conditions due to the smaller ionic radius of Bi^{3+} compared to Pb^{2+}, causing structural instability. To overcome this, stable ferroelectric perovskite $PbTiO_3$, with a high Curie temperature (T_C = 490°C), is often incorporated to stabilize $BiMeO_3$ in perovskite solid solutions.

In the 1980s, bismuth-based $PbTiO_3$ perovskite solid solutions like $Bi(Zn_{2/3}Nb_{1/2})O_3$-$PbTiO_3$ and $Bi(Mg_{2/3}Nb_{1/3})O_3$-$PbTiO_3$ were pioneered, showcasing substantially elevated Curie temperatures (T_C > 400°C) compared to their lead-based counterparts. In recent decades, various bismuth-based $PbTiO_3$ perovskite solid solutions with morphotropic phase boundary (MPB) regions, such as $BiScO_3$-$PbTiO_3$ (BS-PT), $Bi(Ni_{1/2}Zr_{1/2})O_3$-$PbTiO_3$, and $Bi(Mg_{1/2}Ti_{1/2})O_3$-$PbTiO_3$, have been developed. They exhibit higher Curie temperatures than PZT and competitive piezoelectric performance (d_{33} = 150 - 450 pC/N) in their MPB regions, making them attractive for high-temperature electromechanical applications. Notably, $BiFeO_3$-$PbTiO_3$ and $Bi(Zn_{1/2}Ti_{1/2})O_3$-$PbTiO_3$ stand out with their ultrahigh tetragonality (c/a > 1.10) and Curie temperatures (600-836 °C), while $BiScO_3$-$PbTiO_3$ impresses with a 450 °C Curie temperature and exceptional piezoelectric properties (d_{33} = 460 pC/N) at its MPB compositions.

These bismuth-based perovskites have attracted significant research interest in understanding their structure, physical property differences, and structure-property correlations compared to their lead-based counterparts. Recent efforts have led to the growth of bismuth-based $PbTiO_3$ solid solution single crystals, such as $BiScO_3$-$PbTiO_3$, $Bi(Zn_{1/2}Ti_{1/2})O_3$-$PbTiO_3$, $Bi(Zn_{2/3}Nb_{1/3})O_3$-$PbTiO_3$, and $Bi(Mg_{1/2}Ti_{1/2})O_3$-$PbTiO_3$, which exhibit high Curie temperatures and excellent piezoelectric performance.[35–37]

1.9. Objectives and Organization of the Thesis

Several $BiMeO_3$-$PbTiO_3$ solid solutions have been developed so far, but the $BiScO_3$-PbTiO (BS-PT) solid solution stands out due to its remarkable piezoelectric performance (d_{33} > 350 pC/N) and high Curie temperatures (T_C > 400 °C) near its morphotropic phase boundary (MPB) compositions. However, existing bismuth-based solid solutions come with limitations such as conductivity issues at high temperatures and being confined to a narrow compositional range of 34-36% $BiScO_3$ as the MPB region. Moreover, there is still much to uncover regarding the crystal chemistry and the connection between structure and properties in bismuth-related perovskites. This understanding holds great importance for the future design of high-temperature perovskite materials. Therefore, this work aims to address these challenges, focusing on the development of high-temperature bismuth-based piezo-/ferroelectric materials and understanding the structure-property relationships within bismuth-based perovskites.

The first part (**Chapter 3**) of the thesis is to synthesize and characterize a new bismuth-based relaxor ferroelectric perovskite solid solution of $(1-x)Pb(Sc_{1/2}Nb_{1/2})O_3$-$xBiScO_3$. A systematic study is performed on the solid solution in terms of synthesis, crystal structure analysis, ceramic microstructure imaging, and characterization of physical properties, such as dielectric, ferroelectric, and piezoelectric properties.

The second part (**Chapter 4**) of the thesis focuses on developing a novel ternary solid solution by combining $Pb(Sc_{1/2}Nb_{1/2})O_3$ and $BiScO_3$-$PbTiO_3$ solid solution system. The $BiScO_3$-$PbTiO_3$ solid solution stands out among other developed $BiMeO_3$-$PbTiO_3$ solid solutions due to its exceptional piezoelectric performance (d_{33} > 350 pC/N) and high Curie temperatures (T_C > 400 °C) near its morphotropic phase boundary (MPB) compositions. However, these compositions face challenges such as high conductivity, particularly at elevated temperatures which limit their operational temperature range. $Pb(Sc_{1/2}Nb_{1/2})O_3$ is introduced into the $BiScO_3$-$PbTiO_3$ solid solution to create a novel pseudo-binary solid solution system known as PSN-BS-PT. Different compositions of $xPSN-(1-x)[(BS)_{0.34}(PT)_{0.66}]$, $xPSN-(1-x)[(BS)_{0.35}(PT)_{0.65}]$, and $xPSN-(1-x)[(BS)_{0.36}(PT)_{0.64}]$ are synthesized in the form of ceramics. All the compositions are characterized in terms of crystal structure, ceramic microstructure, dielectric, ferroelectric, and piezoelectric properties.

The final part (**Chapter 5**) of the thesis is to grow single crystals of the new PSN-BS-PT system to further improve its piezo-/ferroelectric performance and to study its domain structure. Bismuth-based single crystals of the $0.1Pb(Sc_{1/2}Nb_{1/2})O_3$-$0.315BiScO_3$-$0.585PbTiO_3$ (0.1PSN-0.315BS-0.585PT) ternary complex perovskite system were successfully grown using the high-temperature solution growth (HTSG) method. The crystals are analyzed for their crystal structure, ferroelectric, and piezoelectric properties. Additionally, domain structures are studied through optical analysis using polarized light microscopy (PLM).

Chapter 2.

Materials Characterizations: Principles and Techniques

2.1. Introduction

In this chapter, the focus is on introducing the methods employed for synthesizing materials (polycrystalline ceramics and single crystals) and outlining the fundamental principles behind the various experimental techniques utilized to analyze the crystal structure and physical properties of the materials investigated in this thesis. The synthesis of polycrystalline ceramics was primarily accomplished using the solid-state reaction method. The single crystals were grown from high temperature solution growth (HTSG) method. The investigation of crystal structures within the fabricated materials involved the utilization of techniques, such as powder X-ray diffraction (XRD), and Rietveld refinements to delve into the characteristics of the ceramics, including morphology and grain sizes in their as-sintered state, the Helium Ion Microscopy (HIM) technique was employed. The comprehensive assessment of physical properties including dielectric, ferroelectric, and piezoelectric properties was conducted through dielectric spectroscopy, along with ferroelectric and piezoelectric measurements.

2.2. Powder X-ray Diffraction (XRD)

X-ray diffraction (XRD) is a widely used and reliable method for studying the structure of crystalline materials. It's based on the idea of constructive interference with X-rays produced by a crystalline sample. To generate X-rays, we typically use X-ray tubes, which have a heated cathode that can release electrons. These electrons are then accelerated by a high electric potential before hitting a target material, called an anode. When this collision occurs, electrons from the K shell of the target atom are knocked out by the electron beam, causing electrons from higher energy levels to move down to fill the gaps. This energy shift results in X-ray radiation.

In particular, transitions from the L shell create K_α lines, and those from the M shell produce K_β lines. The wavelength of this X-ray radiation depends on the material used as the target. In our experiment with the Bruker D8 Advanced Diffractometer, we use copper as the target, which gives us K_α radiation with a wavelength of 1.5418 Å.

As visually depicted in Figure 2.1, when a crystal is subjected to X-ray bombardment at specific incident angles, the generation of intense peaks in diffracted radiation hinges upon the constructive interference of the scattered X-rays. This phenomenon necessitates that the disparity in path lengths be an integral multiple of wavelengths. In simpler terms, for a crystal characterized by a planar lattice spacing denoted as 'd,' the discrepancy in travel path lengths between the ray paths ABC and A'B'C' must amount to an integer count of wavelengths. The general relationship binding the wavelength (λ) of incident X-rays, the angle of incidence (θ), and the spacing (d) between crystal lattice planes is encapsulated within Bragg's Law:

$$2d \sin\theta = n\lambda \qquad (2.1)$$

Where 'n' signifies an integer indicative of the diffraction order. The resultant diffraction pattern typically materializes as a plot of diffracted X-ray intensity against the angle 2θ. Each distinctive peak within this pattern corresponds to a set of planes characterized by an identical inter-planar spacing 'd'.

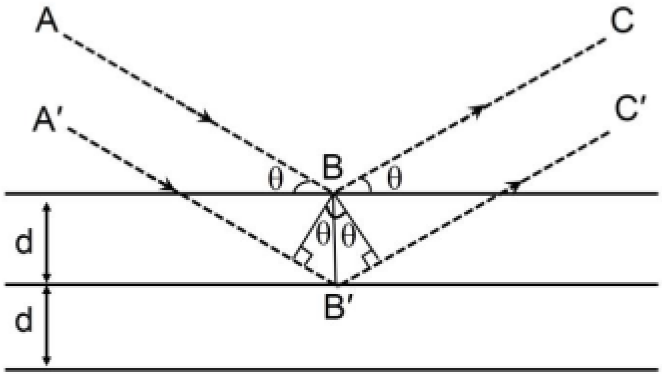

Figure 2.1: Schematic illustration of Bragg's laws derivation from a set of lattice planes with interplanar spacing (d) and the diffraction of X-rays by a crystal.

2.2.1. Principles Employed in Crystal Symmetry Determination

The description of a material's crystal structure centers around its unit cell configuration, as illustrated in Figure 2.2. This unit cell is defined by lattice parameters, encompassing the lengths of its edges (a, b, c) and the respective angles between them (α, β, γ). Seven crystal symmetries exist, determined by the dimensions of the unit cell edges and the angles formed between the x, y, and z axes. The identity of these symmetries, along with their respective edge lengths and angles, is presented in Table 2.1.[38]

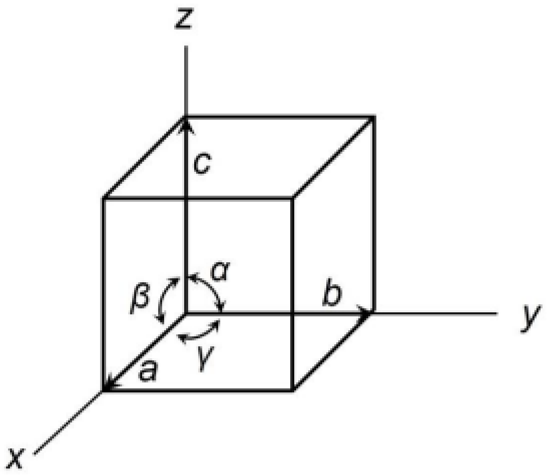

Figure 2.2: **Defining lattice parameters and angles within a crystal unit cell.**

Table 2.1: **Symmetry names, unit cell parameters, and angles for the seven crystal systems.**

Symmetry	Lattice Parameters	Angles
Cubic	$a = b = c$	$\alpha = \beta = \gamma = 90°$
Tetragonal	$a = b \neq c$	$\alpha = \beta = \gamma = 90°$
Orthorhombic	$a \neq b \neq c$	$\alpha = \beta = \gamma = 90°$
Hexagonal	$a = b \neq c$	$\alpha = \beta = 90°, \gamma = 120°$
Rhombohedral	$a = b = c$	$\alpha = \beta = \gamma \neq 90\,°$
Monoclinic	$a \neq b \neq c$	$\alpha = \gamma = 90\,°\,, \beta \neq 90\,°$
Triclinic	$a \neq b \neq c$	$\alpha \neq \gamma \neq \gamma \neq 90\,°$

The relationship between d-spacing and lattice parameters changes depending on the structural type embraced by the material. In the case of materials characterized by crystal structures with orthogonal axes, like cubic, tetragonal, or orthorhombic arrangements, the connection between d-spacing and lattice parameters can be explained with the following equation:

$$\frac{1}{d_{hkl}^2} = \frac{h^2}{a^2} + \frac{k^2}{b^2} + \frac{l^2}{c^2} \qquad (2.2)$$

In this context, 'a,' 'b,' and 'c' represent the unit cell's dimensions, while 'h,' 'k,' and 'l' are labels for specific sets of planes defined by the spacing 'd' between them. To accurately determine the unit cell size, we use a method called indexing the diffraction pattern, matching each observed peak with Miller indices (hkl). For precise results, it's best to label all observed peaks and use regression analysis to calculate the unit cell size. In our research, we use TOPAS academic software to determine crystal symmetry and improve unit cell measurements.

2.2.2. Rietveld Refinement

The refinement of crystal structures was carried out using the Rietveld refinement technique, facilitated by the TOPAS academic software. This method, initially proposed by Hugo Rietveld during the 1960s, involves analyzing neutron or powder X-ray diffraction patterns to gain insights into crystal structure characteristics, including intensity, peak position, and shape. Through a non-linear least squares approach, various parameters, such as background, sample properties, lattice dimensions, atomic arrangements, and symmetry elements, are iteratively adjusted. This process ensures that the calculated profile closely matches the experimental profile, yielding essential information about the crystal structure of the studied materials. Achieving a successful refinement outcome relies on factors like data quality, model accuracy, and the expertise of the researcher.

Central to the Rietveld refinement approach are metrics such as the profile residual factor (R_p), the weighted profile residual (R_{wp}), the expected profile residual (R_{exp}), and the Goodness of Fit (GOF). These measures serve to evaluate the quality of the fitting. These parameters can be computed using the equations presented below:

$$R_p(\%) = \sum_i^n \frac{|Y_i^{obs} - Y_i^{calc}|}{\sum_i^n Y_i^{obs}} \times 100\% \qquad (2.3)$$

$$R_{wp}(\%) = \sum_i^n \frac{w_i(Y_i^{obs} - Y_i^{calc})}{\sum_i^n w_i(Y_i^{obs})^2} \times 100\% \qquad (2.4)$$

$$R_{exp}(\%) = \left(\frac{n-p}{\sum_i^n w_i(Y_i^{obs})^2}\right)^{1/2} \times 100\% \qquad (2.5)$$

$$GOF = \left(\frac{R_{wp}}{R_{exp}}\right)^2 \qquad (2.6)$$

Here, 'n' represents the total data points in the experimental powder diffraction pattern, with 'i' as the index for each point. Y_i^{obs} is the observed intensity at index 'i,' and Y_i^{calc} is the calculated intensity at the same point. We use w_i, often set as 1/ Y_i^{obs}, as the weight for each data point. 'p' represents the number of parameters for the least square fitting.

R_p measures the percentage difference between observed and calculated intensities, while R_{wp} considers the weighted difference. R_{exp} shows the root mean square deviation, and GOF is calculated based on R_{wp} and R_{exp}. Values closer to 1 indicate better fits. However, setting strict thresholds for these parameters is challenging due to factors like peak shapes and background signals that can affect results. The precision of results relies on data accuracy, the fitting model's suitability, and the researcher's expertise. In our study, we determined R_p, R_{wp}, R_{exp}, and GOF through iterative adjustments to achieve the best fit. Typically, reliable results have R_{wp} below 15% and GOF between 1 and 2.

2.3. Dielectric Spectroscopy

Dielectric property measurements play a crucial role in our study, with phase transition temperatures, permittivity values, and dielectric loss being determined. To achieve this, dielectric spectroscopy is employed, a method that allows dielectric permittivity, loss, and phase transitions to be characterized. The dielectric properties of ceramics are examined using a high-resolution Novocontrol Alpha broadband dielectric spectrometer equipped with a specialized high-temperature system. For these measurements, ceramic pellets are carefully prepared, ensuring that flat surfaces are coated with silver paste to create electrodes, effectively forming a sample parallel-plate capacitor. The experimental setup follows the schematic circuit depicted in Figure 2.3, where the samples are connected to the analyzer through gold wires and the Novotherm heating system, enabling precise and controlled characterization of the dielectric properties.

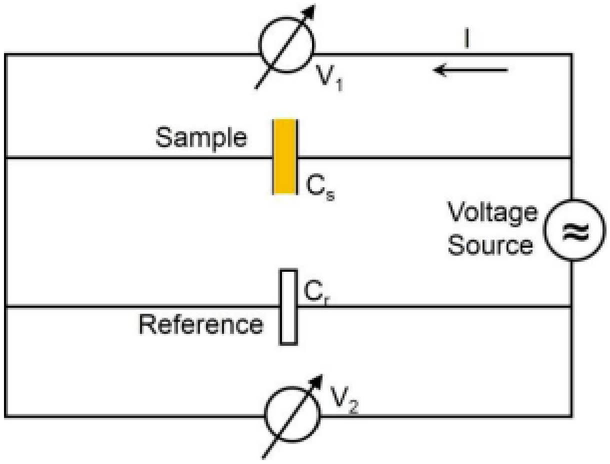

Figure 2.3: Frequency response analyzer circuit for dielectric spectroscopy.

In this arrangement, an applied voltage is sourced from a signal generator across a pair of electrodes situated on the surfaces of both a sample capacitor (C_s, having a thickness denoted as 'd') and a reference capacitor (C_r). Separate voltmeters measure the voltage across the reference capacitor (V_r) and the sample (V_s). Due to the series connection of the two capacitors, the charge on the reference capacitor (Qr) is inherently equivalent to the charge on the sample capacitor (Q_s).

Consequently, the charge on the sample can be determined through:

$$Q = C_r \times V_r \qquad (2.7)$$

Upon obtaining the sample's charge (Q), the material's capacitance can be calculated using the following equation:

$$C = \frac{Q}{V_s} \qquad (2.8)$$

The calculation of the relative real permittivity, denoted as dielectric permittivity ε_r, is carried out using the equation provided below:

$$C = \varepsilon_r \varepsilon_0 \left(\frac{A}{d}\right) \qquad (2.9)$$

Here, C represents the capacitance of the dielectric material situated between two parallel electrodes, ε_0 signifies the permittivity of free space (8.854×10^{-12} F/m), A denotes the surface area of the parallel electrode plates, and d stands for the separation distance between these plates[39].

Dielectric materials typically exhibit energy loss, often attributed to the dissipation of energy through interactions between polarization and electric dipoles. As a result, it becomes essential to account for leakage current when formulating the expression for permittivity. This consideration is underscored by the fact that the charge arising from leakage current varies with time. Consequently, to accurately represent this behavior, dielectric permittivity must be expressed in a complex form that is a function of frequency (f). This complexity is particularly significant as it accounts for both the real and imaginary components of permittivity, reflecting the multifaceted nature of dielectric responses in materials[40].

$$\varepsilon_r^*(f) = \varepsilon'(f) - i\varepsilon''(f) \qquad (2.10)$$

In this context, ε' denotes the real component of dielectric permittivity, often termed as the dielectric constant, and ε'' corresponds to the imaginary component of dielectric permittivity. The loss factor (tan δ) is precisely defined as:

$$\tan\delta = \frac{\varepsilon''}{\varepsilon'} \qquad (2.11)$$

Within this context, δ represents the phase angle between the imaginary and real components of permittivity, as depicted in Figure 2.4. This study entails the assessment of dielectric loss (tan δ) and permittivity (ε') across diverse frequency ranges, while systematically varying temperature conditions.

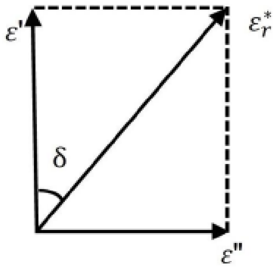

Figure 2.4: Illustration of the loss angle δ in relation to the real and imaginary components of the dielectric permittivity.

2.4. Ferroelectric Hysteresis Measurements

In this study, the ferroelectric characteristics of the prepared ceramics and single crystals were assessed using the RT66A Standard Ferroelectric testing system from Radiant Technologies. This system gauges polarization (P) in relation to electric field (E) across different frequencies, specifically by analyzing P-E hysteresis loops. These loops provide valuable parameters like spontaneous polarization, remnant polarization, and coercive field.

The setup for ferroelectric testing is illustrated in Figure 2.5[7]. It involves a modified Sawyer-Tower electronic circuit employed within the RT66A Standard Ferroelectric testing system. In this arrangement, an AC voltage (V) is administered across the surface electrodes of a sample possessing capacitance (C_s) and thickness (d). The resulting electric field (E) exerted on the sample can be determined using the relevant equation. This configuration allows for precise measurements of hysteresis loops, showcasing the sample's behavior in response to varying electric fields. The circuit compensates for phase shifts originating from conductivity or dielectric loss in the sample, ensuring accurate results.

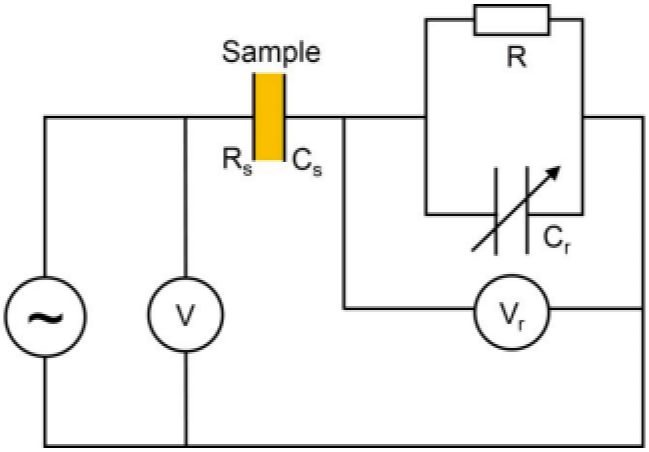

Figure 2.5: Schematic representation of a customized Sawyer-Tower circuit adapted for the precise measurement of ferroelectric hysteresis loops. The symbols C_s, R_s, C_r, R, V, and V_r denote the sample's capacitance, sample resistance, reference capacitance, resistor, step voltage, and voltage across the reference capacitor, respectively.

Spontaneous polarization is the measure of electric charge per unit area on a surface perpendicular to the direction of spontaneous polarization. Since the testing sample and reference capacitor are linked in series, they carry the same amount of charge. Once we determine the charge on the sample, we can calculate the polarization using the following equation:

$$P = \frac{Q}{A} \quad , \qquad (2.12)$$

where Q represents the charge developed on the electrodes of the ferroelectric capacitor, and A denotes the electrode's surface area. In practical experiments, the computer collects digital data, resulting in the creation of a ferroelectric hysteresis loop.[6]

2.5. Piezoelectric Measurements

The determination of the piezoelectric coefficients (d_{33}) for the ceramics under investigation in this thesis was carried out employing a quasi-static measurement technique, utilizing the piezo d_{33}/d_{31} meter (Model ZJ-6B), developed by the Institute of Acoustics at the Chinese Academy of Sciences. This instrument facilitated the precise assessment of the piezoelectric coefficient through quasi-static measurements, revealing the ceramics' responsiveness to mechanical strain and electric polarization.

The expression for the piezoelectric coefficient is given by:

$$d_{33} = \frac{P_3}{T_3}. \qquad (2.13)$$

Here, P_3 represents the charge density (C/m^2), and T_3 corresponds to the applied mechanical stress (N/m^2). The subscript "33" signifies that the measurement of polarization aligns with the direction of the applied stress.

A schematic representation for d_{33} measurement using the Piezo-Meter is depicted in Figure 2.6. Typically, the sample is subjected to a high electric field to ensure the optimal alignment of dipoles within the sample material, a process known as poling.

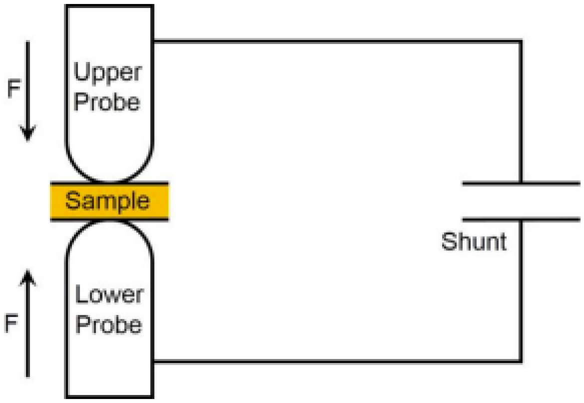

Figure 2.6: Schematic for measuring d_{33} using quasi-static method.

For the measurement of quasi-static d_{33}, meticulous sample preparation was carried out, including the polishing of ceramic or single crystal samples to achieve flat surfaces. Electrodes were formed by applying silver paste to both sides, and reliable ohmic contact was ensured through a 40-minute heat treatment at temperatures ranging from 150 to 200 °C. Subsequently, gold wires were affixed to the electrode surfaces, and the samples were subjected to polarization using direct current (dc) electric fields. These fields were typically maintained at levels equivalent to 1-3 times the coercive fields and lasted for durations up to 1 hour.

An additional step in the poling process involved controlled cooling down to room temperature while maintaining the electric field, thus enhancing polarization alignment. To prevent potential issues like electric sparking and breakdown, the samples were immersed in silicone oil during the poling procedure. Following the poling stage, the gold wires were disengaged, and measurements of quasi-static d_{33} values were carried out on the samples. The resulting average d_{33} values were calculated based on a total of 10 measurements taken from various locations across each ceramic or single crystal and were subsequently reported.

2.6. Helium Ion Microscopy (HIM)

In this thesis, we employ a specialized approach known as Helium Ion Microscopy (HIM) to investigate microstructure of prepared ceramic materials. Helium Ion Microscopy is a high-resolution imaging technique that works by focusing a beam of helium ions onto a sample's surface. These ions interact with the sample's atoms, causing them to scatter and emit various signals. By detecting and analyzing these emitted signals, such as secondary electrons and backscattered helium ions, the microscope creates detailed images of the sample's surface with nanoscale resolution. A schematic of the microscope is shown in Figure 2.7. HIM offers advantages like minimal sample damage and high-resolution imaging, making it useful for various applications in materials science and nanotechnology research. This technique also possesses the advantage of superior depth of field in imaging.

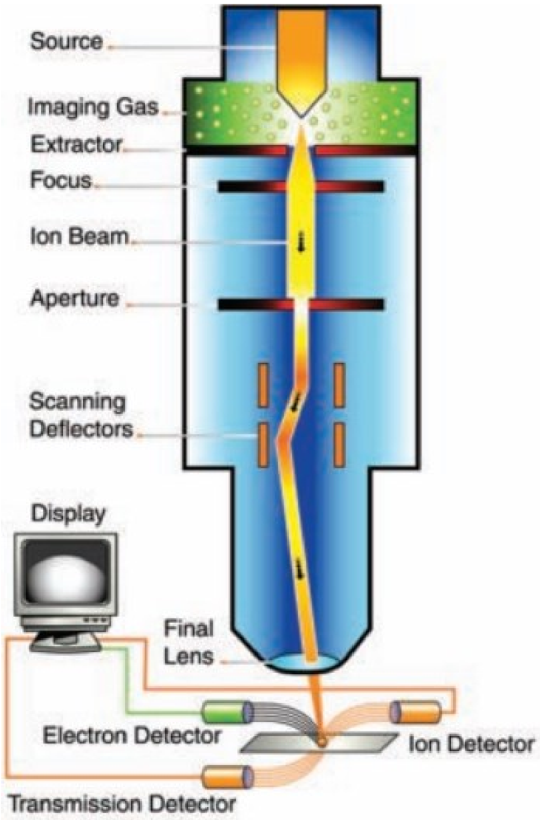

Figure 2.7: Schematic of Helium Ion Microscopy (HIM) imaging system.

For the investigation of ceramic grain size in this work, the software "image J" was employed to quantify the grain sizes within a single HIM image containing 20-50 grains. Each individual grain's size was assessed using four separate measurements in distinct directions, considering the length as the grain size to enhance precision. The accumulated measurements for grain size were subsequently subjected to statistical analysis, yielding insights into grain size distribution and providing information about the average grain size.

2.7. Polarized Light Microscopy (PLM)

In this research, the utilization of Polarized Light Microscopy (PLM) was pivotal, allowing for the determination of crystal symmetry, observation of domain structure, measurement of birefringence, and investigation of phase transitions in single crystals due to their inherent anisotropy. An Olympus BX60 PLM, equipped with a Linkam THMS600 heating/cooling stage and a top-mounted digital camera, was employed. The configuration of PLM, illustrated in Figure 2.8, features a polarizer positioned at the base and an analyzer situated at the top, oriented at a 90° angle to the polarizer to prevent the passage of any light.

Figure 2.8: Principle and configuration of polarized light microscopy (PLM).

Note: reproduced from Ref[74] with qualification for fair dealing for the purpose of research.

In optically isotropic crystals, the entering light remains unchanged, refracted at the same angle and with constant velocity due to uniform refractive indices in all directions. Consequently, full extinction is observed when an isotropic crystal is placed between the polarizer and analyzer in PLM. However, in optically anisotropic crystals, the orientation of crystallographic axes in relation to the incident light angle determines their interaction with light due to varying refractive indices. When an anisotropic crystal is positioned with the incident light along its optical axis, it behaves like isotropic crystals, resulting in extinction. If the light enters from a non-optical axis, it's refracted into two perpendicularly polarized components – extraordinary and ordinary rays. This phenomenon is called birefringence, leading to interference patterns with various colors. Birefringence value (Δn) is calculated using the two refractive indices (n_e and n_o) through the following equation:

$$\Delta n = |n_e - n_0| \qquad (2.14)$$

Due to varying speeds between ordinary and extraordinary rays, one of them lags behind, leading to a calculated retardation (R). When these light components leave the specimen, they go out of phase but then recombine within the analyzer, creating constructive and destructive interference patterns. Measuring this retardation with PLM allows us to determine the crystal's birefringence value. This value is calculated using Equation 2.15, where 'R' stands for retardation, and 't' represents the crystal's thickness.[41]

$$R = t \times \Delta n \qquad (2.15)$$

In this study, we utilized an Olympus U-CBE Berek compensator. This compensator involves a birefringent material like calcite or magnesium fluoride, which is placed perpendicular to the microscope's optical axis between the sample and the analyzer. By adjusting the tilt of this optical plate, we can control its impact on the passing light. When it is not tilted, it has no effect on the transmitted light. However, when tilted, it retards the light in a manner that depends on the tilt angle. To achieve compensation, the compensator crystal is adjusted until no light passes through the analyzer. The angle of rotation, denoted as θ, can be converted into retardation using Equations 2.16 and 2.17:

$$R = C \times \frac{2\left|\sqrt{1-\sin\theta^2/_{\omega^2}} - \sqrt{1-\sin\theta^2/_{\omega^2}}\right|}{\left|1/_{\varepsilon^2} - 1/_{\omega^2}\right|} \qquad (2.16)$$

$$C = \frac{d\times\omega}{2}\left|\frac{1}{\varepsilon^2} - \frac{1}{\omega^2}\right| \qquad (2.17)$$

The birefringence of the crystal sample can be determined using Equation 2.17, with C denoting the compensator's invariables, ω and ε representing the ordinary and extraordinary refractive indices of the compensator, and d indicating the thickness of the compensator. By examining how birefringence changes with temperature, the phase transition occurring at T_C and any additional phase transitions can be analyzed.

Chapter 3.

Synthesis, Structure and Characterization of a New Bismuth-based Relaxor Ferroelectric Perovskite Solid Solution System of (1-x)$Pb(Sc_{1/2}Nb_{1/2})O_3$-x$BiScO_3$

3.1. Abstract

Relaxor ferroelectric materials (RFEs) are an intriguing class of materials due to their unique nanostructure and exceptional properties. These materials are valuable for various technological applications such as ultrasonic transducers, sonar devices, actuators, and frequency filters due to their versatile dielectric and electromechanical properties. Among lead-based oxide perovskite materials, lead scandate-niobate $Pb(Sc_{1/2}Nb_{1/2})O_3$ (PSN) and its solid solutions are relatively less studied compared to its counterparts $Pb(Mg_{1/3}Nb_{2/3})O_3$ (PMN) and $Pb(Zn_{1/3}Nb_{2/3})O_3$ (PZN) relaxor ferroelectrics. In this work, a systematic study is performed on the new bismuth-based solid solution of (1-x)$Pb(Sc_{1/2}Nb_{1/2})O_3$-x$BiScO_3$ in terms of synthesis, crystal structure analysis, ceramic microstructure, and characterizations of physical properties including dielectric, ferroelectric, and piezoelectric properties. X-ray diffraction analysis reveals a rhombohedral phase symmetry (space group R3m) up to a solubility limit of x = 0.20 for the (1-x)$Pb(Sc_{1/2}Nb_{1/2})O_3$-x$BiScO_3$ solid solution. Microstructural analysis shows an increase in average grain size with increasing $BiScO_3$ content, which is attributed to the lower melting point of Bi_2O_3 compared to $Pb(Sc_{1/2}Nb_{1/2})O_3$ and the subsequent grain coarsening during high-temperature sintering. Dielectric measurements indicate a normal ferroelectric phase transition for $Pb(Sc_{1/2}Nb_{1/2})O_3$, while the compositions with x = 0.05, 0.10, 0.15, and 0.20 exhibit a relaxor-like dielectric frequency dispersion, displaying typical relaxor characteristics, with broad and diffuse permittivity peaks which shift to higher temperatures with increasing measurement frequency. Therefore, the substitution of $BiScO_3$ for $Pb(Sc_{1/2}Nb_{1/2})O_3$ induces a crossover from the ferroelectric phase to a relaxor state. The high-temperature slope of the dielectric permittivity of the relaxor compositions can be described with a quadratic equation and the temperature dependences of the dielectric permittivity satisfies the Vogel-Fulcher law. As a representative composition of this solid solution, 0.90$Pb(Sc_{1/2}Nb_{1/2})O_3$-0.10$BiScO_3$

exhibits a high saturation polarization (P_S = 21.45 μC/cm^2), a moderate piezoelectric performance (d_{33} = 32 pC/N), and a low remanent polarization (P_r = 2.62 μC/cm^2) values, characteristic of relaxor ferroelectrics, making it potentially useful for energy storage and electromechanical transduction applications.

3.2. Introduction

Relaxor ferroelectrics (or relaxors, RFEs) and their solid solutions have attracted increasing interest in recent years due to their unique nanostructure and exceptional properties[8,16,42,43]. These materials represent a fascinating class of materials with versatile electrical properties, making them valuable across various technological applications such as ultrasonic transducers, sonar devices, actuators, sensors, electro-optic devices, non-destructive testing equipment, and frequency filters.[10,43,44]

Unlike conventional (or normal) ferroelectrics, where the dielectric permittivity reaches a distinct maximum at the frequency-independent Curie temperature (T_C), relaxors exhibit a different behavior. Their dielectric response is characterized by a broad, frequency-dependent peak in the temperature dependence of permittivity. The key feature of relaxors is their disordered crystal structure, which is often found in complex perovskite materials represented by the formula $[A'_{(1-x)}A''_{x}][B'_{(1-y)}B''_{y}]O_3$ where two or more ions with different valences occupy a crystallographically equivalent position[16]. Within these materials, instead of forming macroscopic polar domains, a local structure known as polar nanoregions (PNRs) emerges due to the chemical and crystallographic disorders resulting from the presence of multiple ionic types in equivalent sites. As the material undergoes cooling, the reorientation (dynamics) of the polar nanoregions (PNRs) gradually slows down, eventually freezing into a random and disordered polar state. This slowing down of PNR dynamics is the key reason why relaxor ferroelectrics exhibit a distinctive feature: a broad and frequency-dependent peak in permittivity.[42]

Lead-based oxide provskite relaxor materials are particularly intriguing, with remarkable dielectric and piezoelectric properties that have gained substantial attention in both fundamental physics and materials and device engineering. In perovskites like $Pb(Mg_{1/3}Nb_{2/3})O_3$ (PMN), which belong to the $Pb(B_{1/3}B'_{2/3})O_3$ type complex perovskites, the B-sites are randomly occupied by both B^{2+} and B'^{5+} ions, driven by the interplay between 1:2 charge and 1:1 strain orders[14,45]. On the other hand, in complex perovskites like $Pb(Sc_{1/2}Nb_{1/2})O_3$ (PSN), falling under the $Pb(B_{1/2}B'_{1/2})O_3$ type, there is no inherent frustration on the B-site which has a 1:1 ratio for the Sc^{3+} (with an ionic radius of 0.745 Å) and Nb^{5+} (with an ionic radius of 0.64 Å) ions. The differences in the charges and ionic radii of these two elements are close to the critical limits for disorder/order occupancy on the B-site in the crystal structure. This means that the arrangement of the B-site cations, i.e. the degree of order/disorder, can be modified by adjusting the thermal treatment during ceramic sintering or the conditions during crystal growth.[46–48] The structure and properties of the prototypical relaxor ferroelectrics PMN and $Pb(Zn_{1/3}Nb_{2/3})O_3$ (PZN) have been extensively studied.[15,45,49] In contrast, $Pb(Sc_{1/2}Nb_{1/2})O_3$ (PSN)-based relaxor ferroelectrics are less well studied.

In order to gain deeper insights into the structure-property relationship of relaxor ferroelectrics, a novel complex solid solution, $(1-x)Pb(Sc_{1/2}Nb_{1/2})O_3-xBiScO_3$ (PSN-BS) is synthesized in the form of ceramic materials through the solid-state reaction method, and its structure and properties are investigated systematically. This comprehensive study involves the analysis of crystal structure, imaging of ceramic microstructure, and the characterization of various physical properties, including dielectric, ferroelectric, and piezoelectric properties. A crossover from the ferroelectric phase in PSN to a relaxor state is induced in the PSN-BS solid solution with the substitution of BS for PSN. A high saturation polarization ($P_S = 21.45$ μC/cm^2), a moderate piezoelectric performance ($d_{33} =$ 32 pC/N), and a low remanent polarization ($P_r = 2.62$ μC/cm^2) values are found for the representative compound of $0.90Pb(Sc_{1/2}Nb_{1/2})O_3-0.10BiScO_3$,. These properties are characteristic of relaxor ferroelectrics, making the solid soolution particularly suitable for applications in dielectric capacitors for energy storage and electromechanical transducers for sensing and actuating.

3.3. Solid State Synthesis and Ceramics Sintering

The solid-state reaction method was utilized for synthesizing the solid solutions of $(1-x)Pb(Sc_{1/2}Nb_{1/2})O_3-xBiScO_3$, with varying compositions represented by x values ranging from 0 to 0.25, in the form of ceramics. High-purity oxide powders, including PbO (99.9% purity, Alfa Aesar), Bi_2O_3 (99.975% purity, Alfa Aesar), Sc_2O_3 (99.5% purity, Alfa Aesar), and Nb_2O_5 (99.9% purity, Alfa Aesar), were employed as the raw materials. An excess of 2 mole% of Bi_2O_3 and PbO was added to compensate for their volatilization at high temperatures. The stoichiometric mixtures of these oxides were hand ground for 2 hours, pressed into pellets, and subjected to calcination at 850 °C for a duration of 6 hours in a muffle furnace. Perovskite solid solutions are formed through the following chemical reaction:

$$(1-x)PbO+\frac{x}{2}Bi_2O_3+\frac{1-x}{4}Sc_2O_3+\frac{1-x}{4}Nb_2O_5 \rightarrow (1-x)Pb\left(Sc_{\frac{1}{2}}Nb_{\frac{1}{2}}\right)O_3+xBiScO_3$$

Following the calcination, the phase purity of the samples was assessed using powder X-ray diffraction (XRD) techniques to check the formation of the phase(s). If the solid solution displayed a pure perovskite phase, the calcined powders were then reground and ball-milled for 24 hours to reduce the particle sizes. After milling, the powder was air-dried and mixed with a small amount of 5 wt% polyvinyl alcohol (PVA) to bind the crystallites together and form small round particles to favor densification of ceramics. The particles were further filtered by passing them through a 120-mesh sieve (0.125 μm) to create denser ceramics. The sieved fine particles were then weighed, with typically 0.6 grams per pellet, and subjected to uniaxial pressing to form 10 mm diameter pellets using a hydraulic press machine under a pressure of 500 MPa.

To minimize the potential evaporation of PbO and Bi_2O_3 at high temperatures, the pressed pellets were placed beside a sacrificial powder having the same composition during the sintering process. The sintering process involved initially heating the pellets to 600 °C and holding them at this temperature for 1 hour to burn out the PVA binder. Subsequently, the temperature was raised to 1100 - 1125°C, and the pellets were held at this temperature for 2 hours to achieve densification of the ceramics. To reduce the risk of ceramics' breaking during cooling, a slower cooling rate was employed. The heating rate during heating was set at 300 °C/h, and the cooling rate was set at 200 °C/h.

3.4. Formation of Solid Solution and Determination of its Solubility Limit

The formation of phases and the limit of the solubility of $BiScO_3$ in $Pb(Sc_{1/2}Nb_{1/2})O_3$ are investigated by powder X-ray diffraction (XRD) using Rigaku MiniFlex 6G system. Figure 3.1 illustrates the XRD patterns for $(1-x)Pb(Sc_{1/2}Nb_{1/2})O_3$-$xBiScO_3$ with nominal compositions of x = 0.05, 0.10, 0.15, 0.18, 0.20, 0.21, and 0.25

following the calcination process. The XRD patterns of the compositions with $x \leq 0.20$ show a pure perovskite phase characteristic of pure $Pb(Sc_{1/2}Nb_{1/2})O_3$ (PDF #80922), indicating the successful formation of the $(1-x)Pb(Sc_{1/2}Nb_{1/2})O_3$-$xBiScO_3$ solid solutions. However, for the compositions of x = 0.21, 0.23, and 0.25, although the primary peaks closely match the characteristic peaks of the perovskite phase, impurity peaks become evident. These impurity peaks are identified to belong to the $Pb_2(ScNb)O_7$ pyrochlore phase using the Jade software. Attempts were made to eliminate these impurity peaks by varying the calcination temperature range from 850 °C down to 750 °C in 50 °C intervals and adjusting the calcination time from 6 hours to 10 hours in 2-hour intervals. Unfortunately, these efforts could not eliminate the impurity peaks. Therefore, it is concluded that the solubility limit for the $(1-x)Pb(Sc_{1/2}Nb_{1/2})O_3$-$xBiScO_3$ perovskite solid solution is x = 0.20.

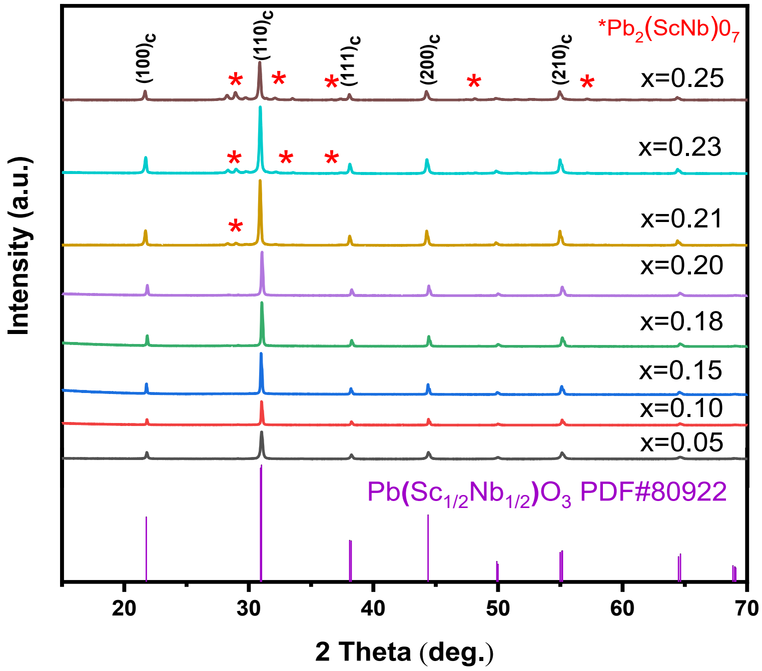

Figure 3.1: **Powder X-Ray diffraction (XRD) patterns of $(1-x)Pb(Sc_{1/2}Nb_{1/2})O_3$-$xBiScO_3$ after calcination measured at room temperature, with the reference pattern of pure $Pb(Sc_{1/2}Nb_{1/2})O_3$ (PDF # 80922) displayed.**

3.5. Crystal Structure Analysis

The room temperature powder XRD patterns for the $(1-x)Pb(Sc_{1/2}Nb_{1/2})O_3$-$xBiScO_3$ solid solution ceramics (with $x \leq 0.20$) after sintering are presented in

Figure 3.2. The agreement between the reference pattern (PDF #80922) and the measured patterns confirms that all the compounds crystallized in the perovskite structure. Notably, the $(200)_c$ single peak, and the splitting observed in the $(111)_c$ indicate that $(1\text{-}x)Pb(Sc_{1/2}Nb_{1/2})O_3\text{-}xBiScO_3$ solid solution maintains a rhombohedral symmetry with the R3m space group for all compositions within the solubility limit. This finding aligns with the existing literature on $Pb(Sc_{1/2}Nb_{1/2})O_3$.[50]

To further analyze the crystal structure, Rietveld refinements were performed on high-quality data collected from Bruker D8 Advance X-ray diffractometer. The confirmation of the rhombohedral symmetry is supported by the good fitting results of the Rietveld refinements, as shown in Figure 3.3 and Table 3.1. The resulting values of lattice parameters 'a_R' and 'α_R', and unit cell volume 'V_R' are detailed in Table 3.1. The variations in these parameters as a function of $BiScO_3$ mole content are graphically presented in Figure 3.4.

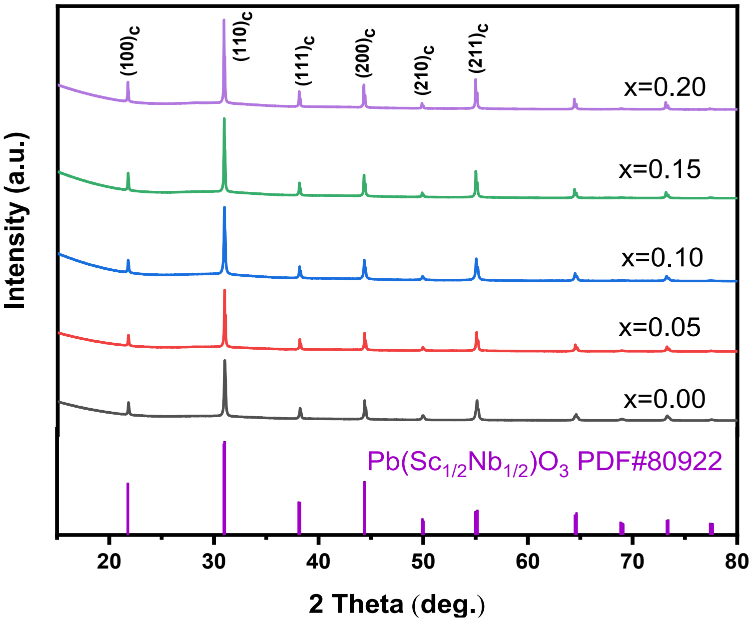

Figure 3.2: **Room temperature X-ray diffraction (XRD) patterns of the $(1\text{-}x)Pb(Sc_{1/2}Nb_{1/2})O_3\text{-}xBiScO_3$ solid solution ceramics after sintering, with the reference pattern for pure $Pb(Sc_{1/2}Nb_{1/2})O_3$ (PDF # 80922) shown for comparison.**

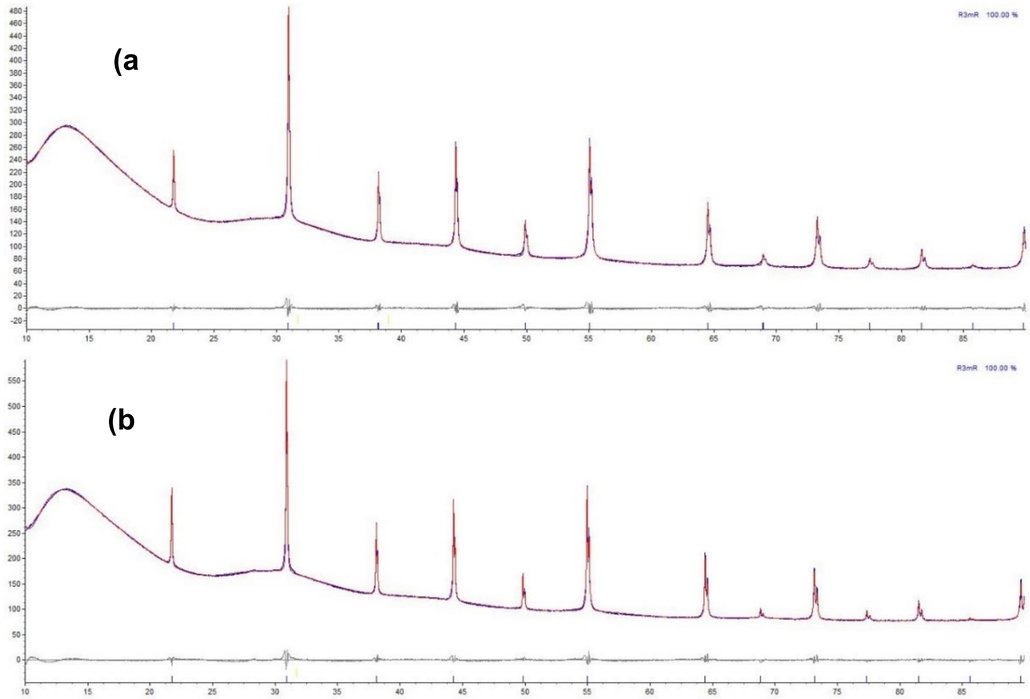

Figure 3.3: Results of Rietveld refinement fitting of the high-resolution X-ray diffraction data of the (1-x)Pb($Sc_{1/2}Nb_{1/2}$)O_3-xBiScO$_3$ solid solution: (a) x = 0, (b) x = 0.10.

As presented in Figure 3.4, the lattice parameters 'a_R' and 'α_R' of the rhombohedral solid solution (1-x)Pb($Sc_{1/2}Nb_{1/2}$)O_3-xBiScO$_3$ exhibit an increasing trend as the content of BiScO$_3$ increases. Consequently, the unit cell volume of the solid solution shows a consistent increase, as documented in Table 3.1. These general trends of expanding lattice parameters and unit cell volume can be attributed to the fact that Sc^{3+} ions (with an ionic radius of r = 0.745 Å) are larger in size compared to Nb^{5+} ions (with an ionic radius of r = 0.64 Å) when they occupy the B-site (coordination number = 6) within the perovskite structure. This effect is predominant over the fact that the ionic radius of Bi^{3+} (r = 1.44 Å) is slightly smaller in comparison to Pb^{2+} (r = 1.49 Å) when they occupy the A-site (coordination number = 12).

Table 3.1: Phase and variations of the 'a_R' and 'α_R' lattice parameters, and volume of the unit cell (V_R) as a function of BiScO$_3$ content for the (1-x)Pb($Sc_{1/2}Nb_{1/2}$)O_3-xBiScO$_3$ solid solutions.

x	Phase	a_R (Å)	α_R (°)	V_R (Å^3)	R_{wp}, R_{exp}, and R_p (%)

0	R3m (100%)	4.08296±0.00007	89.91060±0.00177	68.06499±0.00366	2.921, 0.752, 1.618
0.05	R3m (100%)	4.08363±0.00012	89.99650±0.01993	68.09875±0.00614	2.512, 0.753, 1.539
0.10	R3m (100%)	4.08486±0.00017	89.99869±0.01337	68.16040±0.00843	2.752, 0.619, 1.553
0.15	R3m (100%)	4.08768±0.00010	89.99918±0.03249	68.30157±0.00493	2.300, 0.632, 1.457
0.20	R3m (100%)	4.08794±0.00009	89.99966±0.01489	68.31460±0.00443	2.615, 0.646, 1.727

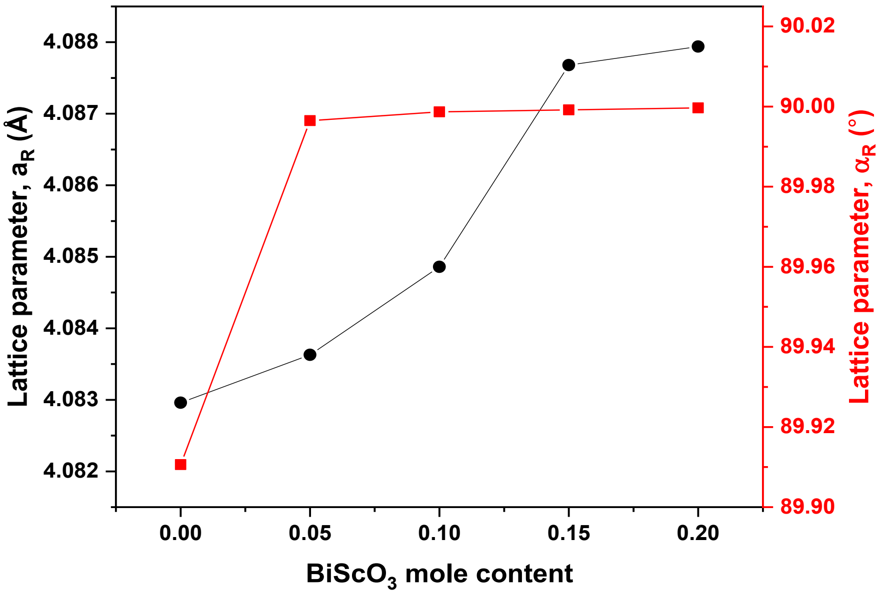

Figure 3.4: **Variations of the room-temperature 'a_R' and 'α_R' lattice parameters, as a function of $BiScO_3$ content for the (1-x)$Pb(Sc_{1/2}Nb_{1/2})O_3$-x$BiScO_3$ solid solution.**

3.6. Ceramic Microstructure Analysis

High-quality ceramics of the (1-x)$Pb(Sc_{1/2}Nb_{1/2})O_3$-x$BiScO_3$ solid solution were successfully synthesized following the sintering process. Helium ion microscopy (HIM, Zeiss Orion NanoFAB equipment) was employed for the examination of the ceramic microstructure. The HIM images presented in Figure 3.5 show that the PSN-BS ceramics contain grains with polygonal shapes. There are either very few or no visible pores and gaps between the grains. These observations indicate a dense microstructure and high-quality for the ceramics. The measured values for apparent density, theoretical density, and relative density are documented in Table 3.2. The high values of relative densities further validate the microstructural imaging result that the synthesized ceramics are of dense microstructure. The grain size distribution and average grain sizes of the ceramics were determined from the HIM images using Image J software. Figure 3.5 demonstrate a substantial increase in average grain size as the mole content of $BiScO_3$ is increased up to 20%. This observed trend indicates a direct relationship between the $BiScO_3$ content and grain growth. This effect could be attributed to the lower melting point of Bi_2O_3 (T_m = 824 °C) compared to $Pb(Sc_{1/2}Nb_{1/2})O_3$ (T_m = 1425 °C), which leads to the formation of a liquid phase at elevated sintering temperatures, enabling enhanced mass transport and substantial grain coarsening.[51,52]

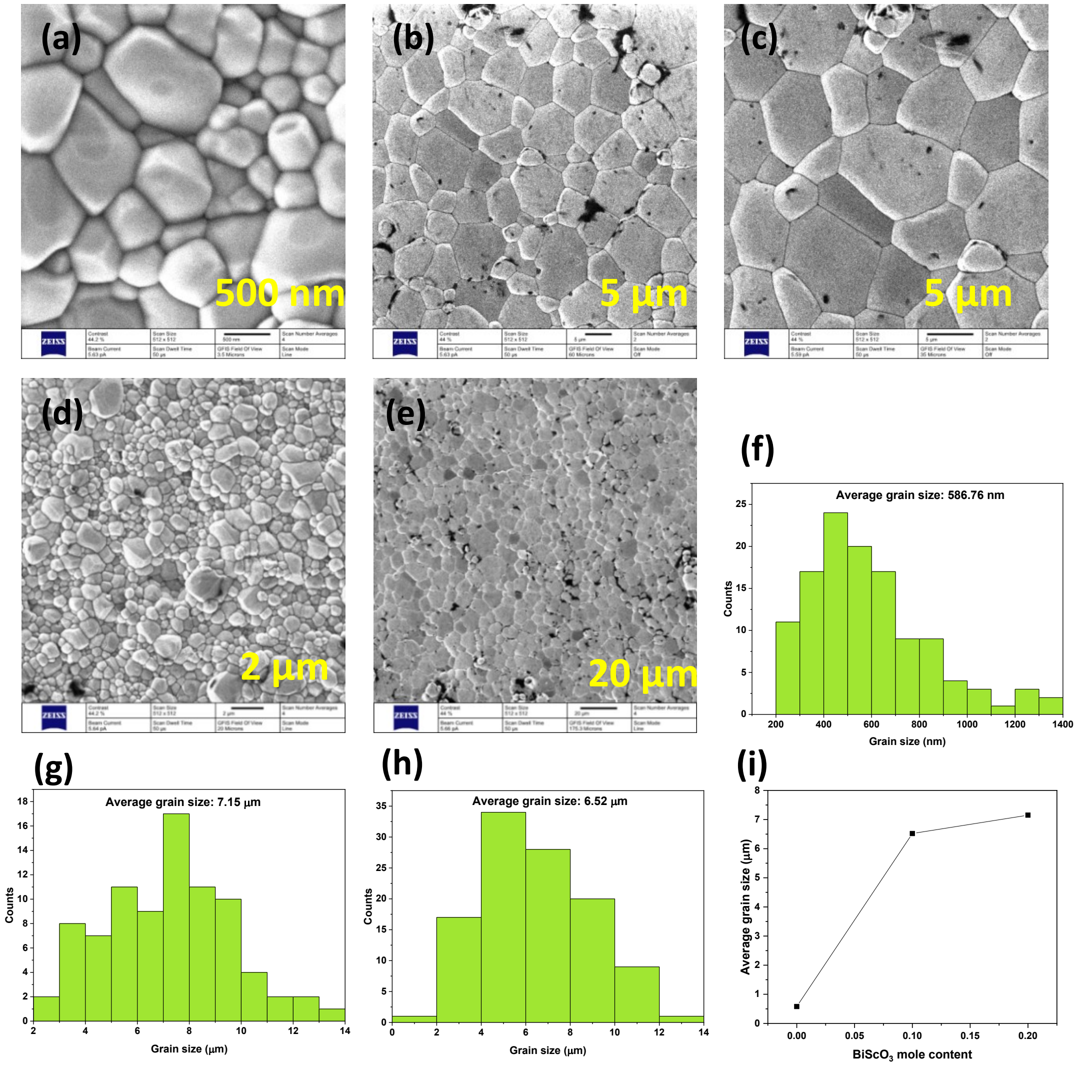

Figure 3.5: Helium ion microscopy (HIM) images of the sintered (1-x)Pb(Sc$_{1/2}$Nb$_{1/2}$)O$_3$-xBiScO$_3$ solid solution ceramics with various compositions: (a) x = 0 with 500 nm scale, (b) x = 0.10 with 5 µm scale, and (c) x = 0.20 with 5 µm scale, (d) x = 0.10 with 2µm scale, and (e) x = 0.20 with 20µm scale. Grain size distribution and average grain sizes of the ceramics calculated using Image J software: (f) x = 0.00, (g) x = 0.10, (h) x = 0.20. Variation of the average grain size with BiScO$_3$ mole content.

Table 3.2: Comparison of the apparent density, theoretical density, and relative density of the (1-x)Pb(Sc$_{1/2}$Nb$_{1/2}$)O$_3$-xBiScO$_3$ solid solution ceramics.

x	Apparent density (g/cm^3)	Theoretical density (g/cm^3)	Relative density
0	7.51	7.90	0.94
0.05	7.45	7.87	0.94
0.10	7.37	7.84	0.93

0.15	7.24	7.79	0.92
0.20	7.25	7.77	0.93

3.7. Dielectric Properties and Relaxation

Figure 3.6 illustrates the temperature-dependent variations of the dielectric constant (ε') and the dielectric loss tangent (tanδ) for all compositions of the (1-x)$Pb(Sc_{1/2}Nb_{1/2})O_3$-x$BiScO_3$ solid solution ceramics measured at different frequencies, using a Novocontrol Alpha high resolution broadband dielectric analyzer with a Novotherm heating system.

The peaks observed in the temperature-dependent behavior of the dielectric constant signify the ferroelectric to paraelectric phase transition occurring at the Curie temperature T_C, or the maximum temperature, T_{max}. The values of T_C or T_{max} for all compositions, measured during both heating and cooling, are presented in Table 3.3 and depicted in Figure 3.7. It is worth noting that the different T_C or T_{max} values obtained during heating and cooling indicate a first-order phase transition due to thermal hysteresis.[4]

Figure 3.6 (a) depicts that the temperature of the peak in the dielectric response of $Pb(Sc_{1/2}Nb_{1/2})O_3$ remains constant at various frequencies. This behavior implies the nature of a normal ferroelectric phase transition in $Pb(Sc_{1/2}Nb_{1/2})O_3$. The normal ferroelectric behavior has been observed for $Pb(Sc_{1/2}Nb_{1/2})O_3$ when lead vacancies therein were effectively minimized or eliminated following a carefully designed production process.[48,50] Therefore, the optimized synthesis process used in this work has led to the formation of stoichiometric PSN with minimized lead vacancies and conventional ferroelectric properties.

As Figure 3.6 (b-e) demonstrate, the peak of the dielectric constant versus temperature shifts to higher temperatures and its magnitude decreases as the measurement frequency increases for the compositions with x = 0.05, 0.10, 0.15 and 0.20. These observations illustrate a "relaxor-like" dielectric frequency dispersion behavior.[8,16,53] Also, the temperature peaks exhibit a diffuse and frequency-dependent permittivity maximum for the compositions with x = 0.05, 0.10, 0.15 and 0.20, suggesting the occurrence of relaxor ferroelectric behavior rather than a typical ferroelectric phase transition in the (1-x)$Pb(Sc_{1/2}Nb_{1/2})O_3$-x$BiScO_3$ solid solutions containing higher than 5 mole% of $BiScO_3$. Thus, the substitution of $BiScO_3$ for PSN induces a crossover from the normal ferroelectric phase to relaxor ferroelectric state, which could be attributed to the enhanced chemical disorder, charge imbalance and inhomogeneous lattice strain created by the $BiScO_3$ substitution.[54]

Furthermore, increasing the $BiScO_3$ content results in wider and more diffuse dielectric profiles, as shown in Figure 3.6 (f), signifying an expansion in the full width at half maximum (FWHM), as detailed in Table 3.3. This implies a higher level of structural disorder and an enhancement in relaxor behavior.[46,55,56]

The addition of $BiScO_3$ in the (1-x)$Pb(Sc_{1/2}Nb_{1/2})O_3$-x$BiScO_3$ solid solution has a significant impact on ΔT_{max} values, which represent the temperature difference between the maximum values observed at frequencies of 1 kHz and 100 kHz. This impact is depicted in Figure 3.7 and detailed in Table 3.3. ΔT_{max} increases with the $BiScO_3$ content increased up to 10%, indicating an increased frequency-dependent behavior and enhanced relxation associated with these materials. At 15% $BiScO_3$ content, a slight decrease in ΔT_{max} is observed, while beyond this point, ΔT_{max} increases once more. This trend reflects the complex interactions among constituents and structural features, and underscores the relaxor ferroelectric characteristics induced by $BiScO_3$.

Figure 3.6 (f) shows the variations of the dielectric constant ε' as a function of temperature for all the compositions of the (1-x)$Pb(Sc_{1/2}Nb_{1/2})O_3$-x$BiScO_3$ solid solution, measured at f = 100 kHz. In comparison, as the content of $BiScO_3$ increases, the dielectric peak became more broadened and flattened, with a continued decrease in the maximum dielectric constant, except for x =0.15, where we notice a slight increase before subsequent decrease. This decrease in the dielectric constant aligns with observations from previous studies.[46,55]

When compared to pure $Pb(Sc_{1/2}Nb_{1/2})O_3$ ceramic, which exhibits a Curie temperature (T_C) of 101°C upon cooling and 99 °C upon heating as determined in this study (97°C upon heating according to Perrin et al. [57]), the (1-x)$Pb(Sc_{1/2}Nb_{1/2})O_3$-x$BiScO_3$ solid solution shows a decrease in the T_{max} values as the content of $BiScO_3$ is increased up to 10%. However, there is a slight increase in T_{max} as the $BiScO_3$ content is further increased to 20%. This non-monotonic trend in maximum temperature (T_{max}) is different from the decreasing T_C trend found in some systems like $Bi(Mg_{2/3}Nb_{1/3})O_3$-$PbTiO_3$ and $Bi(Mg_{3/4}W_{1/4})O_3$-$PbTiO_3$[58]. It also differs from the increasing T_C trend observed in other Bi-based perovskite solid solutions, such as $Bi(Zn_{1/2}Ti_{1/2})O_3$-$PbTiO_3$ and $BiFeO_3$-$PbTiO_3$.[59–61]

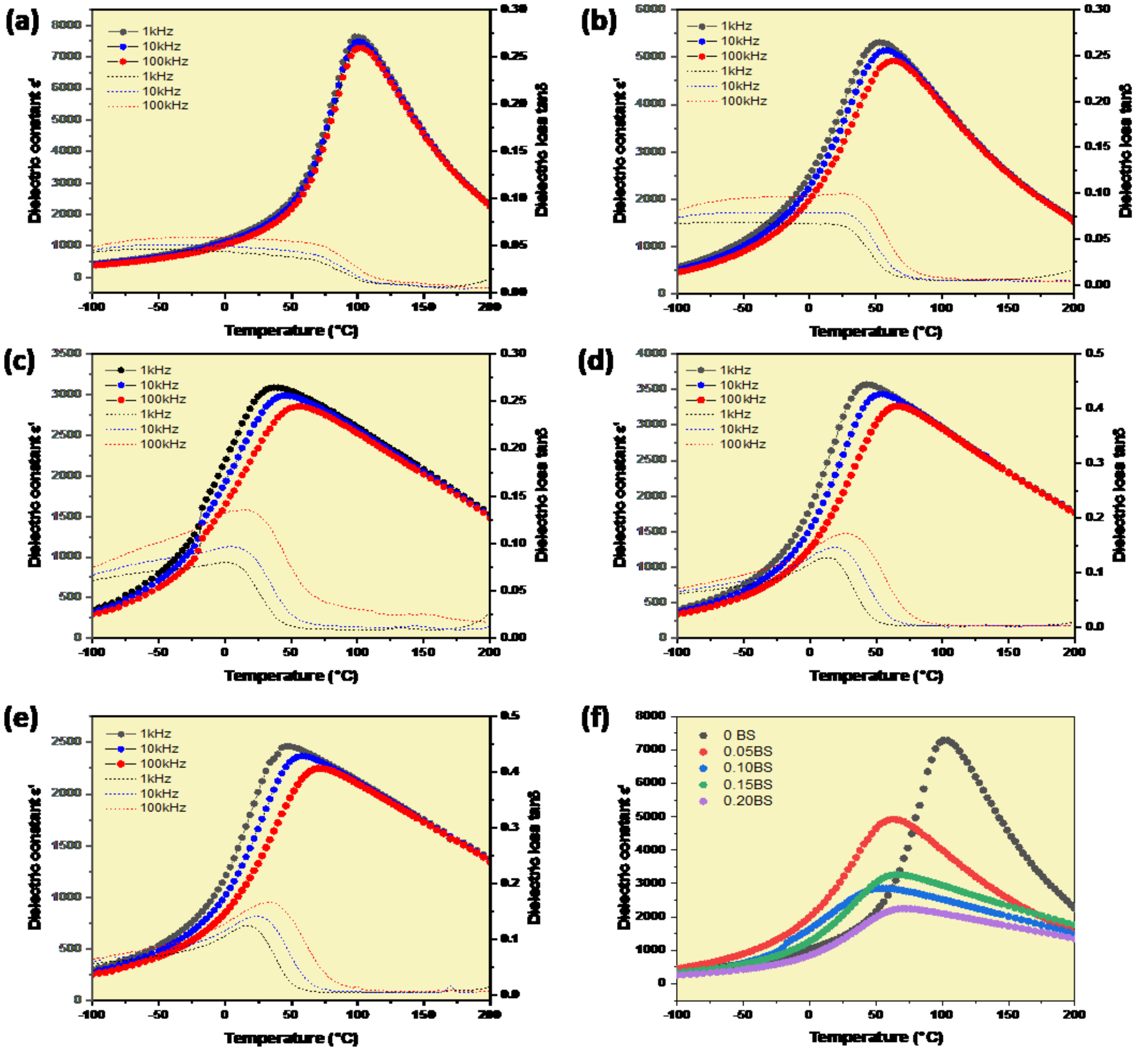

Figure 3.6: **Variation of dielectric constant ε' and loss tangent tan δ as a function of temperature for the (1-x)$Pb(Sc_{1/2}Nb_{1/2})O_3$-x$BiScO_3$ solid solutions: (a) x = 0.00, (b) x = 0.05, (c) x = 0.10, (d) x = 0.15 and (e) x = 0.20, measured at the frequencies of 1 kHz, 10 kHz, and 100 kHz upon cooling. Variations of the dielectric constant ε' as a function of temperature of all the compositions measured at f = 100 kHz (f).**

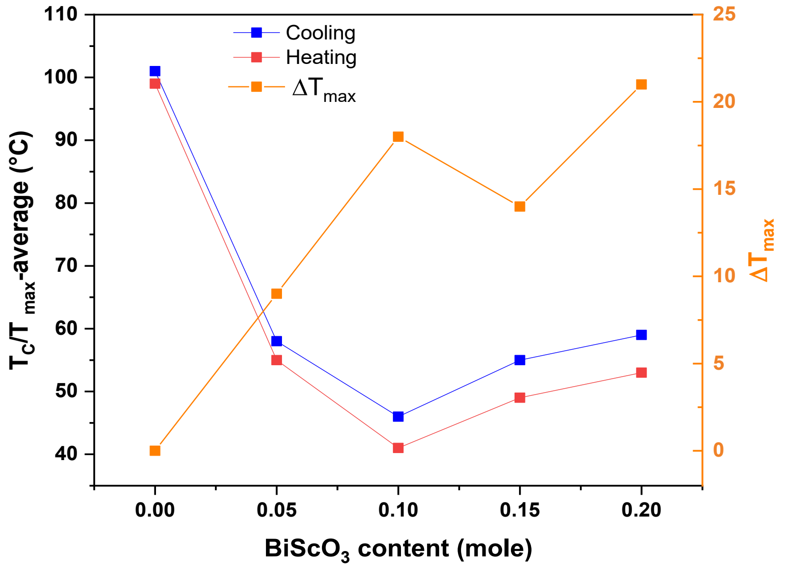

Figure 3.7: Variations of the Curie/maximum temperatures (T_C/T_{max}) as a function of $BiScO_3$ mole content in the $(1\text{-}x)Pb(Sc_{1/2}Nb_{1/2})O_3\text{-}xBiScO_3$ solid solution measured upon heating and cooling, and variations of the ΔT_{max} as a function of $BiScO_3$ mole content upon cooling.

Table 3.3: FWHMs of the dielectric peaks calculated for f = 100 kHz; $T_{C/}T_{max}$ obtained from dielectric measurements upon heating and cooling; ΔT_{max} values obtained from dielectric measurements upon cooling. Errors were determined by the step size of the dielectric temperature measurements.

x	FWHM (°C)	$T_{C/max}$ for heating (°C)	$T_{C/max}$ for cooling (°C)	ΔT_{max} (°C)
0	99.61±2.35	99±3	101±3	0
0.05	138.24±4.10	55±3	58±3	9
0.10	208.64±11.49	41±3	46±3	18
0.15	174.31±7.48	49±2	55±2	14
0.20	179.34±7.05	53±2	59±2	21

Figure 3.8 shows the temperature dependences of the dielectric constant (ε') and loss tangent (tanδ) for the $0.85Pb(Sc_{1/2}Nb_{1/2})O_3\text{-}0.15BiScO_3$ ceramic measured at various frequencies upon cooling. In the temperature ranges shown in Figure 3.8 (a) and Figure 3.8 (b), a pronounced frequency dispersion is observed for the real and imaginary dielectric permittivities, ε' and ε'', as well as the dielectric loss tangent (tan*δ*). When plotted against frequency, as shown in Figure 3.8 (c), ε' gradually decrease with

increasing frequency. As the temperature rises, the frequency dispersion of ε' decreases, showing a nearly frequency-independent behaviour.

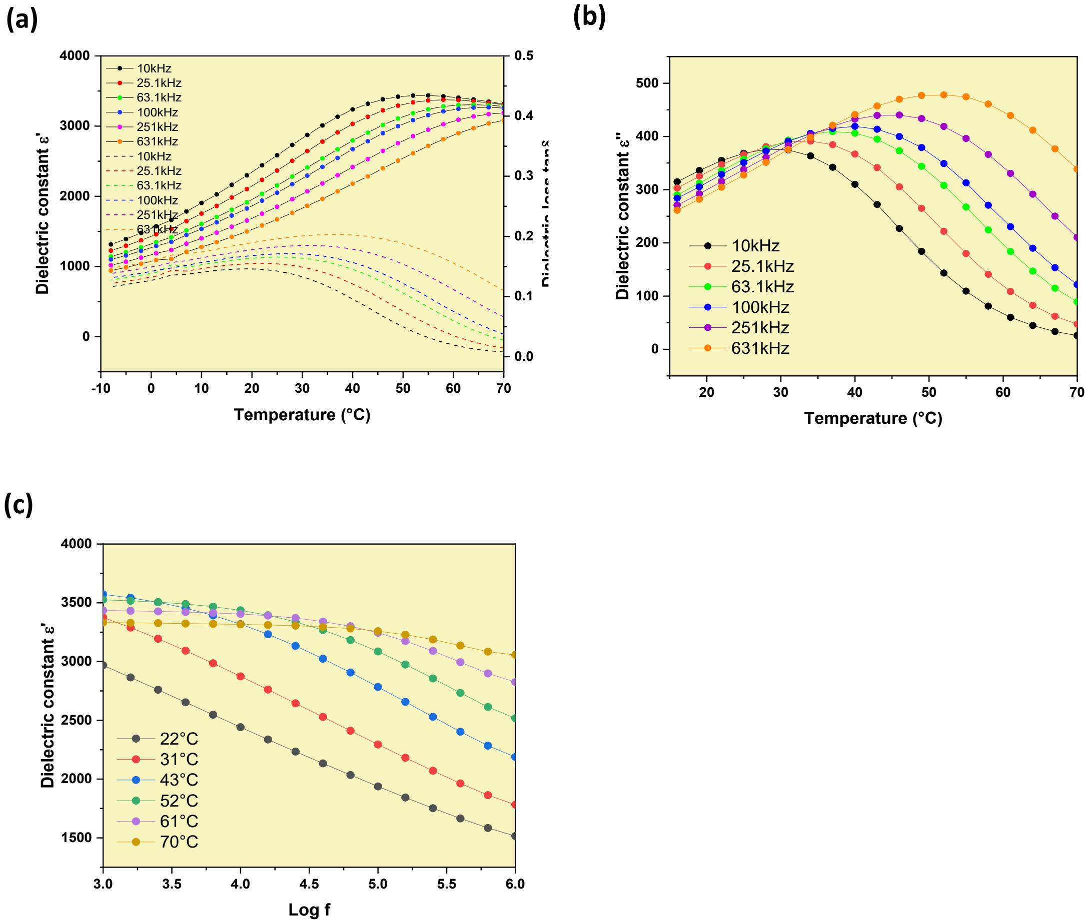

Figure 3.8: **(a) Temperature dependences of the dielectric constant (ε') and loss tangent (tanδ) for (1-x)Pb($Sc_{1/2}Nb_{1/2}$)O_3-xBiScO_3 with x = 0.15 measured at various frequencies upon cooling; (b) Temperature dependences of the imaginary part of the dielectric permittivity (ε'') in the temperature range of 20-70ºC; (c) Frequency dependence of the real part (ε') of the dielectric permittivity for (1-x)Pb($Sc_{1/2}Nb_{1/2}$)O_3-xBiScO_3 with x = 0.15 measured at various temperatures.**

3.8. Relaxor Ferroelectric Properties

As mentioned before, the dielectric permittivity of the (1-x)Pb($Sc_{1/2}Nb_{1/2}$)O_3-xBiScO_3 solid solution exhibits characteristic features of relaxor ferroelectric materials in terms of frequency dependences. This section provides detailed examination of this intriguing relaxor behavior to enhance our comprehension of its properties.

The behavior of the permittivity above T_{max}, observed in $Pb(Mg_{1/3}Nb_{2/3})O_3$ and many other relaxor materials, has been effectively described through a unified model employing a single shape parameter denoted as 'δ'. This parameter is employed within a quadratic law:

$$\frac{\varepsilon_A}{\varepsilon'} = 1 + \frac{(T - T_A)^2}{2d^2} \qquad (3.1)$$

where T_A ($< T_{max}$) represents the peak location and ε_A represents the extrapolated permittivity value at $T = T_A$.[15,43,46] The d parameter serves as a convenient metric for characterizing the extent of broadening in the permittivity peak within relaxor materials. It is noteworthy that this law has demonstrated applicability to a wide range of relaxor materials, irrespective of variations in the degree of peak broadening.[16,43,55]

The slope of the permittivity peak at high temperatures for the $(1-x)Pb(Sc_{1/2}Nb_{1/2})O_3$-$xBiScO_3$ ceramics with compositions of x = 0.10 and x = 0.15 can be described using Equation 3.1. Figure 3.9 illustrates the results of fitting the dielectric permittivity as a function of temperature to the quadratic equation presented in Equation 3.1. This fitting was accomplished by employing a least squares method. The results of this fitting process are very satisfactory for both ceramics, yielding values of d = 91.52 K for x = 0.10, and d = 71.72 K for x = 0.15. The parameter d serves as an indicator of the width of the permittivity peaks and is employed to gauge the extent of diffuseness within these peaks.[46,62] A smaller d parameter implies that the ceramics with x = 0.15 exhibit a sharper permittivity peak.

The observed deviation at lower temperatures can be attributed to the nature of Equation 3.1, which is designed to characterize the static, zero-frequency component of relaxor polarization. In this case, high-frequency data (f = 1 MHz) were utilized for fitting purposes to eliminate any potential influence from relaxation processes associated with grain boundary effects.[42,55,62]

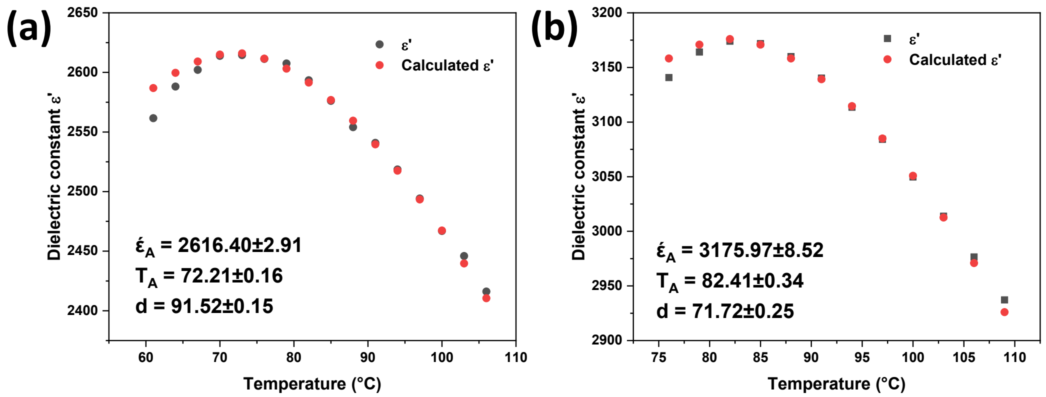

Figure 3.9: Fitting of the dielectric constant as a function of temperature measured at 1 MHz to the quadratic law described in Equation 3.1 for the (1-x)Pb($Sc_{1/2}Nb_{1/2}$)O_3-xBiScO_3 ceramics: (a) x = 0.10, and (b) x = 0.15.

Moreover, the frequency-dependent behavior of the temperature at which the maximum permittivity occurs, denoted as T_{max}, adheres to the Vogel-Fulcher law commonly observed in relaxor materials:

$$\omega = \omega_0 exp\left[\frac{E_a}{(T_{max}-T_f)}\right] \qquad (3.2)$$

In this equation, E_a represents the activation energy, ω_o is the Debye frequency, and T_f is the freezing temperature which signifies the temperature at which the polar nanoregions (PNRs) contributing to the relaxor polarization become immobilized or their dynamics freezes.[42,45,55]

Figure 3.10 displays the fitting outcomes for the T_{max} of the (1-x)Pb($Sc_{1/2}Nb_{1/2}$)O_3-xBiScO_3 ceramics with x = 0.10 and x = 0.15 using the Vogel-Fulcher Equation 3.2. The fitting procedure results in a freezing temperature of -24.97 °C and an activation energy of 0.11 eV for the composition of 0.90Pb($Sc_{1/2}Nb_{1/2}$)O_3-0.10BiScO_3. For the composition of 0.85Pb($Sc_{1/2}Nb_{1/2}$)O_3-0.15BiScO_3, the T_f and E_a values are -48.82°C and 0.18eV, respectively. In the literature, Pb($Sc_{1/2}Nb_{1/2}$)O_3 ceramics were found to have an activation energy of approximately 0.01eV and a freezing temperature of 376 K (103 ℃)[63]. The freezing temperature determined by the Vogel-Fulcher fitting indicates a critical slowing down of polar nanoregion (PNR) dynamics in relaxor materials.[45]

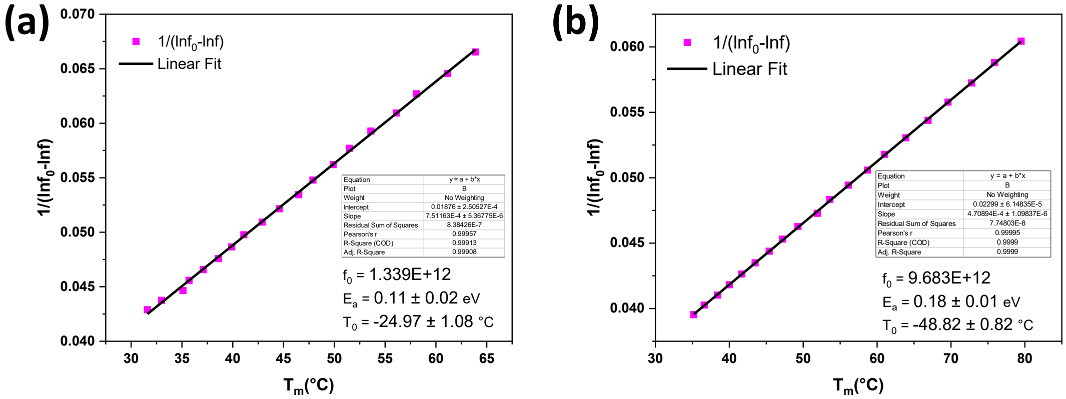

Figure 3.10: Fitting of the dielecric relaxation of the (1-x)Pb($Sc_{1/2}Nb_{1/2}$)O_3-xBiScO$_3$ ceramics to the Vogel-Fulcher law: (a) x = 0.10, and (b) x = 0.15.

3.9. Ferroelectric and Piezoelectric Properties

In Figure 3.11, the polarization-electric field (P-E) hysteresis loops of the (1-x)Pb($Sc_{1/2}Nb_{1/2}$)O_3-xBiScO$_3$ solid solution are depicted. These measurements were conducted at a frequency of 10 Hz and under standard room temperature condition using a Radiant RT66A standard ferroelectric testing system.

The distinctive hysteresis patterns observed in the P-E loops presented in Figure 3.11 affirm the ferroelectric behavior of the the (1-x)Pb($Sc_{1/2}Nb_{1/2}$)O_3-xBiScO$_3$ solid solutions with x = 0.0 and x = 0.05. Notably, as the content of BiScO$_3$ increases up to x = 0.20, there is a noticeable trend of the loops becoming narrower, which is a feature of relaxor ferroelectric materials[55]. The remanent polarization values substantially decrease from 21.43 μC/cm^2 in x = 0 to 0.77 μC/cm^2 in x = 0.20. The lower values of remanent polarization can be beneficial in applications where energy efficiency, stability, and reduced sensitivity to temperature and cost-effectiveness are more important than achieving the highest possible polarization levels.[55,56,64]

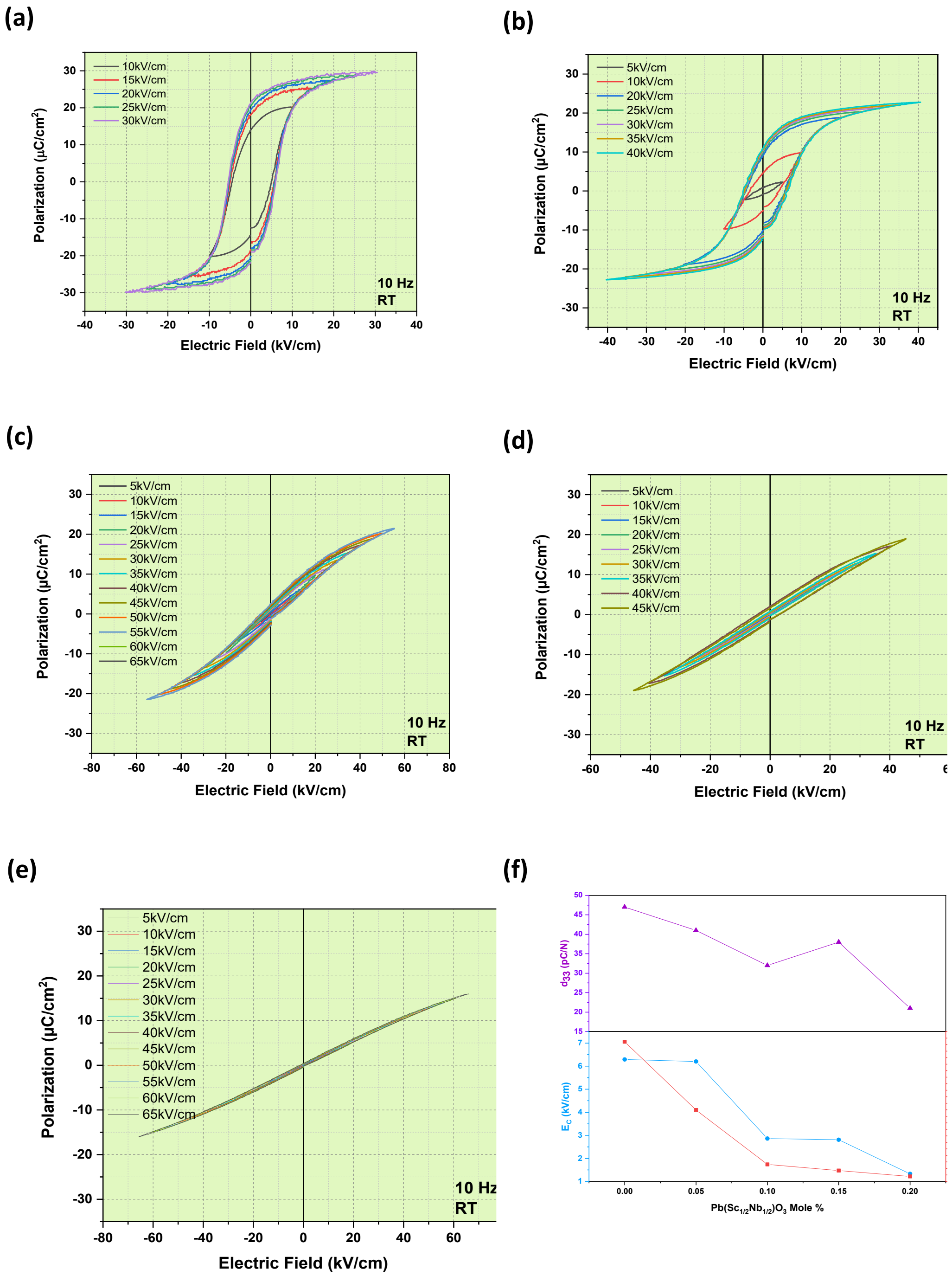

Figure 3.11: Polarization-Electric field (P-E) hysteresis loops of $(1\text{-}x)Pb(Sc_{1/2}Nb_{1/2})O_3\text{-}xBiScO_3$ ceramics at 10 Hz, recorded at room temperature: (a) x = 0.0, (b) x = 0.05, (c)x = 0.10, (d) x = 0.15, and (e) x = 0.20; and (f) variation of the coercive field (E_C), remanent polarization (P_r) and piezoelectric coefficient (d_{33}) as a function of $BiScO_3$ mole content.

Sintered pellets were electroded by a silver paste, then polarized under an electric field of about 30 kV/cm for 60 min in a silicone bath at 40 °C. After that, the samples were allowed to cool down to room temperature with the field kept on for piezoelectric measurements using a piezo d_{33}/d_{31} meter (Model ZJ-6B). Table 3.4 shows a summary of the ferroelectric and piezoelectric properties for the different compositions.

Table 3.4: Ferroelectric and piezoelectric properties of the $(1-x)Pb(Sc_{1/2}Nb_{1/2})O_3$-$xBiScO_3$ solid solutions measured at room temperature: E_C = Coercive Field, P_S = Saturation Polarization, P_r = Remanent Polarization, d_{33} = Piezoelectric Coefficient.

x	E_C+ (kV/cm)	E_C- (kV/cm)	P_r (µC/cm^2)	P_S (µC/cm^2)	d_{33} (pC/N)
0	6.29	-5.41	21.43	29.86	47±2
0.05	6.20	-5.08	10.96	22.77	41±3
0.10	2.86	-4.29	2.62	21.45	32±2
0.15	2.81	-3.54	1.68	18.95	38±3
0.20	1.33	-2.78	0.77	15.88	21±2

3.10. Conclusions

A novel bismuth-based complex perovskite solid solution, $(1-x)Pb(Sc_{1/2}Nb_{1/2})O_3$-$xBiScO_3$ (PSN-BS), has been successfully synthesized in the form of ceramics using the solid-state reaction method and sintering process. X-ray diffraction analysis confirms the formation of a pure perovskite phase of rhombohedral symmetry up to the solubility limit of x = 0.20. Microstructural investigations show a clear relationship between $BiScO_3$ content and increasing grain size, primarily attributed to the lower melting point of Bi_2O_3 compared to $Pb(Sc_{1/2}Nb_{1/2})O_3$, which facilitates the formation of a liquid phase at elevated sintering temperatures, enhancing mass transport and inducing substantial grain coarsening.

Dielectric characterizations reveal a normal ferroelectric phase transition in $Pb(Sc_{1/2}Nb_{1/2})O_3$. The compositions with x values of 0.05, 0.10, 0.15, and 0.20 exhibit relaxor-like dielectric frequency dispersion, marked by a shift to higher temperatures and a decrease in magnitude with increasing measurement frequency. The ceramics demonstrate typical relaxor characteristics, including broad and diffuse permittivity peaks and an increase in the temperature maximum of permittivity with higher measurement frequencies. Therefore, the substitution of $BiScO_3$ for $Pb(Sc_{1/2}Nb_{1/2})O_3$ induces a crossover from the ferroelectric phase to a relaxor state. The high temperature slope of $\varepsilon'(T)$ could be well described by a quadratic law, with the parameters d and ε_A indicating the change in diffuseness and maximum of the permittivity peak. The temperature dependences of the dielectric permittivity are found to satisfy the Vogel-Fulcher law, which provides insights into the dynamics of polar nanoregions (PNRs), revealing freezing temperatures of -24.97 °C and -48.82°C for the compositions of $0.90Pb(Sc_{1/2}Nb_{1/2})O_3$-$0.10BiScO_3$ and $0.85Pb(Sc_{1/2}Nb_{1/2})O_3$-$0.15BiScO_3$, respectively

The $0.90Pb(Sc_{1/2}Nb_{1/2})O_3$-$0.10BiScO_3$ solid solution presents notable properties, including a high saturation polarization (P_S = 21.45 μC/cm^2), a reasonable piezoelectric performance (d_{33} = 32 pC/N), and a low remanent polarization (Pr = 2.62 μC/cm^2), characteristic of relaxor behaviour. These properties render this ceramic advantageous for applications such as energy storage and electromechanical transduction which prioritize energy efficiency, stability, reduced temperature sensitivity, and cost-effectiveness over achieving maximum polarization levels.

Chapter 4.

Synthesis, Structure and Properties of a Novel Ternary Solid Solution with High T_C and High Piezo-/Ferroelectric Performances

4.1. Abstract

In this work, a novel solid solution by combining the ferroelectric $Pb(Sc_{1/2}Nb_{1/2})O_3$ and the binary ferroelectric $BiScO_3$-$PbTiO_3$ is developed. Different compositions of xPSN-(1-x)[$(BS)_{0.34}(PT)_{0.66}$], xPSN-(1-x)[$(BS)_{0.35}(PT)_{0.65}$], and xPSN-(1-x)[$(BS)_{0.36}(PT)_{0.64}$] pseudo-binary solid solutions (abbreviated as PSN-BS-PT) were successfully synthesized in the form of ceramics, with continuous solubility limit and compositionally driven phase transitions from tetragonal to morphotropic phase boundary (MPB) as the combination of tetragonal and rhombohedral phases. Notably, the MPB region in PSN-BS-PT is more extended than the $BiScO_3$-$PbTiO_3$ (BS-PT) solid solution. Also, PSN-BS-PT shows higher Curie temperatures (T_C) compared to traditional $Pb(Zr,Ti)O_3$ (PZT). The temperature-dependent behavior of the dielectric constant in the studied compositions exhibits characteristic features of relaxor ferroelectric materials with increasing amount of PSN. Furthermore, the frequency-dependent behavior of the temperature at which the maximum permittivity occurs adheres to the Vogel-Fulcher law. Excellent piezo-/ferroelectric performance as well as high T_C is achieved for the composition of $0.9(0.35BiScO_3$-$0.65PbTiO_3)$-$0.10Pb(Sc_{1/2}Nb_{1/2})O_3$: d_{33} = 625 pC/N, P_r = 27.42 μC/cm^2 , E_C = 21 kV/cm, and T_C = 363 °C. The results show that 10% substitution of $Pb(Sc_{1/2}Nb_{1/2})O_3$ for BS-PT increases the grain size by 98%, the remanent polarization (P_r) by 46%, and the piezoelectric coefficient (d_{33}) by 45%, which represents a significant improvement of the ferroelectric and piezoelectric performance. The partial phase diagram between $BiScO_3$-$PbTiO_3$ and $Pb(Sc_{1/2}Nb_{1/2})O_3$ is established, illustrating the various phases and MPB region. This research demonstrates the feasibility of developing a novel ternary solid solution system based on the BS-PT solid solution and shows that the addition of $Pb(Sc_{1/2}Nb_{1/2})O_3$ enhances the relaxor behavior and improves the piezoelectric performance, making it a promising candidate for use in various piezo-/ferroelectric applications, in particular at high temperatures and high electric fields.

4.2. Introduction

Piezo-/ferroelectric materials hold significant technological value owing to their versatile applications in various devices, including sensors, actuators, energy harvesting devices, transducers, ultrasonic motors, and other electromechanical systems.[7,27,65–67] In recent decades, there has been a rising demand for piezo-/ferroelectric materials capable of operating effectively across a wide range of temperatures and electric fields. This demand has emerged in applications such as regulating fuel in engines, monitoring nuclear reactors, sensing in deep-sea oil drilling, therapeutic applications, underwater transducers, and monitoring the health of aircraft turbine systems. This expanding array of applications underscores the growing importance of developing advanced piezo-/ferroelectric materials to meet the evolving requirements of modern technology.[49,68–71]

Pb(Zr, Ti)O_3 (PZT) holds a preeminent position among commercially significant piezo-/ferroelectric ceramics, mainly attributed to its exceptional electromechanical properties. Specifically, PZT is known for its impressive piezoelectric constant (d_{33}: 600–700 pC/N) and elevated Curie temperature (T_C: ~350 °C), especially within its morphotropic phase boundary (MPB) region, characterized by a combination of tetragonal and rhombohedral phases. However, PZT's application range is constrained by its low morphotropic phase boundary transition temperature (T_{MPB}), which falls below 200 °C, potentially leading to issues like depoling and aging.[2,72,73] Therefore, PZT's maximum operational temperature falls short of the requirements for high-temperature piezoelectric ceramics, particularly in demanding applications such as deep petroleum exploration, where temperatures frequently exceed 300 °C.[73,74]

Recently developed piezocrystals based on relaxor materials, such as $Pb(Mg_{1/3}Nb_{2/3})O_3$-$PbTiO_3$ (PMN-PT) and $Pb(Zn_{1/3}Nb_{2/3})O_3$-$PbTiO_3$ (PZN-PT), demonstrate significantly better piezoelectric performance compared to traditional PZT. They can generate higher piezoelectric responses, with values of the piezoelectric coefficient (d_{33}) ranging from 1500 to 4100 pC/N. However, PMN-PT and PZN-PT crystals or ceramics can work effectively only around room temperature because they have relatively low Curie temperatures (T_C < 200 °C) and even lower morphotropic phase boundary temperatures (T_{MPB} <100 °C). Also, they have a low coercive field (E_C < 3 kV/cm), which makes them unsuitable for high-power electromechanical transduction applications.[30,32]

Several $BiMeO_3$-$PbTiO_3$ solid solutions have been developed so far, but the $BiScO_3$-PbTiO (BS-PT) solid solution stands out due to its remarkable piezoelectric performance (d_{33} > 350 pC/N) and high Curie temperature (T_C > 400 °C) within its morphotropic phase boundary (MPB) compositions.[75–77] However, BS-PT solid solutions face a significant challenge: they become highly conductive, especially at elevated temperatures, which restricts their operational temperature range.[77,78] Also, the $BiScO_3$ can only be mixed with $PbTiO_3$ up to a limit of 40% $BiScO_3$, and the MPB region in this system is confined to a narrow compositional range of 34-36% $BiScO_3$.[75]

In this work, a novel solid solution by combining the relaxor ferroelectric $Pb(Sc_{1/2}Nb_{1/2})O_3$ and the binary ferroelectric $BiScO_3$-$PbTiO_3$ is synthesized through the solid state reaction method. Different compositions of xPSN-$(1-x)[(BS)_{0.34}(PT)_{0.66}]$, xPSN-$(1-x)[(BS)_{0.35}(PT)_{0.65}]$, and xPSN-$(1-x)[(BS)_{0.36}(PT)_{0.64}]$ pseudo-binary solid solutions (abbreviated as PSN-BS-PT) were synthesized in the form of ceramics which are marked by the blue dots on and around the red line in Figure 4.1. A systematic study is performed on the $(1-x)Pb(Sc_{1/2}Nb_{1/2})O_3$-$x(BiScO_3$-$PbTiO_3)$ in terms of synthesis, crystal structures analysis, ceramic microstructure, phase transitions, and characterizations of physical properties including dielectric, ferroelectric and piezoelectric properties.

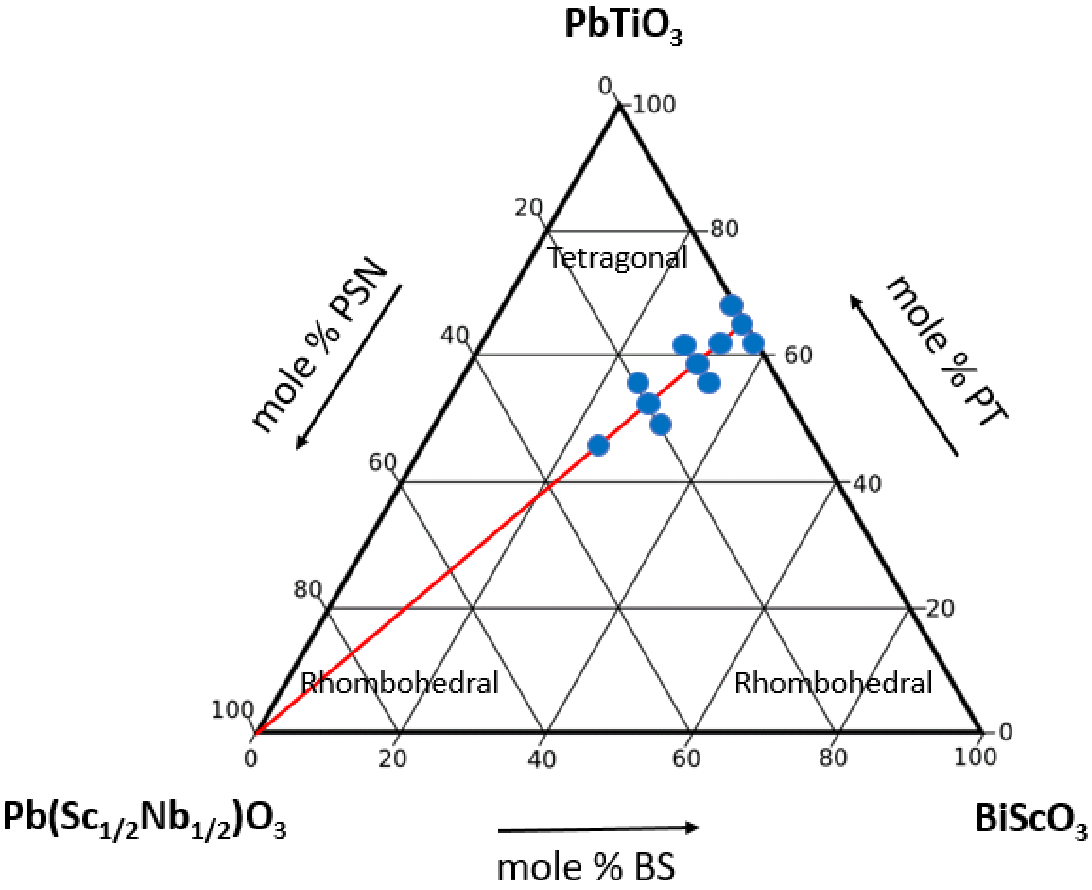

Figure 4.1: **The schematic ternary phase diagram features lead scandium niobate ($Pb(Sc_{1/2}Nb_{1/2})$, PSN), bismuth scandium ($BiScO_3$, BS), and lead titante ($PbTiO_3$, PT) as end members and their respective structural symmetries. Blue dots represent the compositions studied in this research.**

4.3. Solid State Synthesis and Ceramics Sintering

Various compositions ranged from x = 0.00 to 0.30 of the ternary solid solutions xPSN-(1-x)[$(BS)_{0.34}(PT)_{0.66}$], xPSN-(1-x)[$(BS)_{0.35}(PT)_{0.65}$], and xPSN-(1-x)[$(BS)_{0.36}(PT)_{0.64}$] were synthesized in the form of ceramics using the solid-state reaction method. Scandium oxide (Sc_2O_3, 99.9%, Aldrich), bismuth oxide (Bi_2O_3, 99.9%, Alpha Aesar), niobium oxide (Nb_2O_5, 99.9%, Alfa Aesar), lead oxide (PbO, 99.9%, Alfa Aesar), and titanium oxide (TiO_2, 99.5%, Alfa Aesar) were accurately weighed and then thoroughly mixed to achieve homogeneity in the raw materials.

The solid solutions were synthesized via a two-step solid-state reaction method. First, $ScNbO_4$ precursor phase was synthesized by reacting Sc_2O_3 and Nb_2O_5 powders (purity >99%) at 1000 ºC for 8 hours. After that, the pre-formed precursor was mixed with stoichiometric amounts of TiO_2, Bi_2O_3 and PbO. The resulting mixture was hand ground for 2 hours with 2 mol% PbO and 2 mol% Bi_2O_3 excess to compensate for their volatilization at high temperatures. Then the powder mixture was pressed into pellets, and subjected to calcination at 850 ºC for a duration of 6 hours in a muffle furnace. Following the calcination, the phase purity of the samples was assessed using powder X-ray diffraction (XRD). The calcined powders were then reground and ball-milled in ethyl alcohol for 24 hours to reduce the particle sizes. After air-drying, the resulting powder was mixed with 5 wt% polyvinyl alcohol (PVA) binder to form small round particles and favor achieving denser ceramics. The particles were filtered by passing them through a 120-mesh sieve (0.125 µm) and pressed into pellets. Samples were sintered at 1125 ºC for the duration of 2 hours with the heating rate of 300ºC/h and the cooling rate of 200ºC/h. X-ray powder diffraction (XRD) analysis was employed to investigate the purity and crystal structure of the sintered ceramics. Temperature dependence of dielectric permittivity was measured using a Novocontrol Alpha high-resolution broadband dielectric analyzer equipped with a high-temperature furnace. The morphology of the samples with different compositions was studied using helium ion microscopy (HIM). Ferroelectric and piezoelectric properties were measured using a RT-66 ferroelectric test system (Radian technology) and Berlincourt-type quasi state d_{33}/d_{31} meter, respectively.

4.4. Crystal Structure Analysis

The formation of phase(s) of the $(1-x)(0.35BiScO_3-0.65PbTiO_3)-xPb(Sc_{1/2}Nb_{1/2})O_3$ solid solution is investigated by powder X-ray diffraction (XRD) using Rigaku MiniFlex 6G system. Figure 4.2 illustrates the XRD patterns for $(1-x)(0.35BiScO_3-0.65PbTiO_3)-xPb(Sc_{1/2}Nb_{1/2})O_3$ with nominal compositions of x = 0.0, 0.05, 0.10, 0.20 and 0.30 after sintering.

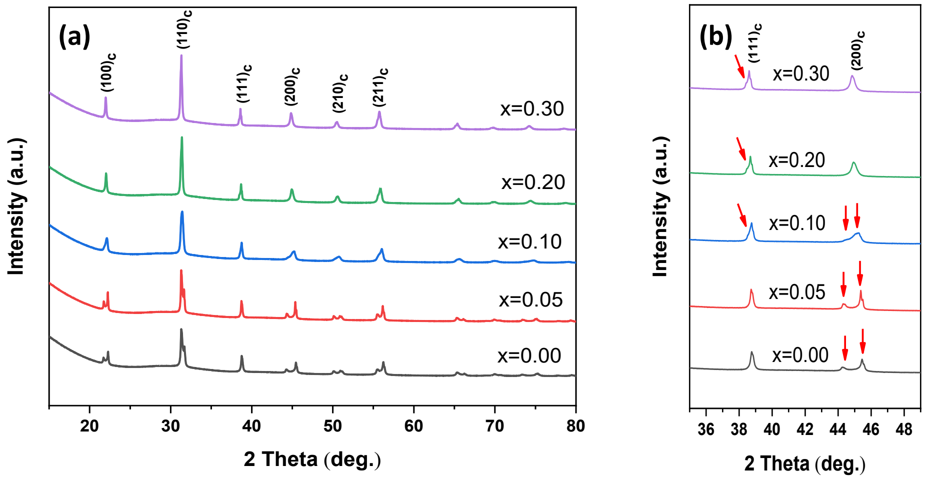

Figure 4.2: **Powder X-ray diffraction patterns obtained at room temperature of the (1-x)(0.35BiScO$_3$-0.65PbTiO$_3$)-xPb(Sc$_{1/2}$Nb$_{1/2}$)O$_3$ solid solution: (a) compositions of x = 0 - 0.30, and (b) their zoomed-in XRD patterns between 36° to 48°.**

The XRD patterns reveal crucial insights into the structural characteristics of the (1-x)(0.35BiScO$_3$-0.65PbTiO$_3$)-xPb(Sc$_{1/2}$Nb$_{1/2}$)O$_3$ solid solution. First of all, it is worth noting that all compositions crystallize in the perovskite structure, indicating a continuous solid solution between Pb(Sc$_{1/2}$Nb$_{1/2}$)O$_3$ and 0.35BiScO$_3$-0.65PbTiO$_3$. Secondly, the tetragonal phase symmetry is evident for x = 0, supported by prior research[75,77]. However, as the Pb(Sc$_{1/2}$Nb$_{1/2}$)O$_3$ content increases to 0.10, the (200)$_c$ peak splitting becomes less pronounced, and an additional shoulder appears in (111)$_c$, implying the formation of a distinct phase with different symmetry.

Significant observations are made concerning the splitting of the (200)$_c$ and (111)$_c$ peaks. In tetragonal unit cells, the (200)$_c$ peak splits into (200)$_c$-(002)$_c$ due to the extension of the lattice in one direction. The splitting is evident with 0.35BS-0.65PT and 0.95(0.35BS-0.65PT)-0.05PSN, but weaker splitting is observed for 10-30% Pb(Sc$_{1/2}$Nb$_{1/2}$)O$_3$ solid solutions. Similarly, in rhombohedral unit cells, the (111)$_c$ peak splits due to the lack of 90° angles. While the (111)$_c$ peak does not apparently split with 0% and 5% PSN, it broadens with 10-30% PSN. Overall, these observations suggest two conclusions: the addition of Pb(Sc$_{1/2}$Nb$_{1/2}$)O$_3$ induces a compositional phase transition, resulting in a higher percentage of the rhombohedral phase compared to the tetragonally dominant 0.35BS-0.65PT and 0.95(0.35BS-0.65PT)-0.05PSN compositions; and there is phase co-existence of rhombohedral and tetragonal phases in higher

$Pb(Sc_{1/2}Nb_{1/2})O_3$ content compositions. Consequently, these findings confirm the presence of a ternary morphotropic phase boundary (MPB) in (1-x)(0.35BS-0.65PT)-xPSN ternary solid solution.

Figure 4.3 shows X-ray diffraction (XRD) patterns for the solid solutions (1-x)(0.34$BiScO_3$-0.66$PbTiO_3$)-x$Pb(Sc_{1/2}Nb_{1/2})O_3$ and (1-x)(0.36$BiScO_3$-0.64$PbTiO_3$)-x$Pb(Sc_{1/2}Nb_{1/2})O_3$ at room temperature after sintering. The findings from these XRD patterns are similar with our earlier XRD analysis of the (1-x)(0.35BS-0.65PT)-xPSN solid solution. All compositions showed a crystalline perovskite structure, suggesting a continuous solid solution between both 0.34$BiScO_3$-0.66$PbTiO_3$ and 0.36BiScO3-0.64PbTiO3 binary solid solutions and $Pb(Sc_{1/2}Nb_{1/2})O_3$ up to 20%.

When the $Pb(Sc_{1/2}Nb_{1/2})O_3$ content reaches 0.20 for the (1-x)(0.34BS-0.66PT)-xPSN and to 0.1 for the (1-x)(0.36BS-0.64PT)-xPSN, the clear splitting of the $(200)_c$ peak becomes less noticeable, as indicated by the red arrows in Figure 4.3 (b and d). This indicates the formation of an additional phase with a different structure for these compositions. The presence of this phase is also supported by the appearance of a shoulder on the $(111)_c$ peak, as marked by the red arrows. These observations demonstrate the existence of a morphotropic phase boundary (MPB) region where both tetragonal and rhombohedral phase structures coexist. These findings are further confirmed by the successful fitting results obtained through Rietveld refinement of the (1-x)(0.35$BiScO_3$-0.65$PbTiO_3$)-x$Pb(Sc_{1/2}Nb_{1/2})O_3$, as presented in Figure 4.4 and Table 4.1. The refinement outcomes indicate a reduction in the proportion of the tetragonal phase and an increase in the content of the rhombohedral phase within the morphotropic phase boundary (MPB) region as the $Pb(Sc_{1/2}Nb_{1/2})O_3$ content rises. As x reaches 0.30, a more pronounced splitting is observed in the $(111)_c$ peaks, while the splitting in the $(200)_c$ peaks diminishes. This suggests a transformation towards a rhombohedral phase.

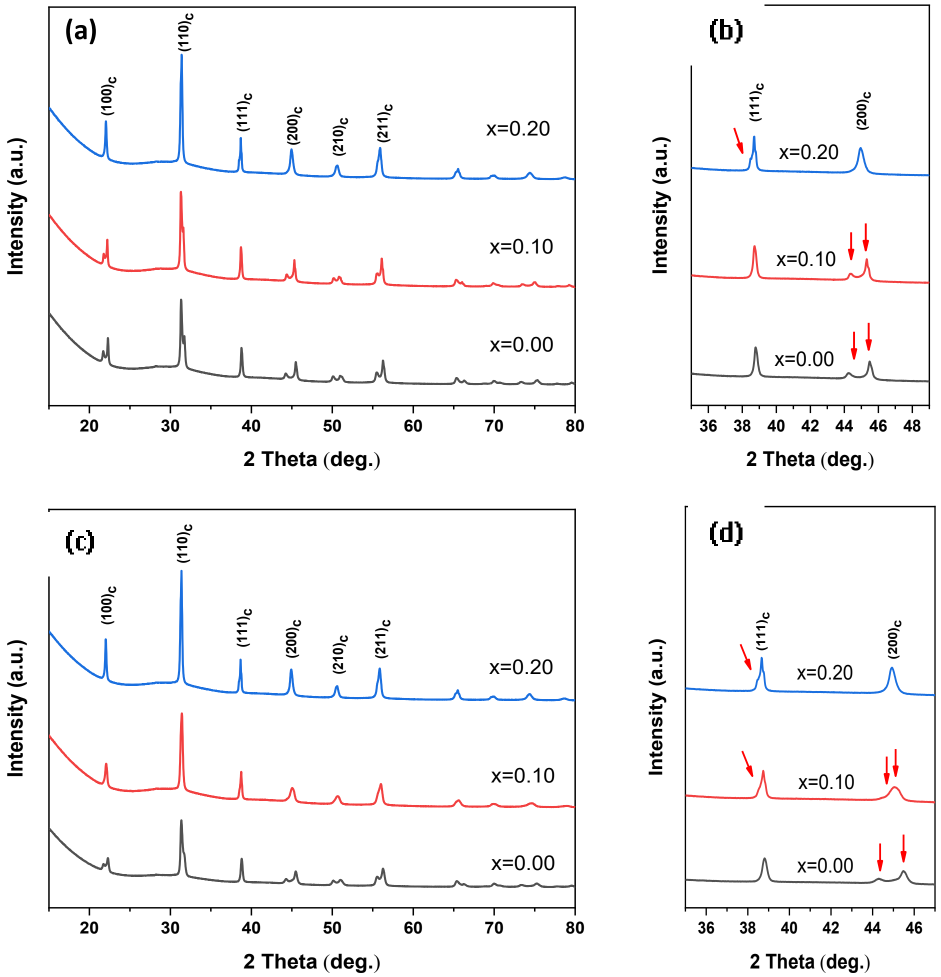

Figure 4.3: Powder X-ray diffraction patterns obtained at room temperature of the ceramics of (1-x)(0.34$BiScO_3$-0.66$PbTiO_3$)-xPb($Sc_{1/2}Nb_{1/2}$)O_3: (a) Compositions of x = 0 - 0.20, (b) Their zoomed-in XRD patterns between 36° to 48°; and (1-x)(0.36$BiScO_3$-0.64$PbTiO_3$)-Pb($Sc_{1/2}Nb_{1/2}$)O_3 solid solutions: (c) Compositions of x = 0 - 0.20; and (d) Their zoomed-in XRD patterns between 36° to 46°.

The refined lattice parameters and unit cell volumes of the (1-x)(0.35$BiScO_3$-0.65$PbTiO_3$)- xPb($Sc_{1/2}Nb_{1/2}$)O_3 solid solution are derived through Rietveld refinements performed on high-quality data collected from Bruker D8 Advance X-ray diffractometer and presented in Table 4.1 and visually represented in Figure 4.5.

As depicted in Figure 4.5, there is an observable increase in the lattice parameter 'a' as the PSN content rises, resulting in an expanded unit cell volume. This expansion can be attributed to the larger ionic radius of Pb^{2+} (r = 1.49 Å) in comparison to Bi^{3+} (r = 1.44 Å) at the A-site (coordination number = 12), as well as the larger ionic radius of

Nb^{5+} (r = 0.64 Å) and Sc^{3+} (r=0.745 Å) compared to Ti^{4+} (r = 0.605 Å) at the B-site (coordination number = 6).

Additionally, the angle 'α' for the rhombohedral phase increases as the $Pb(Sc_{1/2}Nb_{1/2})O_3$ content increases. With the increasing 'a' lattice parameter, the tetragonality, expressed as 'c/a,' decreases from 1.022 to 1.002. This value is relatively lower compared to the 'c/a' ratio of 1.023 for BS-PT within its respective morphotropic phase boundary (MPB) compositions.[77]

In the context of solid solutions based on $BiMeO_3$-$PbTiO_3$ with morphotropic phase boundary (MPB) regions, previous research has demonstrated a significant correlation between the 'c/a' ratio within their MPB regions and the corresponding MPB temperatures and Curie temperatures (T_Cs). Specifically, a higher 'c/a' ratio generally corresponds to higher MPB temperatures and T_Cs, whereas a smaller 'c/a' value is associated with lower MPB temperatures and T_Cs in these systems.[75,79,80] Therefore, it is reasonable to anticipate that the incorporation of more PSN into the BS-PT binary solid solution will lead to a decrease in both the MPB temperature and T_Cs.

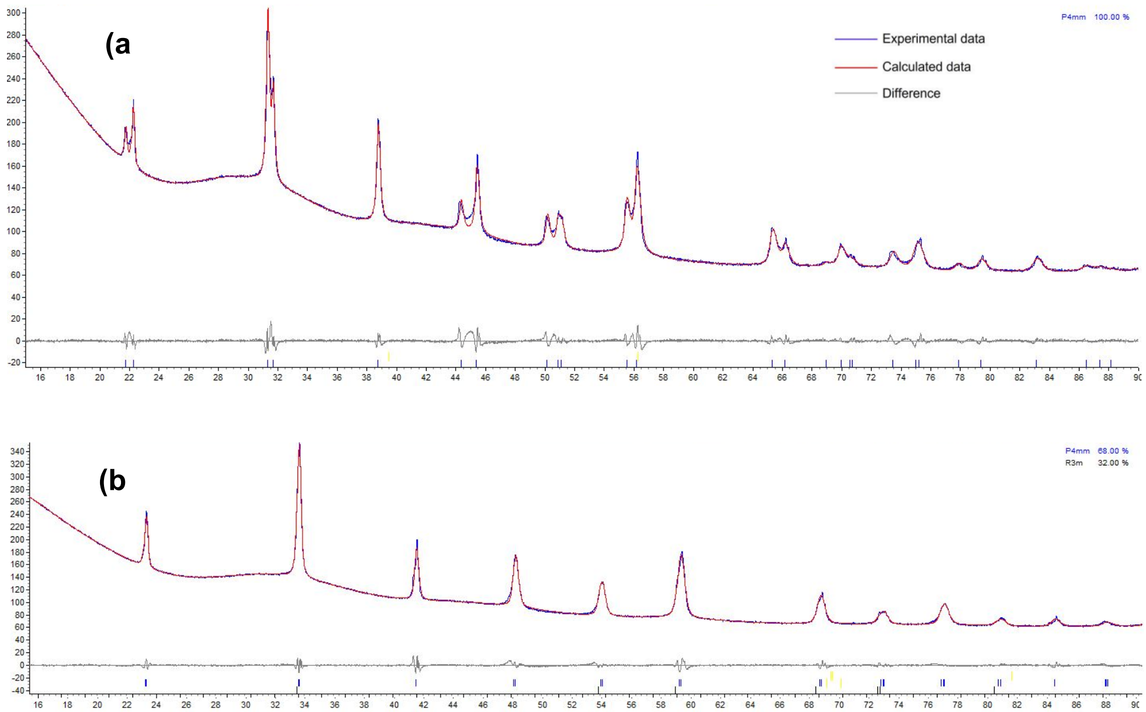

Figure 4.4: Rietveld refinement fitting the high-resolution X-ray diffraction data of the (1-x)(0.35$BiScO_3$-0.65$PbTiO_3$)-x$Pb(Sc_{1/2}Nb_{1/2})O_3$ solid solution: (a) x = 0; (b) x = 0.20.

Phase components (PC) and lattice parameters 'a' and 'c', tetragonality 'c/a', rhombohedral angle 'α', and unit cell volume 'V' of the (1-x)(0.35$BiScO_3$-0.65$PbTiO_3$)-x$Pb(Sc_{1/2}Nb_{1/2})O_3$ solid solution obtained by Rietveld refinements on the high-resolution XRD data. The subscripts “T” and “R” represent tetragonal and rhombohedral phases, respectively. P4mm and R3m are the corresponding space groups of the tetragonal and rhombohedral phases. The quality of the agreement between the experimental data and calculated data is assessed by the residual R factors (R_{wp}, R_{exp}, and R_p). Low R_{wp} (< 5%) values have been achieved for all the compositions, indicating reliable refinement results.

Table 4.1: Variations of the a, c, α lattice parameters, and volume of the unit cell as a function of $Pb(Sc_{1/2}Nb_{1/2})O_3$ content for the $(1\text{-}x)(0.35BiScO_3\text{-}0.65PbTiO_3)\text{-}xPb(Sc_{1/2}Nb_{1/2})O_3$.

x	PC	a_T (Å)	c_T (Å)	c/a	V_T (Å^3)	a_R (Å)	α_R (°)	V_R (Å^3)	R_{wp}, R_{exp} and R_p(%)
0	P4mm (100%)	3.99268±0.00053	4.08276±0.00056	1.022	65.00537±0.01952	/	/	/	3.141, 0.035, 1.721
0.05	P4mm (100%)	3.99811±0.00013	4.08063±0.00016	1.020	65.22839±0.00493	/	/	/	3.084, 0.751, 1.517
0.10	P4mm(63.89%) +R3m(36.11%)	4.01568±0.00027	4.05565±0.00032	1.009	65.40011±0.00032	4.03914±0.00115	89.76303±0.03093	65.89548±0.04285	2.747, 0.850, 1.561
0.20	P4mm(68.06%) +R3m(31.94%)	4.03047±0.00024	4.04268±0.00036	1.003	65.67195±0.00967	4.04490±0.00176	89.82420±0.04096	66.17859±0.08628	2.777, 0.864, 1.572
0.30	P4mm(90.02%) +R3m(9.98%)	4.03820±0.00041	4.04834±0.00062	1.002	66.01654±0.01669	4.05070±0.00227	89.88537±0.04114	66.46429±0.11172	3.039, 0.846, 2.352

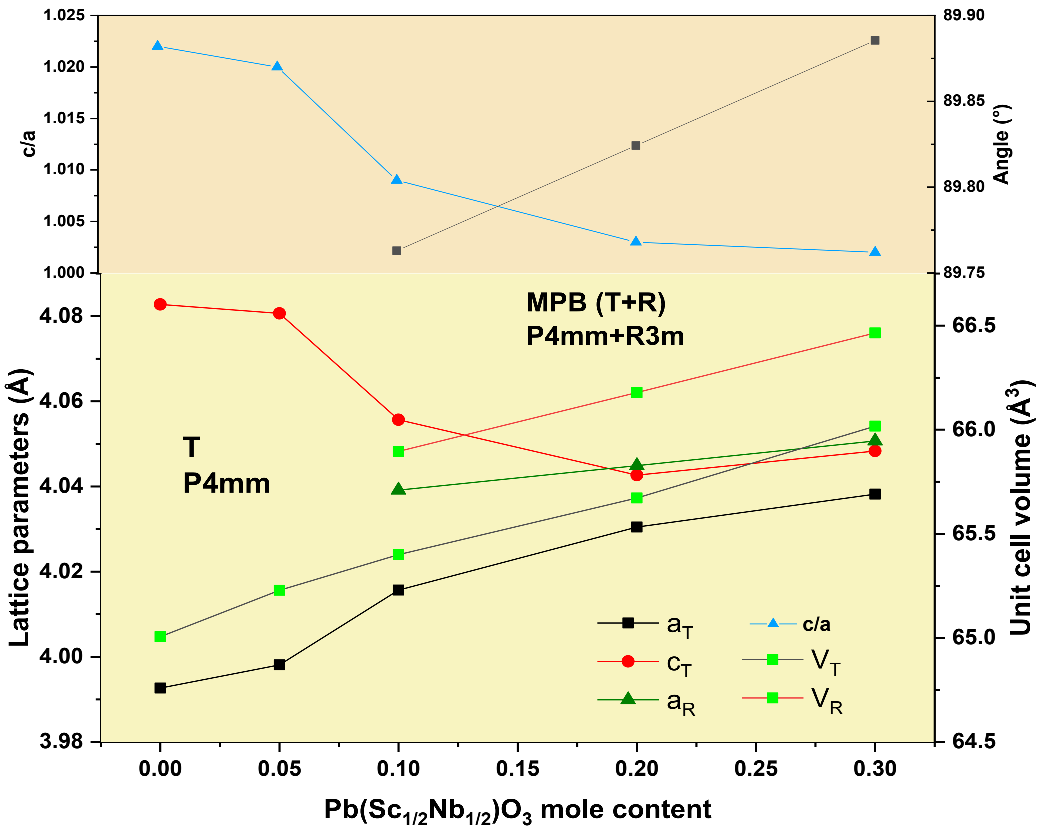

Figure 4.5: **Variations of the room-temperature 'a' and 'c' lattice parameters, 'α_R' Rhombohedral angle, 'c/a', and 'V' as a function of $Pb(Sc_{1/2}Nb_{1/2})O_3$ content for the $(1-x)(0.35BiScO_3-0.65PbTiO_3)-xPb(Sc_{1/2}Nb_{1/2})O_3$ solid solution.**

4.5. Ceramic Microstructure Analysis

High-quality ceramics from the $(1-x)(0.35BiScO_3-0.65PbTiO_3)-xPb(Sc_{1/2}Nb_{1/2})O_3$ solid solution were successfully produced after the sintering process. Table 4.2 records the apparent density, theoretical density, and relative density of the sintered ceramics, demonstrating an acceptable value of relative density for all the samples.

Table 4.2: **Apparent density, theoretical density, and relative density of $(1-x)(0.35BiScO_3-0.65PbTiO_3)-xPb(Sc_{1/2}Nb_{1/2})O_3$ solid solution ceramics.**

x	Apparent density (g/cm³)	Theoretical density (g/cm³)	Relative density
0	7.16	7.72	0.92

0.05	7.19	7.73	0.93
0.10	6.81	7.72	0.88
0.20	6.97	7.74	0.90
0.30	7.20	7.76	0.92

In order to examine the microstructure of the sintered ceramics, we captured surface images of the pellets through the utilization of helium ion microscopy (HIM, Zeiss Orion NanoFAB equipment) presented in Figure 4.6. It is evident from the images that all the sintered ceramics exhibit compact structures characterized by distinct grain boundaries and minimal pore formation. The obtained images revealed polygonal shape grains and a limited presence of pores and defects, aligning with our expectations due to the favorable relative densities of the samples.

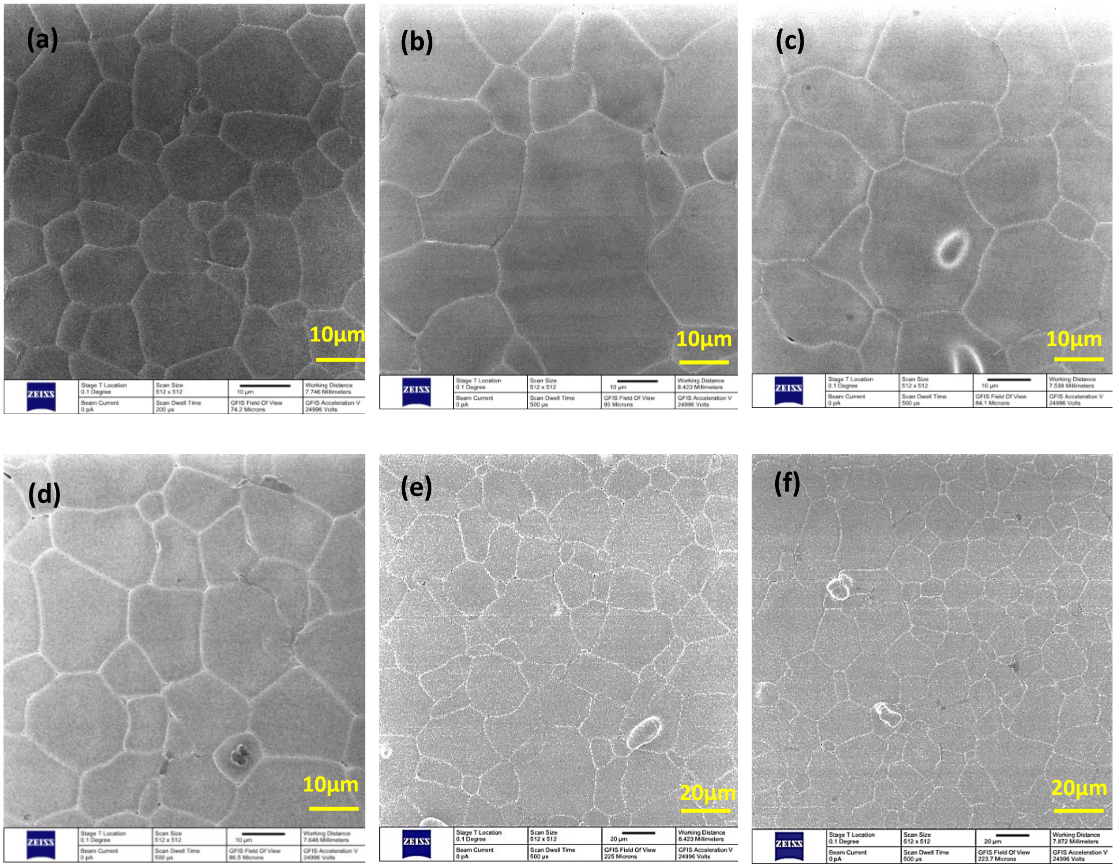

Figure 4.6: **Helium ion microscopy (HIM) images of sintered (1-x)($0.35BiScO_3$-$0.65PbTiO_3$)-$xPb(Sc_{1/2}Nb_{1/2})O_3$ solid solution ceramics for various compositions: (a) x = 0; (b) x = 0.10; (c) x = 0.20; and (d) x = 0.30 with 10μm scale; (e) x = 0.10, (f) x = 0.30 with 20 μm as scale.**

The average grain sizes, as determined from the HIM images, are presented in Figure 4.7. The grain size distribution and the average grain size was calculated by ImageJ software. Analyzing the images, a discernible pattern emerges in the grain size, exhibiting a substantial increase from 0% to 10% PSN, followed by a subsequent decrease at 20% and 30% PSN namely nonmonotonic trend. The trend shows the advantages of the substitution of $Pb(Sc_{1/2}Nb_{1/2})O_3$ for $0.35BiScO_3$-$0.65PbTiO_3$ up to 10%. These findings confirm the visual trends, with the average grain size experiencing a remarkable 98% growth from 0% to 10% PSN.

Larger grain sizes are frequently associated with superior piezoelectric and ferroelectric performance. This connection arises from the fact that larger grains result in fewer grain boundaries and a more contiguous structure. Consequently, this maximizes the potential orientations and polarizability within the material, contributing to enhanced performance.[81,82] Furthermore, the addition of a relaxor component to a ferroelectric material can sometimes inhibit grain growth. This is because relaxor materials tend to have a disordered structure at the nanoscale, which can impede grain growth in the composite. Smaller grain sizes can affect the material's mechanical properties and can be advantageous for certain applications where fine-grained materials are preferred.[83,84]

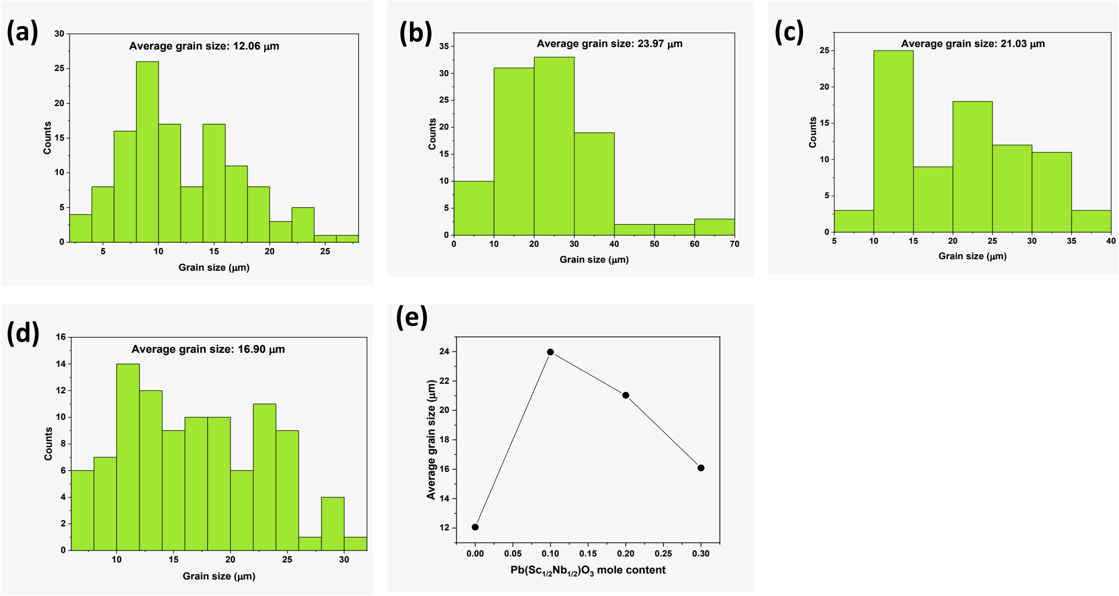

Figure 4.7: **Average grain size values for (1-x)(0.35BiScO$_3$-0.65PbTiO$_3$)-xPb(Sc$_{1/2}$Nb$_{1/2}$)O$_3$ solid solution ceramics, determined using Image J software based on HIM images, are displayed for various compositions: (a) x = 0; (b) x = 0.10; (c) x = 0.20; (d) x = 0.30. The graph (e) illustrates the relationship between average grain size and Pb(Sc$_{1/2}$Nb$_{1/2}$)O$_3$ mole content.**

4.6. Dielectric Properties and Phase Transition

The dielectric constant ε' and dielectric loss tangent tan δ of the (1-x)(0.35BiScO$_3$-0.65PbTiO$_3$)-xPb(Sc$_{1/2}$Nb$_{1/2}$)O$_3$ solid solution ceramics were measured at different frequencies in the temperature range of 100 ºC - 600 ºC upon cooling and are presented in Figure 4.8.

High Curie temperatures (T_Cs > 250 °C) have been observed in this solid solution system. The Curie temperature (T_C) for the material composed of $0.35BiScO_3$-$0.65PbTiO_3$ has been determined to be 436 °C upon cooling, which aligns with the findings of earlier research.[78,85]

As shown in Figure 4.8 (a), the temperature peak does not show any frequency dependence for the composition of $0.35BiScO_3$-$0.65PbTiO_3$, indicating a normal ferroelectric phase transition. Whereas, for all the other compositions (x = 0.05, 0.10, 0.20. 0.30), the peak temperature was observed to be frequency dependent showing possible relaxor ferroelectric behavior in the $(1-x)(0.35BiScO_3$-$0.65PbTiO_3)$-$xPb(Sc_{1/2}Nb_{1/2})O_3$ solid solution.

The temperature dependence of the dielectric constant (ε') for all compositions within the range of $(1-x)(0.35BiScO_3$-$0.65PbTiO_3)$-$xPb(Sc_{1/2}Nb_{1/2})O_3$ up to x = 0.3 at a frequency of 100 kHz is illustrated in Figure 4.8 (f). The data in this figure shows a decreasing trend in the dielectric constant as the value of x increases. The Curie temperatures of this solid solution show a descending trend as well, which is similar to the decreasing T_C trend in $Pb(Sc_{1/2}Nb_{1/2})O_3$ - $PbTiO_3$.[86] Compared with $0.35BiScO_3$-$0.65PbTiO_3$ ceramic (T_C = 436 °C), the T_C of the $(1-x)(0.35BiScO_3$-$0.65PbTiO_3)$-$xPb(Sc_{1/2}Nb_{1/2})O_3$ solid solution has been decreased to 398°C at the composition of x = 0.05, 363°C at the composition of x = 0.10 and continue decreasing to 255 °C at the composition x = 0.3. These observations align closely with the predictions outlined in the preceding 'crystal structure analysis' section. As anticipated, the introduction of additional PSN into the BS-PT binary solid solution has resulted in a reduction in the 'c/a' ratio, and as a consequence, a corresponding decrease in Curie temperatures (T_Cs). This corroborates our initial hypothesis that a decrease in 'c/a' would lead to lower T_Cs.

Also, increasing the PSN content leads to wider and more diffuse dielectric profiles, indicating an increase in full width at half maximum (FWHM) as detailed in Table 4.3. This suggests a higher level of structural disorder and enhanced relaxor behavior.[46,47,87]

All T_Cs upon cooling and heating for $(1-x)(0.35BiScO_3$-$0.65PbTiO_3)$-$xPb(Sc_{1/2}Nb_{1/2})O_3$ solid solutions are reported in Table 4.3. The different values of T_Cs obtained upon heating and cooling arise from thermal hysteresis and indicate the first-order phase transition behavior.[88]

It's worth mentioning that certain dielectric irregularities have been detected at temperatures higher than the Curie temperatures (T_Cs) for some compositions. For instance, at x = 0.10 for the f = 1 kHz, there is a distinct anomaly at approximately 450 °C, which is likely indicative of dielectric relaxation.[87] The observed dielectric relaxation behavior, characterized by a notably enhanced dielectric constant with a thermally activated process, can be attributed to the Maxwell-Wagner extrinsic effect. This phenomenon is intimately connected to the interfaces present within ceramic samples, encompassing the interfaces at surface layers, grain boundaries, and electrode-sample contacts. These interfaces play a pivotal role in facilitating the formation of depletion layers, which subsequently give rise to Maxwell-Wagner-type relaxations. In the context of dielectric properties, Debye-like dipolar relaxation typically involves the reorientation of dipoles in response to an applied electric field, resulting in a time-dependent polarization response. Maxwell-Wagner-type relaxations, on the other hand, are associated with the non-uniform distribution of electric charge within heterogeneous materials, causing charge accumulation at interfaces and inducing relaxation effects.[89,90]

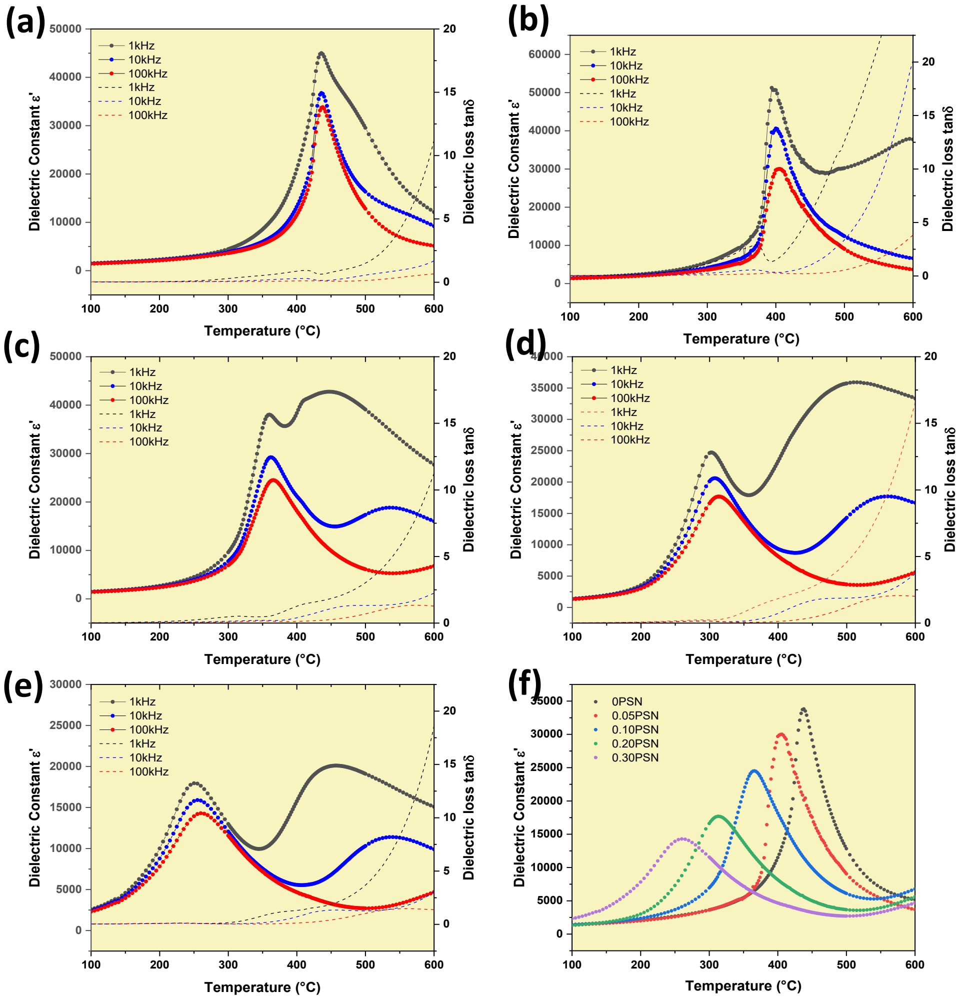

Figure 4.8: Variation of dielectric constant ε' and tan δ as a function of temperature for the (1-x)(0.35BiScO$_3$-0.65PbTiO$_3$)-xPb(Sc$_{1/2}$Nb$_{1/2}$)O$_3$ solid solutions: (a) x = 0; (b) x = 0.05; (c) x = 0.10; (d) x = 0.20; (e) x = 0.30 measured at 1 kHz, 10 kHz, and 100 kHz upon cooling; (f) variations of the dielectric constant ε' as a function of temperature on all the compositions at f = 100 kHz.

Table 4.3: FWHMs calculated for f = 100 kHz for the (1-x)(0.35BiScO$_3$-0.65PbTiO$_3$)-xPb(Sc$_{1/2}$Nb$_{1/2}$)O$_3$ solid solutions; T$_{C/max}$ obtained from dielectric measurement upon heating and cooling. Errors were determined by the step size of the dielectric temperature measurements.

x	FWHM (ºC)	T$_{C/max}$ for heating (ºC)	T$_{C/max}$ for cooling (ºC)	∆T$_{max}$ (ºC)
0	66.28±1.90	440±2	436±2	/
0.05	81.13±2.62	406±2	398±2	4

0.10	94.05±2.53	368±2	363±2	6
0.20	104.72±2.90	314±2	308±2	12
0.30	120.84±2.50	260±2	255±2	10

Variation of dielectric constant ε' and tan δ as a function of temperature for the $(1-x)(0.34BiScO_3-0.66PbTiO_3)-xPb(Sc_{1/2}Nb_{1/2})O_3$ and $(1-x)(0.36BiScO_3-0.64PbTiO_3)-xPb(Sc_{1/2}Nb_{1/2})O_3$ solid solutions is presented in Figure 4.9. The peaks observed in the temperature dependence of the dielectric constant refer to the ferroelectric to paraelectric phase transition at the Curie/maximum temperature ($T_{C/max}$).

In the investigation of compositions $0.34BiScO_3-0.66PbTiO_3$ and $0.36BiScO_3-0.64PbTiO_3$, a notable feature is the frequency-independent temperature peak in the dielectric response, similar to the behavior observed in $0.35BiScO_3-0.65PbTiO_3$. This suggests a typical ferroelectric phase transition, as illustrated in Figure 4.9 (a) and Figure 4.9 (d). In all the other compositions in both $(1-x)(0.34BiScO_3-0.66PbTiO_3)-xPb(Sc_{1/2}Nb_{1/2})O_3$ and $(1-x)(0.36BiScO_3-0.64PbTiO_3)-xPb(Sc_{1/2}Nb_{1/2})O_3$, the temperature peaks are frequency-dependent, showing possible relaxor ferroelectric behavior, similar to what was observed in the $(1-x)(0.35BiScO_3-0.65PbTiO_3)$- $xPb(Sc_{1/2}Nb_{1/2})O_3$ solid solution.

All the compositions exhibit high Curie temperatures (T_Cs > 300 °C), which aligns with the trend observed in the $(1-x)(0.35BiScO_3-0.65PbTiO_3)$- $xPb(Sc_{1/2}Nb_{1/2})O_3$ solid solution. Notably, increasing the PSN content in $(1-x)(0.34BiScO_3-0.66PbTiO_3)-xPb(Sc_{1/2}Nb_{1/2})O_3$ and $(1-x)(0.36BiScO_3-0.64PbTiO_3)-xPb(Sc_{1/2}Nb_{1/2})O_3$ leads to a reduction in T_C, consistent with the influence of PSN on decreasing T_C as seen in the $(1-x)(0.35BiScO_3-0.65PbTiO_3)$- $xPb(Sc_{1/2}Nb_{1/2})O_3$ solid solution. The Curie temperatures decrease as the PSN concentration rises, with $(1-x)(0.34BiScO_3-0.66PbTiO_3)-xPb(Sc_{1/2}Nb_{1/2})O_3$ and $(1-x)(0.36BiScO_3-0.64PbTiO_3)-xPb(Sc_{1/2}Nb_{1/2})O_3$ displaying T_C values of 311 °C and 316 °C, respectively, at their maximum PSN content ($x = 0.2$).

Figure 4.9 (a) shows that at approximately 500 °C, a distinct anomaly is evident at lower frequency (1 kHz) in $0.34BiScO_3-0.66PbTiO_3$, which indicates dielectric relaxation. This anomaly is likely linked to grain boundaries and other defects in the material and their influence on the dielectric properties. The dielectric response curves in lossy materials may appear broader and skewed compared to the sharp, well-defined curves seen in insulators. This broadening is a result of the energy dissipation associated with the material's conductivity.[87]

The T_Cs of all compositions upon cooling are plotted in Figure 4.10 and detailed in Table 4.4. There is a linear dependence of $T_{C/max}$ on composition for all the compositions which is mostly observed in Pb-based and many other Bi-based perovskite systems[91]. This linear trend underscores the consistent reduction in T_C with increasing PSN content in (1-x)(0.34$BiScO_3$-0.66$PbTiO_3$)-x$Pb(Sc_{1/2}Nb_{1/2})O_3$ and (1-x)(0.36$BiScO_3$-0.64$PbTiO_3$)-x$Pb(Sc_{1/2}Nb_{1/2})O_3$, and (1-x)(0.35$BiScO_3$-0.65$PbTiO_3$)- x$Pb(Sc_{1/2}Nb_{1/2})O_3$ solid solutions.

Figure 4.10 (b) provides a clear depiction of the ΔT_{max} values (which represents the temperature difference between the maximum values observed at frequencies of 1 kHz and 100 kHz) for all compositions. Notably, a consistent trend emerges, revealing that ΔT_{max} increases by addition of more PSN, particularly up to 20%. In dielectric spectroscopy, a broader ΔT_{max} is often linked to frequency-dependent behavior, indicative of variations in a material's dielectric properties across different frequencies. This observed behavior aligns closely with the typical characteristics associated with relaxor materials. The increase in ΔT_{max} can be seen as a reflection of the material's heightened structural disorder and microstructural complexity resulting from the introduction of PSN. This complexity is accompanied by a frequency-dependent dielectric response, which is an indicator of relaxor ferroelectric characteristics. In relaxor ferroelectrics, the dipole alignment is more disordered and diffuse compared to conventional ferroelectrics, contributing to the broader ΔT_{max} observed in this study. Relaxor ferroelectrics typically exhibit a frequency-dependent response, which means that their piezoelectric properties can vary with the frequency of the applied electric field. This behavior can be harnessed for specific applications where tunable piezoelectric responses are needed over a range of frequencies.[11]

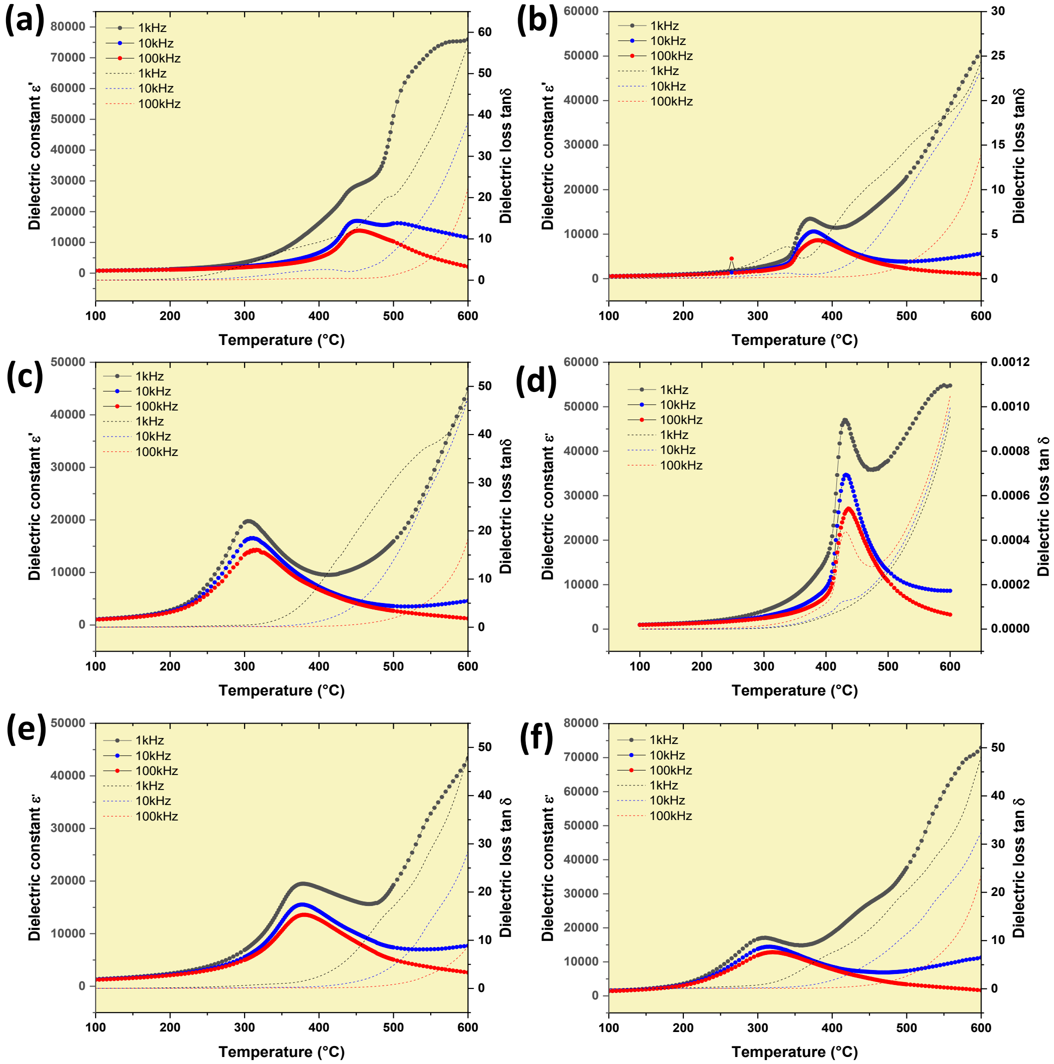

Figure 4.9: Variation of dielectric constant ε' and tan δ as a function of temperature for the (1-x)(0.34BiScO$_3$-0.66PbTiO$_3$)-xPb(Sc$_{1/2}$Nb$_{1/2}$)O$_3$ solid solution: (a) x = 0; (b) x = 0.10; (c) x = 0.20; and for the (1-x)(0.36BiScO$_3$-0.64PbTiO$_3$)-xPb(Sc$_{1/2}$Nb$_{1/2}$)O$_3$ solid solution: (d) x = 0; (e) x = 0.10, (f) x = 0.20 measured at 1 kHz, 10 kHz, and 100 kHz upon cooling.

Table 4.4: T$_{C/max}$ obtained from dielectric measurement upon heating and cooling. Errors were determined by the step size of the dielectric temperature measurements. ΔT$_{max}$ represents the temperature difference between the maximum values observed at frequencies of 1 kHz and 100 kHz. Errors were determined by the step size of the dielectric temperature measurements.

Composition	x	T$_{C/max}$ for heating (°C)	T$_{C/max}$ for cooling (°C)	ΔT$_{max}$ (°C)

(1-x)(0.34BiScO$_3$-0.66PbTiO$_3$)-xPb(Sc$_{1/2}$Nb$_{1/2}$)O$_3$	**0.00**	456±2	453±2	0
	0.10	380±2	376±2	10
	0.20	315±2	311±2	12
(1-x)(0.36BiScO$_3$-0.64PbTiO$_3$)-xPb(Sc$_{1/2}$Nb$_{1/2}$)O$_3$	**0.00**	434±2	433±2	0
	0.10	383±2	379±2	6
	0.20	320±2	316±2	10

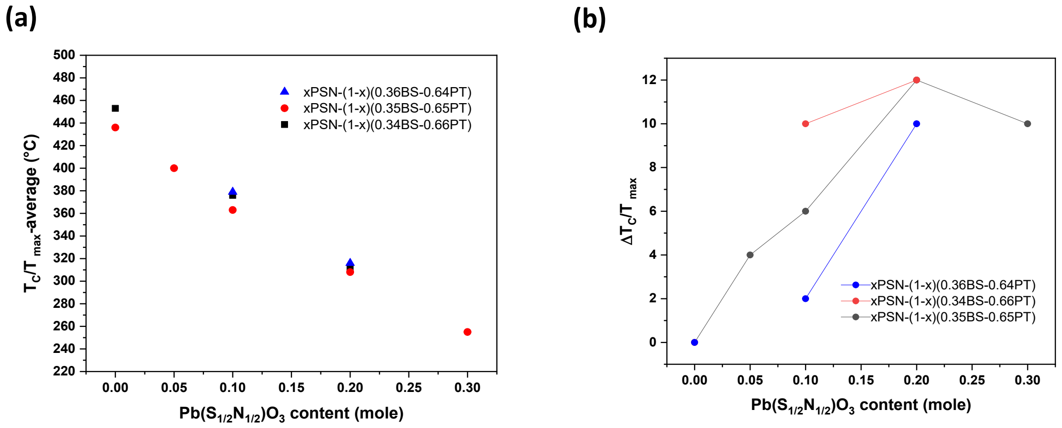

Figure 4.10: **Variations of the (a) Curie temperatures and (b) ΔT_{max} as a function of Pb(Sc$_{1/2}$Nb$_{1/2}$)O$_3$ mole content for the (1-x)(BiScO$_3$-PbTiO$_3$)-xPb(Sc$_{1/2}$Nb$_{1/2}$)O$_3$ solid solution, obtained from dielectric measurements upon cooling.**

From the structural and dielectric investigations conducted, a graph depicting alterations in T_C (Curie temperature) and T_{max} (maximum temperature) concerning the composition is presented. This graph serves as a partial structural phase diagram, illustrating the behavior of the (1-x)(0.35BiScO$_3$-0.65PbTiO$_3$)-xPb(Sc$_{1/2}$Nb$_{1/2}$)O$_3$ solid solution. In this diagram, the red dots pinpoint the Curie and maximum temperatures (T_C or T_{max}), revealing a consistent decrease in these temperatures as the PSN content increases, as depicted in Figure 4.11.

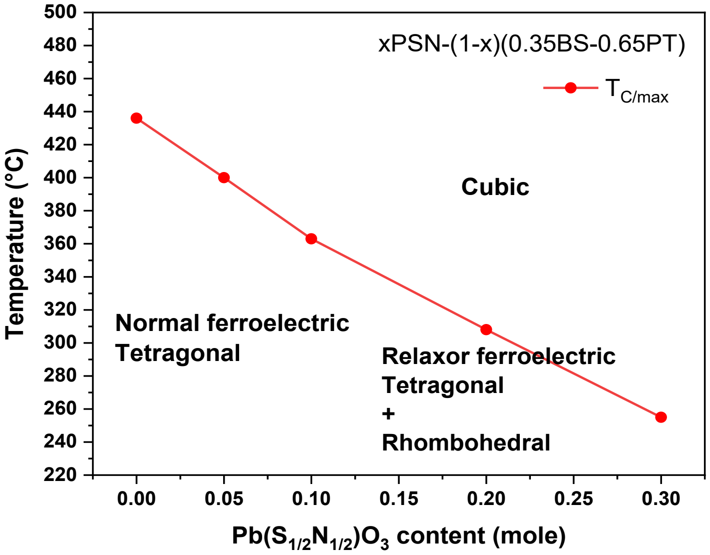

Figure 4.11: Partial structural phase diagram illustrating the behavior of (1-x)(0.35BiScO$_3$-0.65PbTiO$_3$)-xPb(Sc$_{1/2}$Nb$_{1/2}$)O$_3$ solid solution. Red dots mark Curie and maximum temperatures (T_C and T_{max}).

4.7. Dielectric Relaxation

The frequency-dependent behavior of the temperature at which the maximum permittivity occurs adheres to the Vogel-Fulcher law for (1-x)(0.35BiScO$_3$-0.65PbTiO$_3$)-xPb(Sc$_{1/2}$Nb$_{1/2}$)O$_3$ solid solutions with x = 0.10 and x = 0.20. This law includes a freezing temperature denoted as T_f, which signifies the temperature at which the polar nanoregions (PNRs) contributing to the relaxor polarization become immobilized or freeze.

Figure 4.12 displays the outcome of fitting maximum temperature (T_{max}) versus frequencies for both of the compositions using the Vogel-Fulcher equation. The fitting results yielded a freezing temperature of 341℃ and an activation energy (E_a) of 0.026 eV for x = 0.10 and freezing temperature of 268℃ and an activation energy of 0.059eV for the sample with x = 0.20. Sample with 20% PSN shows higher activation energy (E_a) comparing to sample with 10% PSN. This elevated E_a signifies a more substantial energy barrier for the polarization processes in the material. Essentially, it requires more energy to initiate the processes, often attributed to an intricate microstructure and a less ordered arrangement of polar nanoregions, which is a common feature linked to relaxor behavior.[55,92]

Also, the sample with 20% PSN displays a lower T_f of 268°C. A lower T_f indicates that polar nanoregions, contributing to relaxor polarization, become immobilized at lower temperatures. This change is a clear indication of enhanced relaxor properties due to the introduction of PSN. The lower T_f reflects a more diffuse and less ordered polarization response, which has been achieved by increasing the PSN content from 10% to 20%.[14]

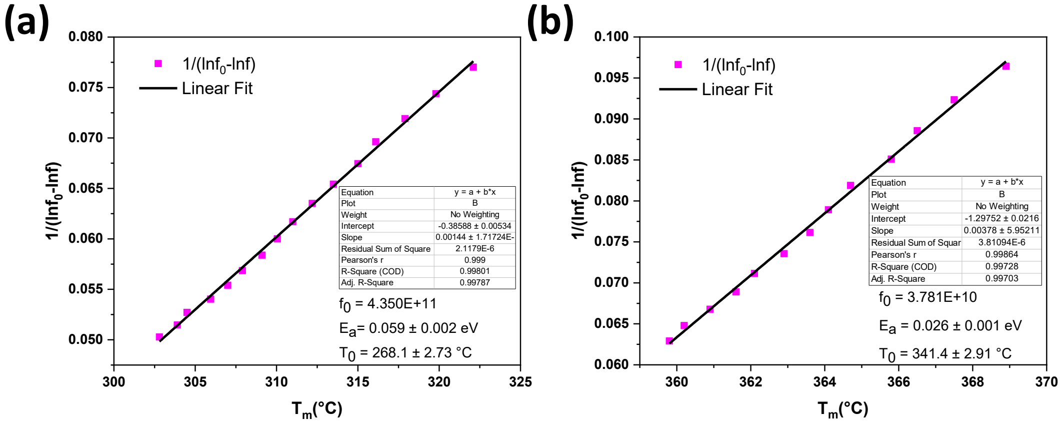

Figure 4.12: Fitting of the dielectric relaxation of the (1-x)(0.35$BiScO_3$-0.65$PbTiO_3$)-x$Pb(Sc_{1/2}Nb_{1/2})O_3$ ceramics to the Vogel-Fulcher law: (a) x = 0.10, and (b) x = 0.20.

4.8. Poling Effect on Piezoelectric Performance

The influence of poling conditions on the piezoelectric properties of BS-PT (both single crystal and ceramic) is a well-established fact. To investigate how temperature and duration of poling impacts the piezoelectric characteristics of (1-x)(0.35$BiScO_3$-0.65$PbTiO_3$)-x$Pb(Sc_{1/2}Nb_{1/2})O_3$ ceramics, poling experiments were conducted at different temperatures (150℃ and 200℃), with different durations (15min and 60min). Specifically, samples were poled at temperatures below Curie Temperature (T_C) and electric field higher their coercive field (near 30kV/cm).

The ceramics were first heated to the designated temperature, held at that temperature for ten minutes, applied the electric field and held for a certain duration, and then cooled back to room temperature while maintaining the applied electric field. The poling condition and resulting quasistatic piezoelectric properties measured at room temperature after various poling conditions are detailed in Table 4.5.

In the case of (1-x)(0.35$BiScO_3$-0.65$PbTiO_3$)-xPb($Sc_{1/2}Nb_{1/2}$)O_3 ceramics, when the poling process is carried out at higher temperatures, particularly at 200 °C, comparing to 150 °C, there is a noticeable decline in the piezoelectric constant. This finding implies that the deterioration of piezoelectric properties caused by the electric field is influenced by temperature in (1-x)(0.35$BiScO_3$-0.65$PbTiO_3$)-xPb($Sc_{1/2}Nb_{1/2}$)O_3 ceramics. Also, based on Table 4.5, it can be inferred that the duration of the poling process plays a significant role in determining piezoelectric performance. To achieve optimal results, it is essential for the dipoles to have ample time for rotation and alignment in accordance with the direction of the electric field.

Table 4.5: Variation in piezoelectric coefficient (d_{33}) for (1-x)(0.35$BiScO_3$-0.65$PbTiO_3$)-xPb($Sc_{1/2}Nb_{1/2}$)O_3 ceramics with x = 0.10 and x = 0.20 and different poling temperatures and poling duration time.

Composition	Poling temperature (℃)	Duration of poling (min)	d_{33}(pC/N)
0.9(0.35$BiScO_3$-0.65$PbTiO_3$)-0.10Pb($Sc_{1/2}Nb_{1/2}$)O_3	150	15	408±17
	150	120	625±21
	200	15	426±11
	200	120	341±8
0.8(0.35$BiScO_3$-0.65$PbTiO_3$)-0.2Pb($Sc_{1/2}Nb_{1/2}$)O_3	150	15	238±9
	150	120	383±8
	200	15	252±12
	200	120	226±6

The decrease in piezoelectric properties upon poling has been reported before in piezoelectric single crystals and ceramics, often referred to as the "over-poling effect". This effect arises due to an electric field-induced phase transition into the monoclinic state. In cases of over-poling, it has been demonstrated that the applied electric field amplifies the presence of the monoclinic phase component at the expense of the rhombohedral phase. This shift adversely impacts piezoelectric performance because the piezoelectric response of the monoclinic phase is inferior to that of the rhombohedral phase in compositions near the morphotropic phase boundary (MPB).[93]

The findings from this study indicate that poling conducted at 200℃, results in a degradation of piezoelectric properties. This degradation occurs because higher temperatures reduce the energy barrier required for the induced monoclinic phase transition to occur.

4.9. Ferroelectric and Piezoelectric Properties

In Figure 4.13, the polarization-electric field (P-E) hysteresis loops and piezoelectric properties are presented for the (1-x)(0.35$BiScO_3$-0.65$PbTiO_3$)-x$Pb(Sc_{1/2}Nb_{1/2})O_3$ ceramics across various compositions at room temperature, measured at a frequency of 10 Hz. Also, the remanent polarization (P_r), coercive field (E_C), and the piezoelectric coefficient (d_{33}) across different compositions of (1-x)(0.35$BiScO_3$-0.65$PbTiO_3$)-x$Pb(Sc_{1/2}Nb_{1/2})O_3$ ceramics are presented in Table 4.6 as reference.

The observed hysteresis characteristics evident in the P-E loops provide confirmation of the presence of ferroelectric behavior within the (1-x)(0.35$BiScO_3$-0.65$PbTiO_3$)- x$Pb(Sc_{1/2}Nb_{1/2})O_3$ solid solution. The polarization-electric field (P-E) hysteresis loops for all compositions demonstrate well-saturated P-E hysteresis loops, as evidenced in Figure 4.13 (a) - (e) for samples with x values of 0.00, 0.05, 0.10, 0.20 and 0.30. This observation highlights the presence of decent ferroelectricity without any leakage. Furthermore, the remanent polarization (P_r) magnitude experiences a notable increase, reaching 27.4 $\mu C/cm^2$ for the composition with x = 0.10, which is positioned at the morphotropic phase boundary.

Also, the observed trend in the magnitude of coercive field indicates a general reduction with increasing PSN content. This suggests that the disordering of PSN disrupts the ferroelectric dipoles. As the alignment of dipoles becomes less ordered due to the influence of PSN, the coercive field decreases because the dipoles can more easily reorient in response to an external electric field.[86]

The values for the coercive field are quite high comparing to PZT(lead zirconate titanate) with E_C value of 2-3kv/cm in the form of single crystal.[94] Small coercive field can be considered as one of the shortcomings of piezocrystals, which limit their applications demanding operation under high electric field conditions. However, the coercive values in this work indicate the potential applications of these piezoceramics for high field applications.

As mentioned earlier, the poling process is a crucial technique in solid-state chemistry and ceramic fabrication for optimizing the piezoelectric and ferroelectric properties of materials. This process involves applying an electric field to the material at elevated temperatures near its Curie temperature (T_C) and cooling it while maintaining the field. The electric field aids in the alignment of electric dipoles, leading to an enhanced piezoelectric response.[70] Sintered pellets were electroded by a silver paste, then polarized under an electric field close to 30 kV/cm for 120 min in a silicone bath at 150 °C before piezoelectric measurements. All the samples were mechanically stable after poling.

Notably, compositions at the morphotropic phase boundary (MPB) exhibit substantial remanent polarization (P_r) and elevated piezoelectric coefficient (d_{33}) values. The composition containing 10% PSN stands out with a maximum d_{33} value of 625 pC/N, which is notably higher than the d_{33} value of the $0.35BiScO_3$-$0.65PbTiO_3$ end member at 430 pC/N. This significant enhancement in piezoelectric performance within the MPB compositions is likely attributed to heightened polarizability resulting from the interplay between rhombohedral and tetragonal symmetries. This interaction leads to a synergistic effect, promoting equivalent polarization states that effectively reduce energy barriers and facilitate optimal domain reorientation.[95]

Also, the increase in piezoelectric coefficient can be attributed to the effect of addition of PSN to the BS-PT solid solution. PSN is a relaxor material and its addition to the 0.35BS-0.65PT normal ferroelectric solid solution results in increasing the relaxor behaviour. Relaxor-PT ferroelectric materials are known for their high piezoelectric coefficients. When a relaxor is added to a regular ferroelectric material, it can enhance the overall piezoelectric response of the composite material, which allows for a wider range of polarization states and greater flexibility in response to an applied electric field.[55]

The reason for the higher piezoelectric coefficient values in ceramics is attributed to the fact that these compositions fall on the boundary region separating the rhombohedral and monoclinic phases. Ceramic compositions near this phase boundary offer a more favorable path with lower free energy for polarization rotation between the $<111>_c$ and $<001>_c$ orientations in comparison to other compositions. This advantage arises from the distinct symmetry of these compositions, which lowers the energy need to overcome an energy barrier for polarization rotation, unlike compositions with other symmetries.[96]

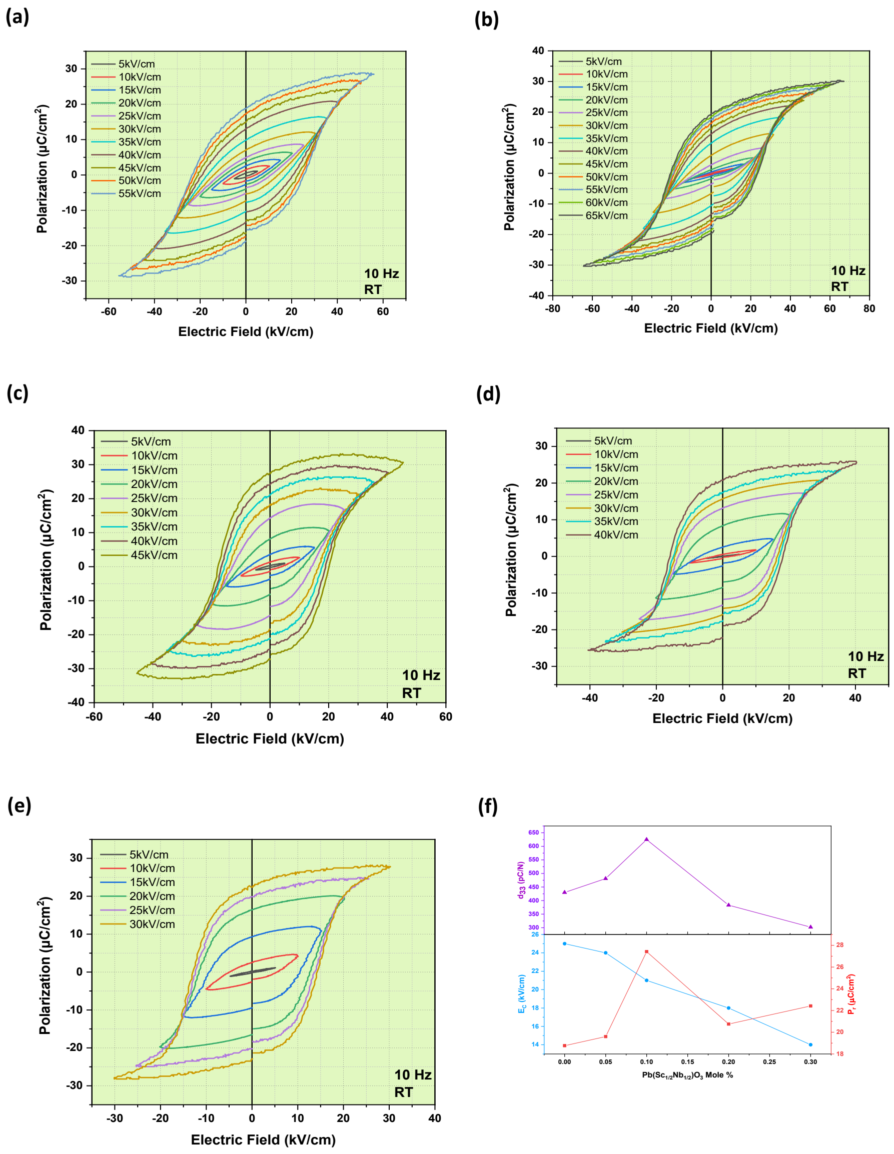

Figure 4.13: Ferroelectric P-E loop of the (1-x)(0.35$BiScO_3$-0.65$PbTiO_3$)-x$Pb(Sc_{1/2}Nb_{1/2})O_3$ solid solution at 10 Hz, recorded at room temperature for the compositions: a) x = 0, b) x = 0.05, c) x = 0.10, d) x = 0.20 and e) x = 0.30; and variation of the coercive field (E_C), remanent polarization (P_r) and piezoelectric coefficient (d_{33}) as a function of $Pb(Sc_{1/2}Nb_{1/2})$ mole content.

Table 4.6: Coercive field (E_C), remanent polarization (P_r) and piezoelectric coefficient (d_{33}) of the (1-x)(0.35$BiScO_3$-0.65$PbTiO_3$)-x$Pb(Sc_{1/2}Nb_{1/2})O_3$ solid solution. E_C and P_r are obtained from the ferroelectric P-E loop measured at room temperature.

x	EC	Pr	d33

	(kV/Cm)	(μC/Cm2)	(pC/N)
0	25	18.76	430±9
0.05	24	19.6	481±11
0.10	21	27.42	625±21
0.20	18	20.75	383±8
0.30	14	22.42	302±18

The polarization-electric field (P-E) hysteresis loop for 0.34BiScO$_3$-0.66PbTiO$_3$ as illustrated in Figure 4.14 (a), does not reach saturation due to the susceptibility of the samples to breakdown when exposed to high electric fields. This susceptibility is likely a consequence of the relatively high conductivity of the 0.34BiScO$_3$-0.66PbTiO$_3$ compound. In contrast, well-saturated P-E hysteresis loops can be observed in Figure 4.14 (b) and Figure 4.14 (c) for compositions with x values of 0.10 and 0.20, indicating robust ferroelectric behavior without any leakage issues. The higher remanent polarization and lower coercive field of composition x = 0.10 illustrates the advantageous effects of incorporating a small amount of PSN into 0.34BiScO$_3$-0.66PbTiO$_3$ in reducing the critical field hence avoiding the dielectric breakdown.

Likewise, the compositions in 0.35BS-0.65PT, a reduction in the coercive field can be observed in the case of 0.34BiScO3-0.66PbTiO3 and 0.36BiScO3-0.64PbTiO3 with an increase in PSN content. Also, a similar pattern in the remanent polarization can be observed by increasing the amount of PSN in both 0.34BiScO3-0.66PbTiO3 and 0.36BiScO3-0.64PbTiO3 solid solutions (Figure 4.15, Table 4.7 and Table 4.8).

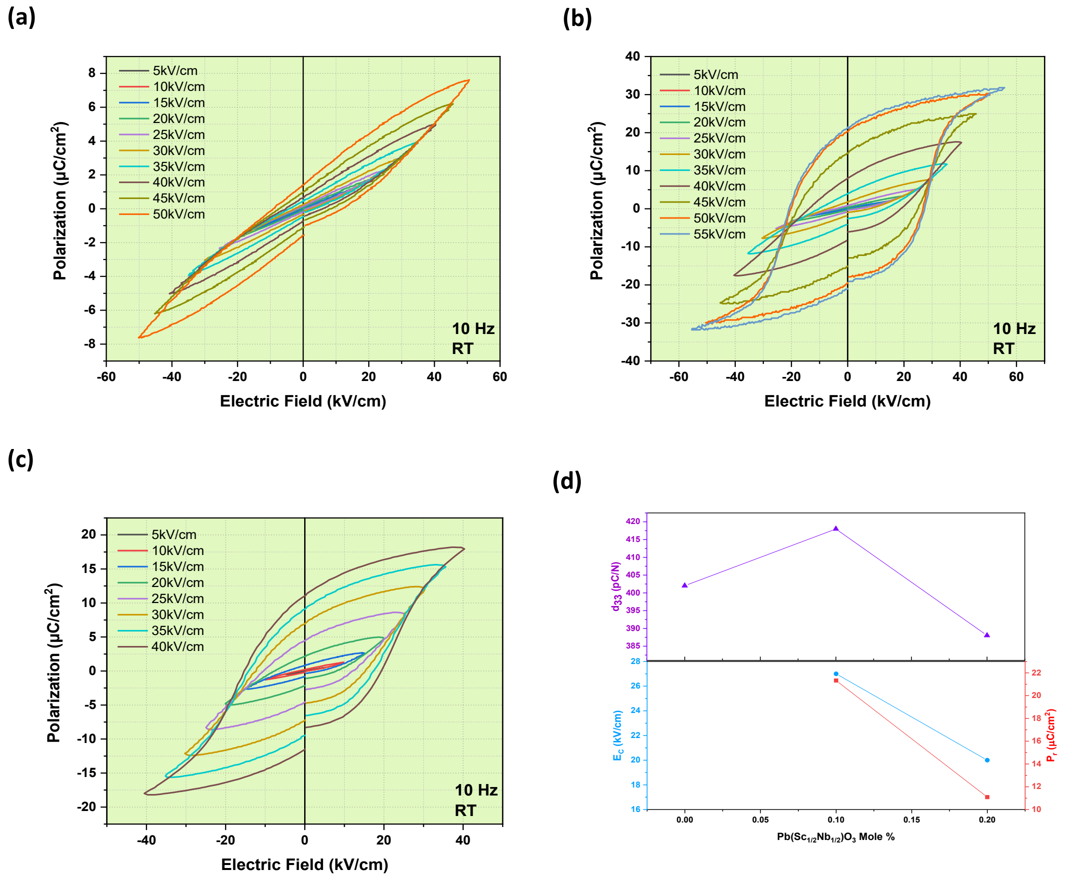

Figure 4.14: Ferroelectric P-E loop of the (1-x)($0.34BiScO_3$-$0.66PbTiO_3$)-x$Pb(Sc_{1/2}Nb_{1/2})O_3$ solid solution at 10 Hz, recorded at room temperature for the compositions: a) x = 0, b) x = 0.10, c) x = 0.20; and d) variation of the coercive field (E_C), remanent polarization (P_r) and piezoelectric coefficient (d_{33}) as a function of x$Pb(Sc_{1/2}Nb_{1/2})O_3$ mole content.

Table 4.7: Coercive Coercive field (E_C), remanent polarization (P_r) and piezoelectric coefficient (d_{33}) of the (1-x)($0.34BiScO_3$-$0.66PbTiO_3$)-x$Pb(Sc_{1/2}Nb_{1/2})O_3$ solid solution. E_C and P_r are obtained from the ferroelectric P-E loop measured at room temperature.

x	E_C (kV/Cm)	P_r (μC/Cm²)	d_{33} (pC/N)
0	/	/	402±6
0.10	27	21.32	418±11
0.20	20	11.09	388±11

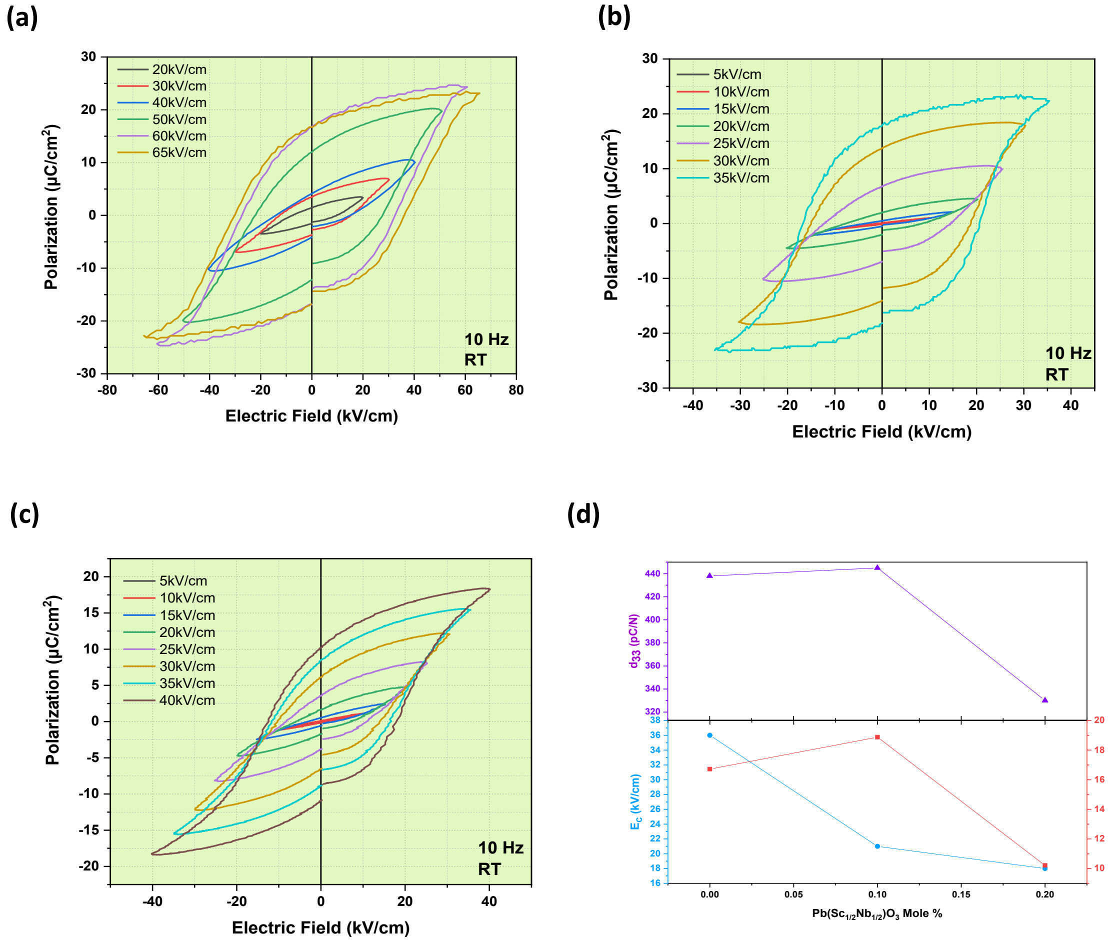

Figure 4.15: Ferroelectric P-E loop of the (1-x)(0.36BiScO$_3$-0.64PbTiO$_3$)-xPb(Sc$_{1/2}$Nb$_{1/2}$)O$_3$ solid solution at 10 Hz, recorded at room temperature for the compositions: a) x=0, b) x = 0.10, c) x = 0.20; and d) variation of the coercive field (E_C), remanent polarization (P_r) and piezoelectric coefficient (d_{33}) as a function of Pb(Sc$_{1/2}$Nb$_{1/2}$)O$_3$ mole content.

Table 4.8: Coercive field (E_C), remanent polarization (P_r) and piezoelectric coefficient (d_{33}) of the (1-x)(0.36BiScO$_3$-0.64PbTiO$_3$)-xPb(Sc$_{1/2}$Nb$_{1/2}$)O$_3$ solid solution. E_C and P_r are obtained from the ferroelectric P-E loop measured at room temperature.

x	E_C (kV/Cm)	P_r (μC/Cm²)	d_{33} (pC/N)
0	36	16.72	438±11
0.10	21	18.88	445±9

0.20	18	10.21	330±4

4.10. Conclusions

In conclusion, the focus of this research is design, synthesis, and characterization of novel ceramic materials, intended for potential applications in high-temperature and high-power electromechanical transduction. To address the issue of conductivity within the conventional high-temperature $BiScO_3$-$PbTiO_3$ binary solid solution system and aim to synthesize a solid solution with higher piezoelectric performance at higher temperatures, a novel pseudo-binary solid solution system, $xPb(Sc_{1/2}Nb_{1/2})O_3$-$yBiScO_3$-$zPbTiO_3$ denoted as xPSN-yBS-zPT, has been successfully developed. This system was synthesized using the solid-state reaction method, resulting in a material with unique properties.

Powder X-ray diffraction and crystal structure refinement reveal a structural transformation driven by composition. There is a phase transition from tetragonal phase to morphotropic phase boundary (MPB) as the combination of tetragonal and rhombohedral phases by increasing the PSN content. Furthermore, the MPB range in $(1-x)(0.35BiScO_3-0.65PbTiO_3)-xPb(Sc_{1/2}Nb_{1/2})O_3$ ($0.05 \leq x < 0.30$) expands compared to the narrow MPB range in $xBiScO_3$-$(1-x)PbTiO_3$ system ($0.34 < x < 0.36$). Microstructural analysis using helium ion microscopy (HIM) demonstrates an increase in grain size followed by a decrease as more PSN is incorporated. This is because the addition of a relaxor component to a ferroelectric material could sometimes inhibit grain growth since relaxor materials tend to have a disordered structure at the nanoscale, which can impede grain growth.

The dielectric measurements of the ceramics were performed across a range of compositions and temperatures. The compositions with varying PSN content show frequency-dependent behavior, indicating the presence of relaxor ferroelectric behavior. Moreover, higher PSN content lead to broader dielectric plots, signifying increased disorder and enhanced relaxor characteristics. High Curie temperatures (T_Cs > 250 °C) are identified for all the compositions. The highest remanent polarization (P_r) recorded at 27.4 μC/cm^2 and high coercive field (E_C) between 21 kV/cm to 27 kV/cm by addition of 10% PSN confirms strong performance in ferroelectric properties.

Additionally, piezoelectric measurement reveals substantial enhancements in the MPB compositions, with the highest d_{33} values reaching 625 pC/N for $0.9(0.35BiScO_3$-$0.65PbTiO_3)$-$0.10Pb(Sc_{1/2}Nb_{1/2})O_3$. This performance is comparable to PZT system but offers the advantages of a higher curie temperature, thereby widening the operational temperature range for potential electromechanical transducer devices. Robust piezo-/ferroelectric properties and stability of the xPSN-yBS-zPT system at high temperatures are offered, marking it as a promising new family of materials for high-temperature and high-power electromechanical applications.

Chapter 5.

Growth and Characterization of Relaxor Ferroelectric $(1\text{-}x)(0.35BiScO_3\text{-}0.65PbTiO_3)\text{-}xPb(Sc_{1/2}Nb_{1/2})O_3$ Crystals

5.1. Abstract

Bismuth-based single crystals with the nominal composition of $0.1Pb(Sc_{1/2}Nb_{1/2})O_3$-$0.315BiScO_3$-$0.585PbTiO_3$ (0.1PSN-0.315BS-0.585PT) ternary complex perovskite system were successfully grown using a high-temperature solution growth (HTSG) method. A mixture of PbO and Bi_2O_3 in a molar ratio of 73:27 was used as flux, and the flux to charge ratio was optimized to be 70:30 (wt%). The grown crystals, with dimensions up to 3 mm, exhibit a pseudo-cubic morphology. The XRD patterns of the ground powder and naturally formed pseudo-cubic facets confirm that the grown single crystals crystallize in the perovskite structure with the rhombohedral symmetry as the major phase, and the naturally grown pseudo-cubic facets are parallel to $\{100\}_C$. Polarized light microscopy (PLM) examination reveals a band-like domain structure in the (001)-oriented crystal plate, which undergoes a phase transition to a cubic phase at T_C = 410°C indicating a high curie temperature. Detailed analysis of the domain structure demonstrates the coexistence of rhombohedral, tetragonal and monoclinic phases, thereby indicating the morphotropic phase boundary (MPB) characteristics. The ferroelectric properties are displayed by polarization-electric field (P-E) hysteresis loops with a remanent polarization of 17 $\mu C/cm^2$ and a high coercive field of 68 kV/cm. The piezoelectric coefficient (d_{33}) is found to be 478 pC/N. The high Curie temperature and decent piezo- and ferroelectric performance of the PSN-BS-PT crystals make this ternary complex perovskite system a promising candidate for potential applications in high-temperature and high-power electromechanical transduction.

5.2. Introduction

Piezo- and ferroelectric materials are incredibly valuable for a wide range of applications in various devices such as sensors, actuators, energy harvesters, transducers, ultrasonic motors, and other electromechanical systems.[7,9,66,70] In recent years, there has been an increasing demand for these materials to perform effectively in a wide temperature range and in the presence of varying electric field strengths. This demand arises from such critical areas as fuel regulation in combustion engines, nuclear reactor monitoring, deep-sea oil drilling, therapeutic applications, underwater transducers, and the health monitoring of aircraft turbine systems.[68,69,97] The ever-expanding scope of these applications underscores the pressing need to develop advanced piezo- and ferroelectric materials that can adapt to the evolving demands of modern technology.

$Pb(Zr, Ti)O_3$ (PZT) has long been a top choice for piezo- and ferroelectric ceramics in various industries due to its exceptional properties. The most studied and used PZT compositions typically contain a mixture of tetragonal, rhombohedral and monoclinic phases, known as the morphotropic phase boundary (MPB). However, to tailor them for specific applications, dopants are commonly added to PZT ceramics inducing “soft” (doner dopants with higher valency) or “hard” (acceptor dopants with lower valency) piezoelectric behavior. Soft PZT ceramics usually shows T_C in 200-300 °C and higher piezoelectric behavior (d_{33} in 600-800 pC/N) suitable for sensor and actuator applications. On the other hand, hard PZT ceramics stand out for a relatively high Curie temperature, around 350 °C, with their piezoelectric coefficient typically ranging from 200 to 400 pC/N, particularly suitable for ultrasonic motor applications.[73,74,98] PZT-related materials suffer from depolarization and aging issues within 200 °C, making them unsuitable for high-temperature applications, like deep drilling for oil and engine turbine monitoring where temperatures can reach well over 300 °C.[2,99]

Newly developed piezocrystals based on relaxor materials, like $Pb(Mg_{1/3}Nb_{2/3})O_3$-$PbTiO_3$ (PMN-PT) and $Pb(Zn_{1/3}Nb_{2/3})O_3$-$PbTiO_3$ (PZN-PT), have shown impressive improvements in piezoelectric performance compared to the traditional PZT ceramics. These materials can produce much higher piezoelectric responses, with the piezoelectric coefficient (d_{33}) ranging from 1500 to 4100 pC/N.[30,32,100] However, PMN-PT and PZN-PT crystals or ceramics can only be effectively used around room temperature due to their low Curie temperatures (T_C is less than 200 °C) and even lower morphotropic phase boundary temperatures (T_{MPB} is less than 100 °C). Additionally, they have a low coercive field (E_C is less than 3 kV/cm), which makes them unsuitable for high-power electromechanical applications.[30]

In search for high-T_C piezoelectrics, bismuth-containing systems have attracted new attention. Among various $BiMeO_3$-$PbTiO_3$ solid solutions developed, $BiScO_3$-PbTiO (BS-PT) stands out for its good piezoelectric performance (d_{33}>350 pC/N) and high Curie temperatures (T_C > 400°C), particularly for its morphotropic phase boundary (MPB) compositions.[77,78] However, there is a notable challenge with these compounds: they tend to become highly conductive, especially at high temperatures, which limits their effective operating temperature range. Another constraint is that $BiScO_3$ can only form solid solutions with $PbTiO_3$ with a maximum concentration of 40%, and the MPB region in this system covers a relatively narrow compositional range of 34-36% $BiScO_3$.[75] Moreover, it is difficult to grow Bi-based complex perovskite single crystals.

In our efforts to develop new piezo-/ferroelectric materials with high T_C and high performance, this work is centered at the growth, structural analysis, and characterization of xPSN-(1-x)[$(BS)_{0.35}(PT)_{0.65}$] perovskite solid solution single crystals. This novel solid solution had been recently developed in the form of ceramics in our laboratory. It demonstrates promising piezo- and ferroelectric performance. However, single crystals of this material had not been grown or studied. In this work, 0.1PSN-0.9[$(BS)_{0.35}(PT)_{0.65}$] single crystals are successfully grown using a high-temperature solution growth (HTSG) method. The grown crystals are analyzed by X-ray diffraction, and polarized light microscopy (PLM), and investigated for their ferroelectric and piezoelectric properties, domain structure, phase components, and phase transition.

The grown ternary crystals are found to exhibit remarkable properties: a high Curie temperature (T_C = 410 °C), a decent piezoelectricity (d_{33} = 478 pC/N), and a high remanent polarization (P_r = 17 μC/cm^2) with a substantial coercive field (E_C = 68 kV/cm). These properties outperform those reported in other Bi-containing perovskite solid solution single crystals, such as $Bi(Zn_{2/3}Nb_{1/3})O_3$-$PbTiO_3$ (30BZN-70PT) and $Bi(Zn_{2/3}Ta_{1/3})O_3$-$PbTiO_3$ (20BZTa-80PT), making the PSN-BS-PT crystals an interesting piezocrystal resource for potential applications under harsh conditions.[36,101]

5.3. Single Crystal Growth

For the growth of single crystals with the nominal composition of $0.1Pb(Sc_{1/2}Nb_{1/2})O_3$-$0.315BiScO_3$-$0.585PbTiO_3$ (0.1PSN-0.315BS-0.585PT) single crystals, high-purity powders of scandium oxide (Sc_2O_3, 99.9%, Aldrich), bismuth oxide

(Bi_2O_3, 99.9%, Alpha Aesar), niobium oxide (Nb_2O_5, 99.9%, Alfa Aesar), lead oxide (PbO, 99.9%, Alfa Aesar), and titanium oxide (TiO_2, 99.5%, Alfa Aesar) were accurately weighed in stoichiometric amounts, thoroughly mixed and hand-ground for 2 hours. The growth of single crystal was carried out using the high-temperature solution growth (HTSG) method. To lower the melting point and reduce high-temperature evaporation of the system, a complex mixture of 73 mole % PbO and 27 mole % Bi_2O_3 was employed as flux which provids good solubilities for the constituent oxides. Given the considerably high melting point of Sc_2O_3 (T_m = 2485°C), a relatively high ratio of 70 to 30 (wt%) of flux to solute was utilized for growing the PSN-BS-PT single crystals. In the growth procedure, the well-mixed powders of solute and flux were first loaded into a 50 ml platinum crucible. This platinum crucible was then placed inside a larger alumina (Al_2O_3) crucible, which was sealed with an alumina lid using alumina cement to prevent the evaporation of the high-temperature solution. Subsequently, this double crucible setup was positioned within a covered furnace chamber. A sketch of the furnace and crucible assembly and a real picture of the furnace and ventilation system are provided in Figure 5.1.

As outlined in the thermal profile presented in Figure 5.2, the solute-flux mixture was initially heated up to 1180°C, held at this temperature for 24 hours to ensure the complete dissolution of the solute within the flux. Following this, the mixture was first cooled at a rate of 5 °C per hour, bringing it closer to the estimated liquid line of the solute-flux phase diagram. Subsequently, the high-temperature solution was cooled down at a slower rate of 2 °C per hour, a crucial step when reaching the supersaturation to prompt the spontaneous nucleation and crystal growth. This growth process continued until the temperature reached 850 °C. From there on, it was cooled at a faster rate of 50 °C per hour down to room temperature. The platinum crucible with the grown crystals embedded in solidified flux was then taken out. To retrieve the as-grown single crystals, the crucible underwent a leaching process with a 20% nitric acid solution, conducted at room temperature of 27 °C, which lasted for 5 to 7 days.

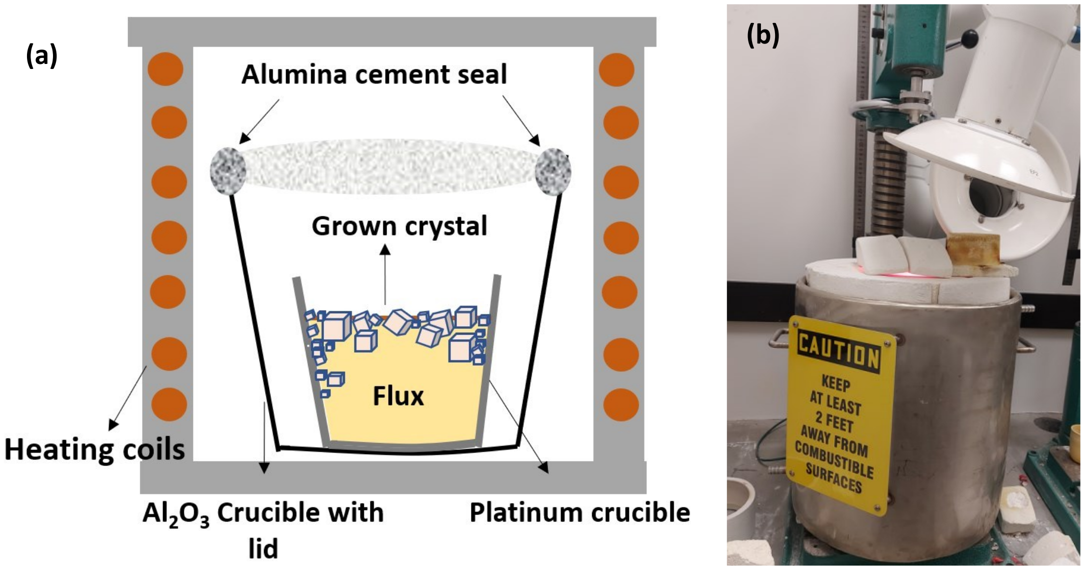

Figure 5.1: **(a) Schematic illustrating the furnace and crucible assembly utilized in the high-temperature solution growth (HTSG) process for the growth of $0.1Pb(Sc_{1/2}Nb_{1/2})O_3$-$0.315BiScO_3$-$0.585PbTiO_3$ crystals; (b) Real picture of the furnace set up and ventilation system.**

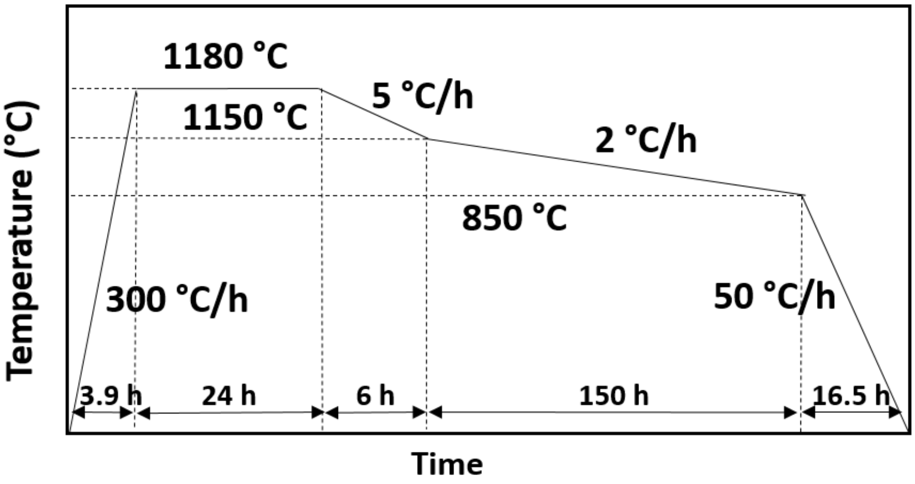

Figure 5.2: **Thermal profile consisting of heating, dwelling, and cooling at variable rates used for the growth of crystals with the nominal composition of $0.1Pb(Sc_{1/2}Nb_{1/2})O_3$-$0.315BiScO_3$-$0.585PbTiO_3$ crystals by high-temperature solution growth (HTSG) method.**

5.4. Growth Result, Crystal Morphology, and Structural Analysis

Figure 5.3 shows the results of a growth batch. The crystals with the nominal composition of $0.1Pb(Sc_{1/2}Nb_{1/2})O_3$-$0.315BiScO_3$-$0.585PbTiO_3$ were formed on the surface and inside solidified flux (Figure 5.3 (a-c)). The as-grown crystals exhibit a yellowish color and have the typical dimensions of 2 mm × 2 mm × 2 mm, with the largest ones reaching 3 mm in size. Notably, well-defined 90° angles along the edges and flat surfaces, exhibiting naturally developed pseudo-cubic morphology, which is the result of a nearly complete growth of the $\{100\}_C$ facets. These facets exhibit a slower growth rate compared to other major facets like $\{110\}_C$ and $\{111\}_C$, giving rise to the pseudo-cubic shape.

The key factor determining crystal morphology lies in the relative growth rates of various crystal faces[100]. The faces with slower growth rates hold more significant morphological importance. As illustrated in Figure 5.3 (b), the surface microstructure of some as-grown crystals exhibits diagonal lines cutting through the crystal center, which is indicative of growth sectors resulting from a pyramidal growth mechanism, ultimately giving rise to the observed pseudo-cubic crystal morphology. Optical microscopy reveals that the as-leached crystals are notably translucent, suggesting a minimal presence of defects and/or inclusions formed during growth. The high quality of the crystals greatly facilitates the subsequent examinations of their domain structure, phase components and phase transitions using polarized light microscopy (PLM).

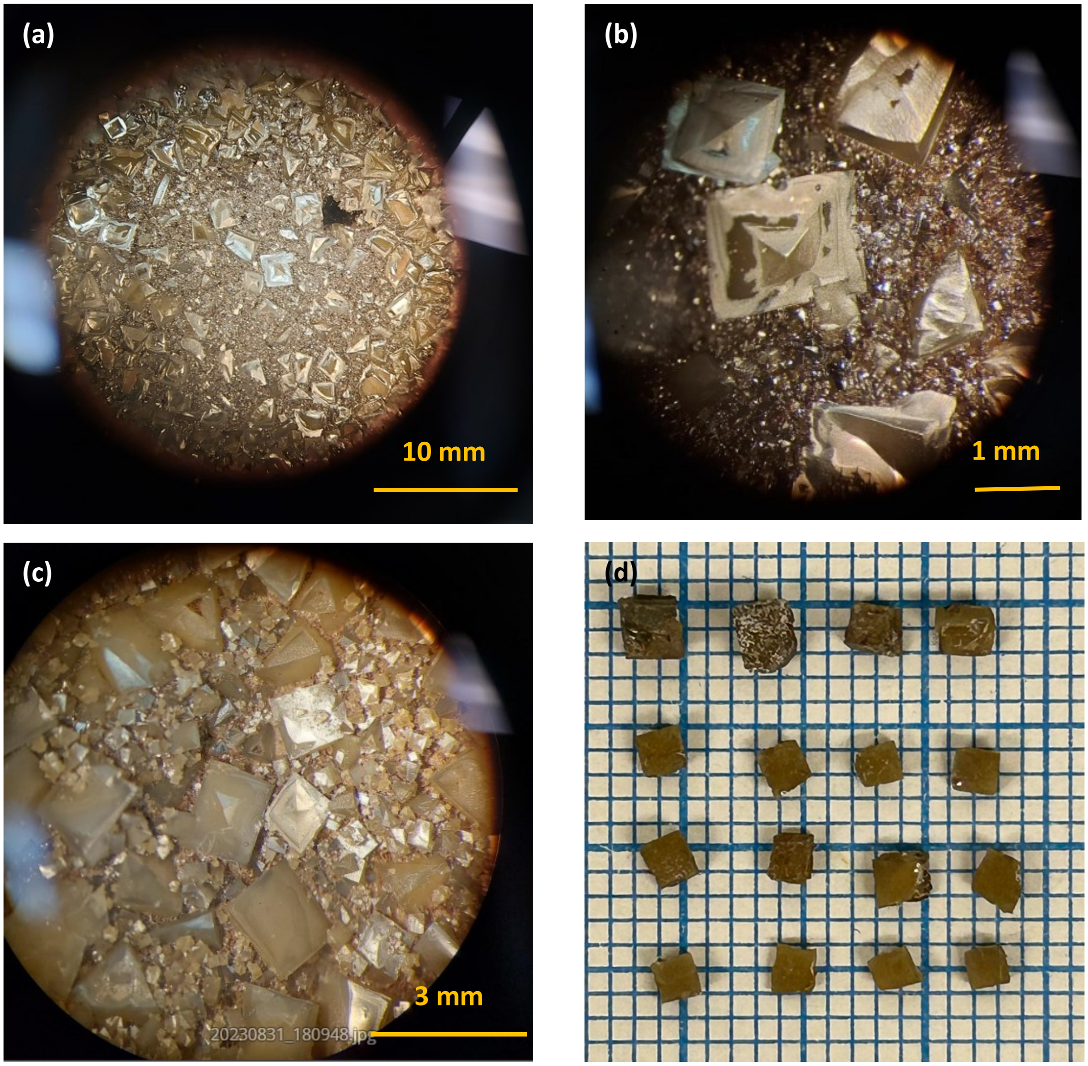

Figure 5.3: **Optical images of as-grown single crystals with a nominal composition of $0.1Pb(Sc_{1/2}Nb_{1/2})O_3$-$0.315BiScO_3$-$0.585PbTiO_3$: (a) Crystals formed on the surface of solidified flux in the crucible after cooling; (b) Enlarged view of selected single crystals formed inside the flux that display growth striation; (c) Crystals grown in the middle of the flux that are revealed after leaching in 20% nitric acid for 60 minutes; (d) Selected crystals after leaching with pseudo-cubic morphology.**

Figure 5.4 displays the XRD patterns of $0.1Pb(Sc_{1/2}Nb_{1/2})O_3$-$0.315BiScO_3$-$0.585PbTiO_3$ in the forms of both ground powder and as-grown single crystal. The powder XRD pattern (Figure 5.4 (a)), in comparison with the standard $Pb(Sc_{1/2}Nb_{1/2})O_3$ file, confirms that the grown single crystals crystallize in the perovskite structure with a rhombohedral symmetry being the dominant phase. Figure 5.4 (b) shows the XRD pattern of one of the pseudo-cubic facets of an as-grown PSN-BS-PT single crystal. The only $\{h00\}_C$ ($\{100\}$, $\{200\}$ and $\{300\}$) peaks confirms the naturally grown facets are parallel to $\{100\}_C$. The rhombohedral lattice parameter 'a_R' of crystals is calculated to be 4.005 Å by using the Bragg's law.

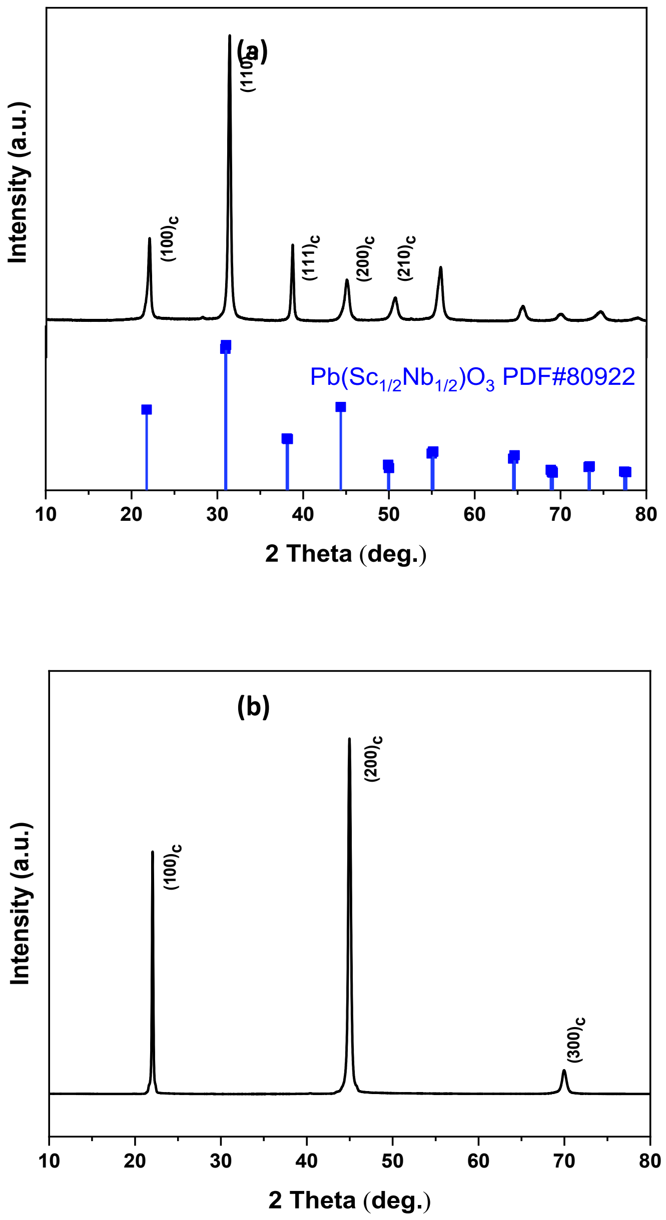

Figure 5.4: X-ray diffraction (XRD) patterns obtained from: (a) Ground powder; (b) One of the naturally grown pseudo-cubic facets, of the $0.1Pb(Sc_{1/2}Nb_{1/2})O_3$-$0.315BiScO_3$-$0.585PbTiO_3$ single crystals.

5.5. Optical Domain Structure, Phase Symmetry and Phase Transition

The domain structures, phase symmetries and phase transitions of the PSN-BS-PT crystal platelets were examined based on the principles of optical crystallography. For this purpose, an Olympus BX60 PLM equipped with a Linkam HTMS600 heating/cooling stage was employed. Figure 5.5, shows the images of a $(001)_{cub}$ platelet (thickness = 73 μm) observed under different orientations of crossed polarizers. Regions 1 (Figure 5.5 (a)) of the platelet exhibits extinction when the crossed polarizers are set at 45° relative to the $[100]_{cub}$ direction, indicating a rhombohedral symmetry. An intermediate extinction was observed at 90° ± 21° in Regions 2 (Figure 5.5 (b)), suggesting the presence of a monoclinic phase. In Regions 3 (Figure 5.5 (c)), extinctions parallel to [100] and domain walls along [110] direction are found, which align with a tetragonal symmetry. Based on the PLM results, rhombohedral appears to be the major phase, with the coexistence of the monoclinic phase in some areas and the tetragonal phase on the edge. The color fringes appearing in the rhombohedral and monoclinic areas arise from the inclined domain walls. Therefore, the PSN-BS-PT single crystals demonstrate a coexistence of rhombohedral, monoclinic and tetragonal phases, which is characteristic of morphotropic phase boundary (MPB) behavior, as observed in several other solid solution systems.[66,98,102]

Figure 5.6 shows the variation of domain structures as a function of temperature from room temperature up to 460 °C. Upon heating, the color fringes of the domains becoming less vivid arising from the decrease of birefringence, which occurs more sharply around 370 °C. However, the birefringence of the rhombohedral and monoclinic domains does not vanish until T_C = 410 °C, which corresponds to the transition temperature into the high-temperature cubic phase. Interestingly, the domain walls and birefringence of the tetragonal phase subsist until T_C = 460 °C when it transforms into the cubic phase. The higher T_C observed in the tetragonal phase could be accounted for the effect of composition segregation in the PSN-BS-PT system. The concentration of PT of BS-PT in the crystals could increase as the temperature decrease in the late stage of the growth process, leading to a higher T_C. This clarifies the sequential formation of the rhombohedral and monoclinic phases followed by the tetragonal phase.[103]

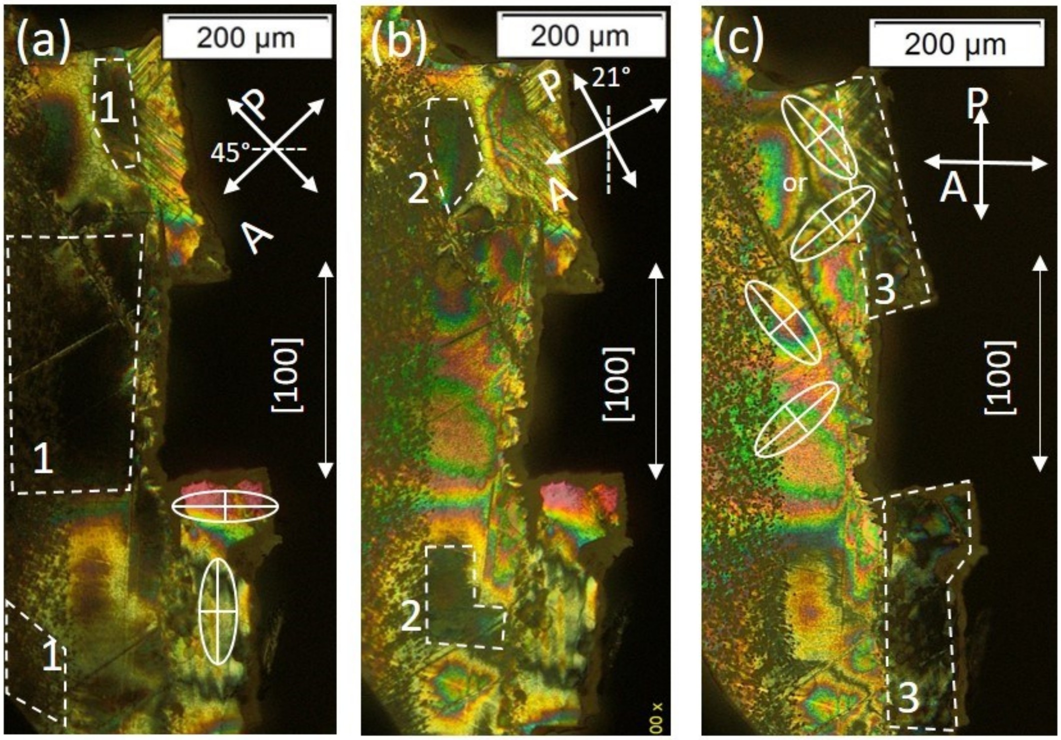

Figure 5.5: Domain structure of a $(001)_{cub}$ platelet of the PSN-BS-PTR single crystal observed by polarized light microscopy (PLM) at room temperature: a) Diagonal extinctions in Region 1, corresponding to the rhombohedral phase; b) Intermediate extinctions at 90° ± 21°, indicating the monoclinic symmetry in Regions 2; c) Parallel extinctions in Regions 3, suggesting the tetragonal symmetry.

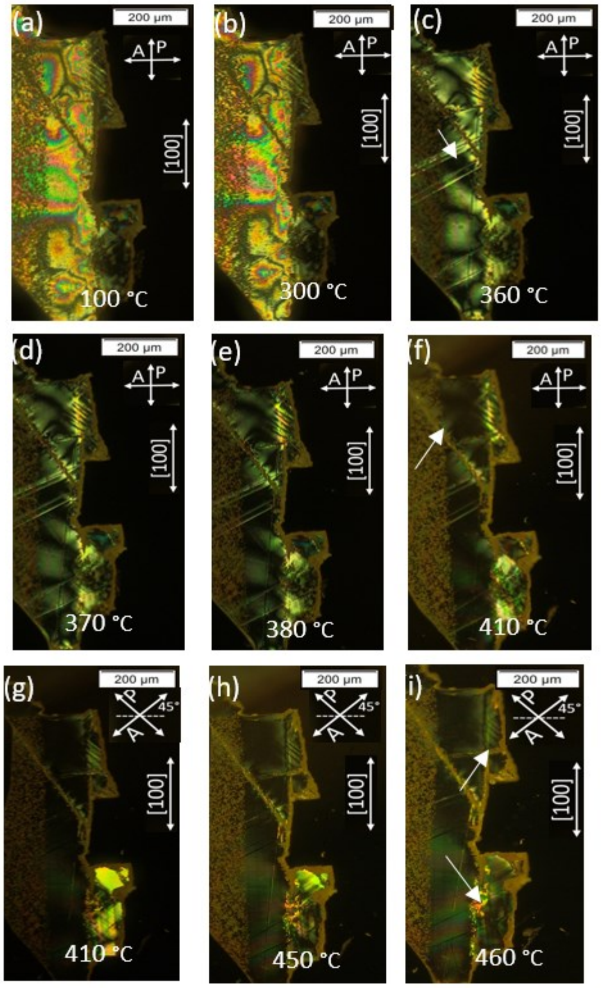

Figure 5.6: **Variations of domain structure of the $(001)_{cub}$ platelet showing phase transitions of the birefringent rhombohedral, monoclinic and tetragonal symmetries to the high temperature isotropic cubic phase.**

5.6. Ferroelectric and Piezoelectric Properties

Silver paste was painted on the $(001)_{cub}$ surfaces of polished single crystals as electrodes for ferroelectric and piezoelectric measurements, using a Radiant RT66A standard ferroelectric testing system and a piezo d_{33}/d_{31} meter (Model ZJ-6B), respectively. Figure 5.7 presents the polarization-electric field (P-E) hysteresis loops of the crystal displayed at room temperature. The loops reveal the ferroelectric characteristic when sample is subjected to electric fields up to 170 kV/cm. Notably, the coercive field (E_C) for this crystal is 68 kV/cm, significantly higher than those observed in relaxor-based piezo-/ferroelectric single crystal systems like PMN-PT and PZN-PT, where E_C typically remains below 5 kV/cm.[104,105] This high coercive field in the PSN-BS-PT crystal system underscores its superior and more enduring ferroelectric behavior, useful for the potential applications of these crystals in high-power transducers. The remanent polarization of the PSN-BS-PT crystal is found to be approximately 17 μC/cm², further substantiating its strong ferroelectric nature. The high coercive field and large polarization are two crucial indicators of the material's ability to retain the remanent electric polarization after the removal of an applied electric field. To reveal their optimum piezoelectric properties, the crystals need to be poled. The poling process involved applying an electric field to the crystal at an elevated temperature near its Curie temperature (T_C), followed by cooling down to room temperature while maintaining the field. The electric field aids in the alignment of electric dipoles, leading to an enhanced piezoelectric response. The $(001)_{cub}$ oriented crystals were electroded by silver paste, then poled under an electric field of 35 kV/cm in a silicone bath at 150 °C for 120 min, and cooled down before the piezoelectric measurements. The piezoelectric coefficient d_{33}, a measure of the polarization developed along $[001]_c$ in response to a mechanical stress applied along the same direction, is determined to be 478 pC/N. This significant piezoelectric performance within the MPB compositions could be attributed to the interplay between the polarization components of the rhombohedral, tetragonal and monoclinic symmetries.[98,102] This interaction leads to a synergistic effect, promoting multiple polarization states that effectively reduce energy barriers and facilitate optimal domain reorientation, making the crystal more electromechanically active. Thus, like in other solid solution systems with MPB compositions, the PSN-BS-PT crystals with multiple phase components offer a more favorable path with lower free energies for polarization rotations toward $<001>_c$ direction under the electric field, giving rise to a very good piezoelectricity with a relatively high T_C.

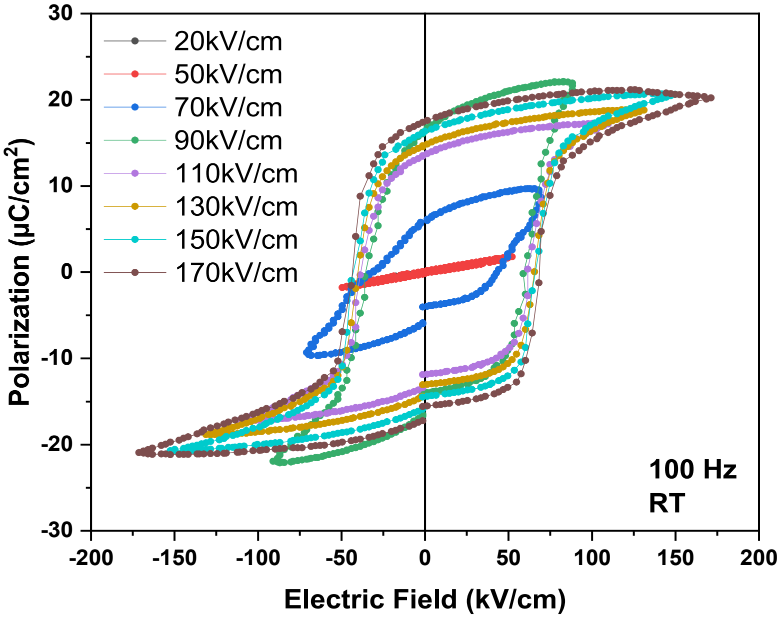

Figure 5.7: Polarization-electric field (P-E) loops of the single crystals with nominal composition of 0.1Pb($Sc_{1/2}Nb_{1/2}$)O_3-0.315BiScO_3-0.585PbTiO_3 measured at the frequency of 100 Hz at room temperature, under various field strengths from 20 kV/cm up to 170 kV/cm, demonstrating good ferroelectricity.

5.7. Conclusions

In this work, single crystals of the ternary complex perovskite system of 0.1Pb($Sc_{1/2}Nb_{1/2}$)O_3-0.315BiScO_3-0.585PbTiO_3 (0.1PSN-0.315BS-0.585PT) were successfully grown using the high-temperature solution growth (HTSG) method. The grown crystals, with dimensions up to 3mm, exhibit a pseudo-cubic morphology with a good quality. The XRD patterns of the ground powder and naturally formed pseudo-cubic facets confirm that the grown single crystals crystallize in the perovskite structure, and the naturally grown facets are parallel to $\{100\}_C$. Upon heating, phase transition from the rhombohedral and monoclinic to the cubic phase take place at T_C = 410 ℃, while the tetragonal phase transforms into cubic phase at a higher T_C of 460 ℃, which suggests a higher concentration of PT of BS-PT in it, resulting from composition segregation. The domain structures in the (001)-oriented single crystals examined by polarized light microscopy (PLM) and optical crystallography revealed the coexistence of rhombohedral, monoclinic and tetragonal phases, with the development of the tetragonal phase likely occurring at the late stage of the growth, demonstrating the morphotropic phase boundary (MPB) characteristics for the grown crystals. The crystals are proved to be ferroelectric with a remanent polarization of 17 μC/cm^2 and a high coercive field of 68 kV/cm. The piezoelectric coefficient (d_{33}) is measured to be 478 pC/N. The good piezo- and ferroelectric properties, and the high T_C of the PSN-BS-PT ternary crystals make them promising materials for high temperature electromechanical transduction applications.

Chapter 6.

Conclusions

This thesis work focuses on developing new piezo-/ferroelectric materials with improved performance and enhanced relaxor behavior, making them ideal for a range of applications, in particular at high temperatures.

In the first part of the thesis, a new bismuth-based solid solution of $(1-x)Pb(Sc_{1/2}Nb_{1/2})O_3$-$xBiScO_3$ is synthesized. The study includes determination of solubility limit, crystal structure analysis, ceramic microstructure imaging, and the characterization of physical properties, such as dielectric, ferroelectric, and piezoelectric properties. The study shows that the substitution of $BiScO_3$ for $Pb(Sc_{1/2}Nb_{1/2})O_3$ induces a crossover from the ferroelectric phase to a relaxor state. As a representative composition of this solid solution, $0.90Pb(Sc_{1/2}Nb_{1/2})O_3$-$0.10BiScO_3$ exhibits a high saturation polarizations ($P_S = 21.45$ μC/cm^2), a moderate piezoelectric performance ($d_{33} = 32$ pC/N), and a low remanent polarization ($P_r = 2.62$ μC/cm^2) values, characteristic of relaxor ferroelectrics, making it potentially useful for energy storage and electromechanical transduction applications.

The second part of the thesis is to develop a novel ternary solid solution by combining $Pb(Sc_{1/2}Nb_{1/2})O_3$ and $BiScO_3$-$PbTiO_3$ solid solution. Different compositions of $xPSN-(1-x)[(BS)_{0.34}(PT)_{0.66}]$, $xPSN-(1-x)[(BS)_{0.35}(PT)_{0.65}]$, and $xPSN-(1-x)[(BS)_{0.36}(PT)_{0.64}]$ ternary solid solutions has been successfully synthesized, exhibiting compositionally driven phase transitions from tetragonal to morphotropic phase boundary (MPB) as combination of tetragonal and rhombohedral phases. Notably, the MPB region in PSN-BS-PT is more extended than the $BiScO_3$-$PbTiO_3$ (BS-PT) solid solution. Also, PSN-BS-PT shows higher Curie temperatures (T_C) comparing to traditional $Pb(Zr,Ti)O_3$ (PZT). The temperature-dependent behavior of the dielectric constant in the studied compositions exhibits characteristic features of relaxor ferroelectric materials with increasing amount of PSN. Furthermore, the frequency-dependent behavior of the temperature at which the maximum permittivity occurs adheres to the Vogel-Fulcher law. Excellent piezo-/ferroelectric performance as well as high T_C is achieved for the composition of $0.9(0.35BiScO_3$-$0.65PbTiO_3)$-$0.10Pb(Sc_{1/2}Nb_{1/2})O_3$: $d_{33} = 625$ pC/N, $P_r =$

27.42 μC/cm^2 , E_C = 21 kV/cm, and T_C = 363 °C. The results show that 10% substitution of $Pb(Sc_{1/2}Nb_{1/2})O_3$ for BS-PT increases the grain size by 98%, the remanent polarization (P_r) by 46%, and the piezoelectric coefficient (d_{33}) by 45%, which represents a significant improvement of the ferroelectric and piezoelectric performance.

In the final part of the thesis, bismuth-based single crystals of the $0.1Pb(Sc_{1/2}Nb_{1/2})O_3$-$0.315BiScO_3$-$0.585PbTiO_3$ (0.1PSN-0.315BS-0.585PT) ternary complex perovskite system were successfully grown using a high-temperature solution growth (HTSG) method. The XRD patterns of the ground powder and naturally formed pseudo-cubic facets confirm that the grown single crystals crystallize in the perovskite structure with the rhombohedral symmetry as the major phase, and the naturally grown pseudo-cubic facets are parallel to $\{100\}_C$. Polarized light microscopy (PLM) examination reveals a band-like domain structure in the (001)-oriented crystal plate, which undergoes a phase transition to a cubic phase at T_C = 410°C indicating a high curie temperature. Detailed analysis of the domain structure demonstrates the coexistence of rhombohedral, tetragonal and monoclinic phases, thereby indicating the morphotropic phase boundary (MPB) characteristics. The ferroelectric properties are displayed by polarization-electric field (P-E) hysteresis loops with a remanent polarization of 17 μC/cm^2 and a high coercive field of 68 kV/cm. The piezoelectric coefficient (d_{33}) is found to be 478 pC/N. The high Curie temperature and decent piezo- and ferroelectric performance of the PSN-BS-PT crystals make this ternary complex perovskite system a promising candidate for potential applications in high-temperature and high-power electromechanical transduction.

Figure 6.1 illustrates the piezoelectric coefficient (d_{33}) of the ceramic and single crystal of $0.1Pb(Sc_{1/2}Nb_{1/2})O_3$-$0.315BiScO_3$-$0.585PbTiO_3$ synthesized in this study and other existing piezo-/ferroelectric perovskite materials concerning their Curie temperatures. The bismuth-based single crystal of the $0.1Pb(Sc_{1/2}Nb_{1/2})O_3$-$0.315BiScO_3$-$0.585PbTiO_3$ (0.1PSN-0.315BS-0.585PT) with T_C = 410 °C and d_{33} = 478 pC/N and the ceramics with T_C = 363 °C and d_{33} = 625 pC/N have demonstrated elevated Curie temperature as well as decent piezoelectric coefficient. As a result, these materials present themselves as potential candidates for advanced high-temperature and high-performance applications.

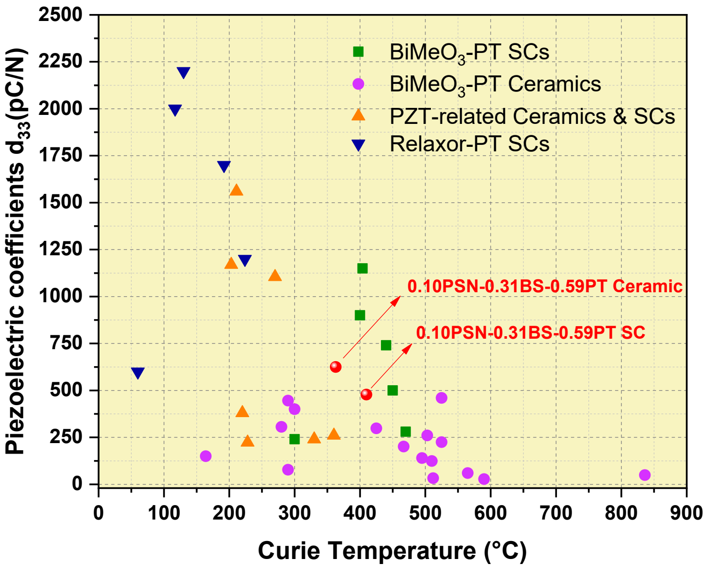

Figure 6.1: **Variations in the piezoelectric coefficient (d_{33}) concerning the Curie temperature (T_C) across different perovskite materials.**

References

1. Curie, J. & Curie, P. Développement par compression de l'électricité polaire dans les cristaux hémièdres à faces inclinées. *Bulletin de Minéralogie* **3**, 90–93 (1880).
2. Jaffe, H. Piezoelectric Ceramics. *Journal of the American Ceramic Society* **41**, 494–498 (1958).
3. Nye, J. F. *Physical properties of crystals: their representation by tensors and matrices*. (Oxford university press, 1985).
4. Damjanovic, D. Ferroelectric, dielectric and piezoelectric properties of ferroelectric thin films and ceramics. *Reports on progress in physics* **61**, 1267 (1998).
5. Tagantsev, A. & Gerra, G. Interface-Induced Phenomena in Polarization Response of Ferroelectric Thin Films. *Journal of Applied Physics* **100**, (2006).
6. Li, F. & Zhang, S. Decoding the Fingerprint of Ferroelectric Loops: Comprehension of the Material Properties and Structures. *Journal of the American Ceramic Society* **97**, 1–27 (2014).
7. Lines, M. E. & Glass, A. M. *Principles and Applications of Ferroelectrics and Related Materials*. (Oxford University Press, 2001).
8. Cross, L. E. Relaxor ferroelectrics. *Ferroelectrics* **76**, 241–267 (1987).
9. Manjón-Sanz, A. M. & Dolgos, M. R. Applications of Piezoelectrics: Old and New. *Chem. Mater.* **30**, 8718–8726 (2018).
10. Wang, T., Li, Y., Zhang, X., Zhang, D. & Gong, W. Simultaneous excellent energy storage density and efficiency under applied low electric field for high entropy relaxor ferroelectric ceramics. *Materials Research Bulletin* **157**, 112024 (2023).
11. Covaci, C. & Gontean, A. Piezoelectric Energy Harvesting Solutions: A Review. *Sensors* **20**, 3512 (2020).

12. Noheda, B. *et al.* Stability of the monoclinic phase in the ferroelectric perovskite. *Phys. Rev. B* **63**, 014103 (2000).
13. Bokov, A. & Ye, Z.-G. Dielectric Dispersion and Critical Behavior in Relaxor Ferroelectric $Pb(Mg_{1/3}Nb_{2/3})O_3$ – $PbTiO_3$. *Applied Physics Letters* **77**, 1888–1890 (2000).
14. Viehland, D., Jang, S. J., Cross, L. E. & Wuttig, M. Freezing of the polarization fluctuations in lead magnesium niobate relaxors. *Journal of Applied Physics* **68**, 2916–2921 (1990).
15. Bokov, A. A. & Ye, Z.-G. Universal relaxor polarization in $Pb(Mg_{1/3}Nb_{2/3})O_3$ and related materials. *Phys. Rev. B* **66**, 064103 (2002).
16. Bokov, A. A. & Ye, Z.-G. Recent progress in relaxor ferroelectrics with perovskite structure. *J Mater Sci* **41**, 31–52 (2006).
17. Ahn, C. *et al.* A brief review on relaxor ferroelectrics and selected issues in lead-free relaxors. *Journal of the Korean Physical Society* **68**, 1481–1494 (2016).
18. Bing, Y.-H. & Ye, Z.-G. Effects of chemical compositions on the growth of relaxor ferroelectric $Pb(Sc_{1/2}Nb_{1/2})_{1-x}Ti_xO_3$ single crystals. *Journal of Crystal Growth* **250**, 118–125 (2003).
19. Bokov, A. A. & Ye, Z.-G. DIELECTRIC RELAXATION IN RELAXOR FERROELECTRICS. *J. Adv. Dielect.* **02**, 1241010 (2012).
20. Valasek, J. Piezo-Electric and Allied Phenomena in Rochelle Salt. *Phys. Rev.* **17**, 475–481 (1921).
21. Valasek, J. Properties of Rochelle Salt Related to the Piezo-electric Effect. *Phys. Rev.* **20**, 639–664 (1922).
22. Berlincourt, D. & Jaffe, H. Elastic and Piezoelectric Coefficients of Single-Crystal Barium Titanate. *Phys. Rev.* **111**, 143–148 (1958).

23. Jaffe, B., Roth, R. S. & Marzullo, S. Piezoelectric Properties of Lead Zirconate-Lead Titanate Solid-Solution Ceramics. *Journal of Applied Physics* **25**, 809–810 (1954).
24. Jaffe, B., Roth, R. S. & Marzullo, S. Properties of piezoelectric ceramics in the solid-solution series lead titanate-lead zirconate-lead oxide: tin oxide and lead titanate-lead hafnate. *Journal of research of the National Bureau of Standards* **55**, 239–254 (1955).
25. Newnham, R. E., Skinner, D. P. & Cross, L. E. Connectivity and piezoelectric-pyroelectric composites. *Materials Research Bulletin* **13**, 525–536 (1978).
26. Newnham, R. E., Bowen, L. J., Klicker, K. A. & Cross, L. E. Composite piezoelectric transducers. *Materials & Design* **2**, 93–106 (1980).
27. Zhang, S. *et al.* Advantages and Challenges of Relaxor-$PbTiO_3$ Ferroelectric Crystals for Electroacoustic Transducers- A Review. *Prog Mater Sci* **68**, 1–66 (2015).
28. Zhang, S. & Li, F. High Performance Ferroelectric Relaxor-$PbTiO_3$ Single Crystals: Status and Perspective. *Journal of Applied Physics* **111**, 031341 (2012).
29. Li, F. *et al.* The origin of ultrahigh piezoelectricity in relaxor-ferroelectric solid solution crystals. *Nat Commun* **7**, 13807 (2016).
30. Park, S.-E. & Shrout, T. R. Ultrahigh strain and piezoelectric behavior in relaxor based ferroelectric single crystals. *Journal of Applied Physics* **82**, 1804–1811 (1997).
31. Zhang, S. & Shrout, T. R. Relaxor-PT single crystals: observations and developments. *IEEE Transactions on Ultrasonics, Ferroelectrics, and Frequency Control* **57**, 2138–2146 (2010).
32. Li, F. *et al.* Giant piezoelectricity of Sm-doped $Pb(Mg_{1/3}Nb_{2/3})O_3$-$PbTiO_3$ single crystals. *Science* **364**, 264–268 (2019).
33. Grinberg, I. *et al.* Structure and dielectric response in the high T_C ferroelectric $Bi(Zn,Ti)O_3$-$PbTiO_3$ solid solutions. *Phys. Rev. Lett.* **98**, 107601 (2007).

34. Shannon, R. D. Revised effective ionic radii and systematic studies of interatomic distances in halides and chalcogenides. *Acta Cryst A* **32**, 751–767 (1976).
35. Liu, Z. *et al.* High Curie temperature bismuth-based piezo-/ferroelectric single crystals of complex perovskite structure: recent progress and perspectives. *CrystEngComm* **24**, 220–230 (2022).
36. Liu, Z. *et al.* High Curie-temperature (T_C) piezo-/ferroelectric single crystals with bismuth-based complex perovskites: Growth, structures and properties. *Acta Materialia* **136**, 32–38 (2017).
37. Paterson, A. R. *et al.* High-temperature solution growth and characterization of $(1-x)PbTiO_3-xBi(Zn_{2/3}Nb_{1/3})O_3$ piezo-/ferroelectric single crystals. *Journal of Crystal Growth* **486**, 38–44 (2018).
38. Pecharsky, V. & Zavalij, P. *In Fundamentals of Powder Diffraction and Structural Characterization of Materials*. *Fundamentals of Powder Diffraction and Structural Characterization of Materials, by V. Pecharsky and P. Zavalij. XXIII, 713 p. With CD-ROM. 0-387-24147-7. Berlin: Springer, 2005.* (2003).
39. Barsoukov, E. & Macdonald, J. R. *Impedance spectroscopy: theory, experiment, and applications*. (John Wiley & Sons, 2018).
40. Xu, Y. *Ferroelectric materials and their applications*. (Elsevier, 2013).
41. Powell, R. C. *Symmetry, Group Theory, and the Physical Properties of Crystals*. vol. 824 (Springer New York, 2010).
42. Ye, Z.-G. & Bokov, A. A. Dielectric and Structural Properties of Relaxor Ferroelectrics. *Ferroelectrics* **302**, 227–231 (2004).
43. Ye, Z. G. Relaxor Ferroelectric Complex Perovskites: Structure, Properties and Phase Transitions. *KEM* **155–156**, 81–122 (1998).
44. Li, F. Exploration of the mechanisms enabling high performance in relaxor ferroelectric crystals. *Chin. Sci. Bull.* **67**, 3873–3881 (2022).

45. Bokov, A. A., Ye, Z.-G. & Bokov, A. A. Freezing of dipole dynamics in relaxor ferroelectric $Pb(Mg_{1/3}Nb_{2/3})O_3$-$PbTiO_3$ as evidenced by dielectric spectroscopy. *J. Phys.: Condens. Matter* **12**, L541–L548 (2000).

46. Bing, Y.-H., Bokov, A. A. & Ye, Z.-G. Diffuse and sharp ferroelectric phase transitions in relaxors. *Current Applied Physics* **11**, S14–S21 (2011).

47. Farber, L. & Davies, P. Influence of Cation Order on the Dielectric Properties of $Pb(Mg_{1/3}Nb_{2/3})O_3$-$Pb(Sc_{1/2}Nb_{1/2})O_3$ (PMN-PSN) Relaxor Ferroelectrics. *Journal of the American Ceramic Society* **86**, 1861–1866 (2003).

48. Venturini, E. L., Grubbs, R. K., Samara, G. A., Bing, Y. & Ye, Z.-G. Ferroelectric and relaxor properties of $Pb(Sc_{0.5}Nb_{0.5})O_3$: Influence of pressure and biasing electric field. *Phys. Rev. B* **74**, 064108 (2006).

49. Ye, Z.-G. *et al.* Development of ferroelectric order in relaxor (1−x) $Pb(Mg_{1/3}Nb_{2/3})O_3$-$xPbTiO_3$ (0 <~ x <~ 0.15). *Phys. Rev. B* **67**, 104104 (2003).

50. Perrin, C. *et al.* Neutron diffraction study of the relaxor-ferroelectric phase transition in disordered $Pb(Sc_{1/2}Nb_{1/2})O_3$. *Journal of Physics: Condensed Matter* **12**, 7523 (2000).

51. Lee, M.-S., Park, J.-W. & Jeong, Y. H. Grain growth anomaly and piezoelectric properties of liquid phase sintered high T_C $0.36BiScO_3$-$0.64PbTiO_3$ ceramics with sillenite $Bi_{12}PbO_{19}$. *Ceramics International* **47**, 34405–34413 (2021).

52. Sehirlioglu, A., Sayir, A. & Dynys, F. Microstructure–Property Relationships in Liquid Phase-Sintered High-Temperature Bismuth Scandium Oxide-Lead Titanate Piezoceramics. *Journal of the American Ceramic Society* **91**, 2910–2916 (2008).

53. Peräntie, J., Tailor, H. N., Hagberg, J., Jantunen, H. & Ye, Z.-G. Electrocaloric properties in relaxor ferroelectric (1− *x*)$Pb(Mg_{1/3}Nb_{2/3})O_3$–$xPbTiO_3$ system. *Journal of Applied Physics* **114**, 174105 (2013).

54. Kojima, S., Hidaka, Y., Tsukada, S., Bing, Y. & Ye, Z.-G. Brillouin scattering studies of ordered $Pb(Sc_{1/2}Nb_{1/2})O_3$ crystal with vacancies. *Ferroelectrics* **556**, 44–50 (2020).
55. Cross, L. E. Relaxor Ferroelectrics. in *Piezoelectricity* vol. 114 131–155 (Springer Berlin Heidelberg, 2008).
56. Krogstad, M. J. *et al.* The relation of local order to material properties in relaxor ferroelectrics. *Nature Mater* **17**, 718–724 (2018).
57. Perrin, C. *et al.* Influence of B-site chemical ordering on the dielectric response of the $Pb(Sc_{1/2}Nb_{1/2})O_3$ relaxor. *Journal of Physics: Condensed Matter* **13**, 10231 (2001).
58. Nomura, S., Kaneta, K., Kuwata, J. & Uchino, K. Phase transition in the PbTiO-A $(B_{23}Nb_{13})O_3$ (A= La, Bi; B= Zn, Mg) solid solutions. *Materials Research Bulletin* **17**, 1471–1475 (1982).
59. Sunder, V. S., Halliyal, A. & Umarji, A. M. Investigation of tetragonal distortion in the $PbTiO_3$–$BiFeO_3$ system by high-temperature x-ray diffraction. *Journal of materials research* **10**, 1301–1306 (1995).
60. Stringer, C. J., Shrout, T. R., Randall, C. A. & Reaney, I. M. Classification of transition temperature behavior in ferroelectric $PbTiO_3$–$Bi(Me'Me'')O_3$ solid solutions. *Journal of Applied Physics* **99**, 024106 (2006).
61. Freitas, V. F. *et al.* Piezoelectric Characterization of $(0.6)BiFeO_3$–$(0.4)PbTiO_3$ Multiferroic Ceramics. *Journal of the American Ceramic Society* **94**, 754–758 (2011).
62. Ganesh, P. *et al.* Origin of diffuse scattering in relaxor ferroelectrics. *Phys. Rev. B* **81**, 144102 (2010).
63. Chu, F., Reaney, I. M. & Setter, N. Spontaneous (zero-field) relaxor–to–ferroelectric-phase transition in disordered $Pb(Sc_{1/2}Nb_{1/2})O_3$. *Journal of Applied Physics* **77**, 1671–1676 (1995).

64. Liu, J. *et al.* Insights into the dielectric response of ferroelectric relaxors from statistical modeling. *Phys. Rev. B* **96**, 054115 (2017).
65. Uchino, K. *Ferroelectric Devices*. (CRC Press, 2018).
66. Ye, Z.-G. *Handbook of advanced dielectric, piezoelectric and ferroelectric materials*. (Woodhead Publishing Limited, 2008).
67. *Handbook of Advanced Dielectric, Piezoelectric and Ferroelectric Materials: Synthesis, Properties and Applications*. (CRC Press, 2008).
68. Zhang, S., Jiang, X., Lapsley, M., Moses, P. & Shrout, T. R. Piezoelectric accelerometers for ultrahigh temperature application. *Applied Physics Letters* **96**, (2010).
69. Shrout, T. R., Zhang, S., Eitel, R., Stringer, C. & Randall, C. A. High performance, high temperature perovskite piezoelectrics: 2004 14th IEEE International Symposium on Applications of Ferroelectrics, ISAF-04. A Conference of the IEEE Ultrasonics, Feroelectrics, and Frequency Control Society (UFFC-S). in 126–129 (2005).
70. De, U., Sahu, K. R. & De, A. Ferroelectric Materials for High Temperature Piezoelectric Applications. *SSP* **232**, 235–278 (2015).
71. Li, X., Wang, Z., He, C., Long, X. & Ye, Z.-G. Growth and piezo-/ferroelectric properties of PIN-PMN-PT single crystals. *Journal of Applied Physics* **111**, 034105 (2012).
72. Seregin, D., Vorotilov, K., Sigov, A. & Kotova, N. Porous PZT films prepared by PVP assisted sol-gel process. *Ferroelectrics* **484**, 43–48 (2015).
73. Izyumskaya, N. *et al.* Processing, Structure, Properties, and Applications of PZT Thin Films. *Critical Reviews in Solid State and Materials Sciences* **32**, 111–202 (2007).

74. Bokov, A. A., Long, X. & Ye, Z.-G. Optically isotropic and monoclinic ferroelectric phases in $Pb(Zr_{1-x}Ti_x)O_3$ (PZT) single crystals near morphotropic phase boundary. *Phys. Rev. B* **81**, 172103 (2010).

75. Eitel, R. E., Zhang, S. J., Shrout, T. R., Randall, C. A. & Levin, I. Phase Diagram of the Perovskite System $(1-x)BiScO_3$-$xPbTiO_3$. *Journal of Applied Physics* **96**, 2828–2831 (2004).

76. Zhang, S., Randall, C. A. & Shrout, T. R. Characterization of perovskite piezoelectric single crystals of $0.43BiScO_3$–$0.57PbTiO_3$ with high Curie temperature. *Journal of Applied Physics* **95**, 4291–4295 (2004).

77. Eitel, R. E., Randall, C. A., Shrout, T. R. & Park, S.-E. Preparation and Characterization of High Temperature Perovskite Ferroelectrics in the Solid-Solution $(1-x)BiScO_3$ –$xPbTiO_3$. *Jpn. J. Appl. Phys.* **41**, 2099–2104 (2002).

78. Dong, Y., Zou, K., Liang, R. & Zhou, Z. Review of $BiScO_3$-$PbTiO_3$ piezoelectric materials for high temperature applications: fundamental, progress, and perspective. *Progress in Materials Science* **132**, 101026 (2023).

79. Castro, A. *et al.* Synthesis, Structural Characterization, and Properties of Perovskites Belonging to the $x\ BiMnO_3-(1-x)PbTiO_3$ System. *Chemistry of Materials* **22**, 541–550 (2010).

80. Pan, Z. *et al.* High piezoelectric performance in a new Bi-based perovskite of $(1-x)Bi(Ni_{1/2}Hf_{1/2})O_3-xPbTiO_3$. *Journal of Applied Physics* **112**, 114120 (2012).

81. Li, Z. *et al.* Grain size effect on piezoelectric properties of rhombohedral lead zirconate titanate ceramics. *Ceramics International* **49**, 27733–27741 (2023).

82. Li, J.-F. & Cheng, D. Compositional effect on piezoelectric and anomalous photovoltaic properties of PLZT ceramics with fixed grain sizes. *J Electroceram* **21**, 267–270 (2008).

83. Randall, C. A., Hilton, A. D., Barber, D. J. & Shrout, T. R. Extrinsic contributions to the grain size dependence of relaxor ferroelectric $Pb(Mg_{1/3}Nb_{2/3})O_3$: $PbTiO_3$ ceramics. *J. Mater. Res.* **8**, 880–884 (1993).

84. Dong, Y., Zhou, Z., Liang, R. & Dong, X. Correlation between the grain size and phase structure, electrical properties in $BiScO_3$-$PbTiO_3$ -based piezoelectric ceramics. *J Am Ceram Soc* **103**, 4785–4793 (2020).

85. Zhang, S., Randall, C. A. & Shrout, T. R. High Curie temperature piezocrystals in the $BiScO_3$-$PbTiO_3$ perovskite system. *Applied Physics Letters* **83**, 3150–3152 (2003).

86. Takenaka, T. & Kawachi, T. Piezoelectric properties of $Pb(Sc_{1/2}Nb_{1/2})O_3$-$PbTiO_3$ ceramics. *Ferroelectrics* **169**, 303–307 (1995).

87. Bobnar, V., Uršič, H., Casar, G. & Drnovšek, S. Distinctive contributions to dielectric response of relaxor ferroelectric lead scandium niobate ceramic system. *Physica Status Solidi (b)* **250**, 2232–2236 (2013).

88. Shirane, G. & Hoshino, S. On the Phase Transition in Lead Titanate. *J. Phys. Soc. Jpn.* **6**, 265–270 (1951).

89. Viviani, M., Bassoli, M., Buscaglia, V., Buscaglia, M. T. & Nanni, P. Giant permittivity and Maxwell–Wagner relaxation in Yb : $CaTiO_3$ ceramics. *J. Phys. D: Appl. Phys.* **42**, 175407 (2009).

90. Wang, G. *et al.* Origin of Colossal Dielectric Behavior In Double Perovskite Ba_2CoNbO_6. *Journal of the American Ceramic Society* **96**, 2203–2210 (2013).

91. Abrahams, S. C., Kurtz, S. K. & Jamieson, P. B. Atomic Displacement Relationship to Curie Temperature and Spontaneous Polarization in Displacive Ferroelectrics. *Phys. Rev.* **172**, 551–553 (1968).

92. Levit, R., Martinez-Garcia, J. C., Ochoa, D. A. & García, J. E. The generalized Vogel-Fulcher-Tamman equation for describing the dynamics of relaxor ferroelectrics. *Sci Rep* **9**, 12390 (2019).

93. Bokov, A. A. & Ye, Z.-G. Field-induced shift of morphotropic phase boundary and effect of overpoling in (1−x)Pb($Mg_{1/3}Nb_{2/3}$)O_3–xPbTiO_3 piezocrystals. *Applied Physics Letters* **92**, 082901 (2008).

94. Wang, B. Growth and Characterization of Lead Zirconate-Titanate ($PbZr_{1-x}Ti_xO_3$)-Based Novel Piezo-/Ferroelectric Single Crystals (2016).

95. Qiao, P. *et al.* Enhanced electromechanical performance of PSZT–PMS–PFW through morphotropic phase boundary design and defect engineering. *Journal of Materials Chemistry C* **11**, 11631–11642 (2023).

96. Fu, H. & Cohen, R. E. Polarization rotation mechanism for ultrahigh electromechanical response in single-crystal piezoelectrics. *Nature* **403**, 281–283 (2000).

97. Zhang, S. & Yu, F. Piezoelectric Materials for High Temperature Sensors. *Journal of the American Ceramic Society* **94**, 3153–3170 (2011).

98. Noheda, B. *et al.* The monoclinic phase in PZT: New light on morphotropic phase boundaries. *AIP Conference Proceedings* **535**, 304–313 (2000).

99. Smith, G. L. *et al.* PZT-Based Piezoelectric MEMS Technology. *Journal of the American Ceramic Society* **95**, 1777–1792 (2012).

100. Ye, Z.-G. High-performance piezoelectric single crystals of complex perovskite solid solutions. *MRS bulletin* **34**, 277–283 (2009).

101. Yuan, Y., Liu, Z., Bari, M. & Ye, Z.-G. Growth, Structure, and characterization of new High-TC Piezo-/Ferroelectric Bi($Zn_{2/3}Ta_{1/3}$)O_3-PbTiO_3 single crystals. *Journal of Crystal Growth* **580**, 126473 (2022).

102. Ye, Z.-G. & Dong, M. Morphotropic domain structures and phase transitions in relaxor-based piezo-/ferroelectric (1−x)Pb($Mg_{1/3}Nb_{2/3}$)O_3−xPbTiO_3 single crystals. *Journal of Applied Physics* **87**, 2312–2319 (2000).

103. Noheda, B., Cox, D. E., Shirane, G., Gao, J. & Ye, Z.-G. Phase diagram of the ferroelectric relaxor (1−x) $Pb(Mg_{1/3}Nb_{2/3})O_3$ −x$PbTiO_3$. *Phys. Rev. B* **66**, 054104 (2002).

104. Ye, Z.-G., Dong, M. & Yamashita, Y. Thermal stability of the $Pb(Zn_{1/3}Nb_{2/3})O_3$-$PbTiO_3$ [$PZNT_{91/9}$] and $Pb(Mg_{1/3}Nb_{2/3})O_3$-$PbTiO_3$ [$PMNT_{68/32}$] single crystals. *Journal of Crystal Growth* **211**, 247–251 (2000).

105. Long, X. & Ye, Z.-G. Top-seeded solution growth and characterization of rhombohedral PMN–30PT piezoelectric single crystals. *Acta Materialia* **55**, 6507–6512 (2007).